ABSTRACT

Title of Dissertation: TUNNELING AND RAMAN SPECTROSCOPIES OF THE ELECTRON-DOPED HIGH-TEMPERATURE SUPERCONDUCTORS

Muhammad Mumtaz Qazilbash, Doctor of Philosophy, 2004

Dissertation directed by: Professor Richard L. Greene
Department of Physics

This thesis consists of spectroscopic studies of the electron-doped high temperature cuprate superconductors $Pr_{2-x}Ce_xCuO_{4-\delta}$ (PCCO) and $Nd_{2-x}Ce_xCuO_{4-\delta}$ (NCCO).

Point contact and high barrier tunneling spectroscopies were employed to study the evolution of the superconducting gap (Δ) with cerium doping. Point contact spectroscopy of low barrier junctions reveals that the gap changes from *d*-wave in under-doped PCCO to a nodeless gap in over-doped PCCO. This transition in pairing symmetry occurs just above optimal doping.

High barrier tunnel junctions were prepared on optimally doped PCCO and NCCO crystals for tunneling into the *ab*-planes. The spectra are not consistent with either a clean *s*-wave gap or a clean monotonic $d_{x^2-y^2}$ gap, and can be explained by a non-monotonic *d*-wave gap.

A normal state gap near zero voltage bias is observed in the tunneling spectra for dopings between x = 0.13 and x = 0.19 when superconductivity is suppressed

by magnetic fields larger than the upper critical fields (H_{c2}). The normal state gap appears to coexist with the superconducting gap. The normal state gap vanishes at a temperature close to the superconducting transition temperature for optimally doped samples.

Raman spectroscopy was employed to systematically study the electronic properties of PCCO and NCCO crystals and films across the superconducting phase diagram. Polarization and doping dependence of the 2Δ coherence peaks in the superconducting state show a change in the superconducting gap from non-monotonic d-wave at optimal doping to either a dirty d-wave or a dirty s-wave in the over-doped samples.

By analyzing coherence effects, we find that all coherent carriers in the non-superconducting state condense to form the superfluid. Carriers that are doped beyond optimal doping are incoherent and do not contribute to the coherent Raman response in the normal and superconducting states.

We systematically studied the effects of temperature and magnetic field on the coherence peaks in the Raman spectra for various dopings. Compared to the optimally doped crystals, H_{c2} decreases by more than an order of magnitude in the most over-doped crystal. The implications of these observations are discussed.

TUNNELING AND RAMAN SPECTROSCOPIES OF THE ELECTRON-DOPED HIGH-TEMPERATURE SUPERCONDUCTORS

by

Muhammad Mumtaz Qazilbash

Dissertation submitted to the Faculty of the Graduate School of the
University of Maryland at College Park in partial fulfillment
of the requirements for the degree of
Doctor of Philosophy
2004

Advisory Committee:

Professor Richard L. Greene, Chairman
Dr. Girsh Blumberg
Professor H. Dennis Drew
Professor Christopher J. Lobb
Professor Ichiro Takeuchi

DEDICATION

To those who strive for justice

ACKNOWLEDGEMENTS

High-temperature superconductors were discovered in 1986 and the news was flashed around the world. I was in high school when I first read about these fascinating materials on the front page of a newspaper and I hoped to work with these materials some day. Therefore, I am indebted to my advisor, Professor Rick Greene, who allowed me to work on the electron-doped high-temperature superconductors and then provided plenty of encouragement. Rick has been a great advisor who has always given the correct advice and just the right amount of supervision. He has tolerated my independent-minded approach to research issues as well as my habit of being unduly critical of my own work. His vast knowledge and experience with high-temperature superconductors has helped me to keep my research on track. In short, I am lucky to have had him as my advisor.

I am grateful to Dr. Girsh Blumberg for the opportunity to work in his Raman lab at Lucent Technologies, Bell Labs. It would be fair to say that Girsh's Raman spectrometer and associated setup made it relatively easy to obtain the very low energy electronic Raman spectra, something that would have been difficult to do at any other Raman lab. I have learnt a lot about superconductivity and Raman scattering from Girsh. He has also taught me to study and analyze the data in novel ways.

When I first joined Rick's lab, I was taught the basic low temperature physics techniques by two postdocs: Amlan Biswas and Vera Smolyaninova. Amlan also got me started with point contact tunneling and helped me make it work. Later on I had the opportunity of interacting with Yoram Dagan, whose experience with film growth and tunneling spectroscopy has benefited me greatly. I wish to thank Bing Liang for WDS measurements on crystals of the electron-doped cuprates.

I would like to thank the graduate students with whom I have shared the lab: Hamza Balci, Josh Higgins and Pengcheng Li. Even though each of us had separate projects, we have worked as a team and have helped each other in numerous ways. I also wish to thank Matt Sullivan, in particular for providing me with YBCO films, and in general for the interesting, informative and provocative interactions we have had in the lab. Thanks are due to the undergraduates with whom I have worked: Chris Hill, Matt Barr, William Fisher, Rich Ott and Rachel Headley.

Thanks are due to the people I have worked with in Girsh's lab: Adrian Gozar and Brian Dennis. They helped me get started with the Raman experiments and provided answers to my questions about the Raman setup. I wish to thank Girsh's former student, Andreas Koitzsch, for making his data and thesis available to me.

One of the important benefits of working in the Center of Superconductivity Research has been the opportunity to interact with other professors associated with the Center. I wish to thank Chris Lobb, Dennis Drew, Steve Anlage, Fred Wellstood and Ichiro Takeuchi for helpful discussions and suggestions.

I acknowledge fruitful collaboration with Chris Kendziora on Raman studies of PCCO films at the Naval Research Labs.

Thanks are also due to Doug Bensen and Brian Straughn for technical support, and to Z. Y. Li for crystal growth and target preparation.

This research work has been made easier with the encouragement and support provided by my family, especially my mother, and by my friends both here and abroad.

TABLE OF CONTENTS

LIST OF FIGURES

Chapter 1

Introduction

A new state of matter was discovered in 1911 by Kamerlingh Onnes. He observed that upon cooling with liquid He-4, the resistivity of a mercury sample vanished at 4.2 K [1]. This new state of matter is called a superconductor and exhibits two fundamental characteristics: zero DC resistivity below a critical transition temperature (T_c) and the ability to expel a magnetic field upon lowering the temperature below T_c (Meissner effect) [1].

Subsequently, superconductivity was observed in several metallic elements (e.g. Pb, Sn, Nb, Al) and in binary alloys (e.g. Nb_3Sn). However, a complete understanding of the mechanism that is responsible for superconductivity eluded the scientific community for over forty years after the initial discovery. The isotope effect in superconductors was discovered in 1951 and gave a vital clue for understanding superconductivity [1]. It was observed that T_c was proportional to $M^{-1/2}$ for isotopes of the same element (M is the atomic mass of the isotope). This suggested that the lattice plays a direct role in superconductivity. At about the same time, Fröhlich emphasized the importance of the electron-lattice interaction in explaining superconductivity [1]. Not long after, in 1957, Bardeen, Cooper and Schrieffer (BCS) put forward a comprehensive theory of superconductivity based upon electron-pairing via phonon mediated attraction [1, 2]. The basic physical idea is that an electron polarizes the medium by attracting positive ions; these excess positive ions in turn

attract a second electron. This leads to an effective attraction between the two electrons. If this attraction is stronger than the screened Coulomb repulsion then a net attractive potential results and gives rise to superconductivity. Superconductivity is a truly macroscopic quantum phenomenon [2, 1].

All superconducting (SC) metals have low T_c of less than 10 K and their SC properties were well explained by the BCS theory. For many years the highest known T_c was 23 K in the A-15 compound Nb_3Ge. This situation changed dramatically when in 1986, Alex M*ü*ller and Georg Bednorz discovered superconductivity in a ceramic sample of $(La,Ba)_2CuO_4$ (LBCO) at $T \approx 30$ K [3]. This monumental discovery was followed by an intense search for superconductivity in the copper-oxide compounds (cuprates). About six months later, a new superconductor $YBa_2Cu_3O_7$ (YBCO) was discovered with T_c of about 90 K [4]. Since then, several other families of SC cuprates were discovered with the highest T_c of 138 K (at ambient pressure) obtained in $Hg_{0.8}Tl_{0.2}Ba_2Ca_2Cu_3O_{8.33}$ [5]. Clearly, the T_c values were much higher than those of conventional superconductors. It also appeared that some superconducting properties of these high-temperature superconductors (HTSC) could not be explained by conventional BCS theory based on electron-phonon interactions [1]. Moreover, these materials displayed unusual properties in their non-SC state that could not be reconciled with the Landau Fermi Liquid theory that describes so well the properties of metals [6]. The Landau Fermi Liquid theory's description of the metallic state is in terms of "quasiparticles" or "dressed" electrons (holes) that incorporates the weak interactions between the electrons (holes). This description starts to break down in the cuprates because of relatively stronger electron-electron correlations.

The parent compounds of the cuprates are Mott insulators [7] with long-range anti-ferromagnetic ordering. Superconductivity is realized by doping the parent compounds with holes or electrons. Most of the cuprates are hole-doped. In 1989, Tokura *et al.* discovered the electron-doped cuprates [8]. The electron-doped cuprates have a relatively modest maximum T_c of about 25 K. Most of the work pre-

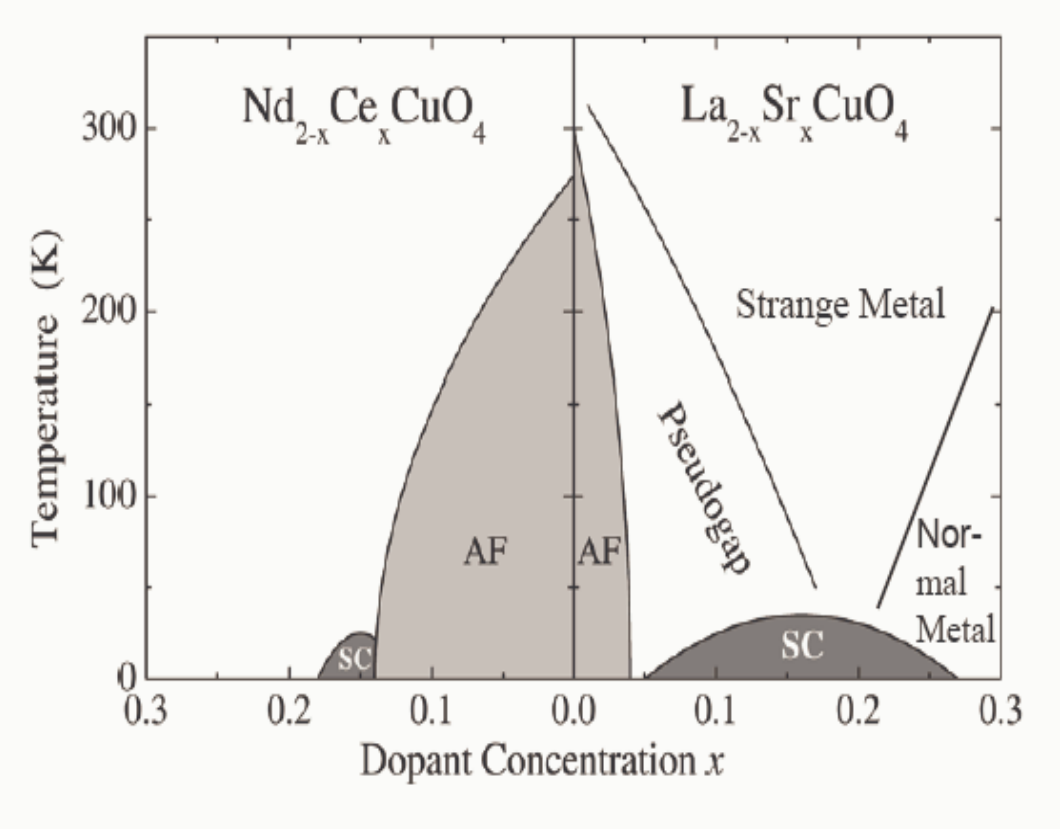

Figure 1.1: Phase diagram of the cuprate superconductors for hole doping (right hand side) and electron doping (left hand side). Taken from Ref. [9].

sented in this thesis was carried out on two electron-doped cuprates $Pr_{2-x}Ce_xCuO_{4-\delta}$ (PCCO) and $Nd_{2-x}Ce_xCuO_{4-\delta}$ (NCCO).

The cuprates possess a rich phase diagram shown in Fig. 1.1. For example, in the hole-doped $La_{2-x}Sr_xCuO_4$, the parent compound is La_2CuO_4, an anti-ferromagnetic insulator with a Neel temperature (T_N) of 300 K. Holes are introduced into the copper oxide planes by partly replacing La^{3+} with Sr^{2+}. The anti-ferromagnetism is suppressed at about 0.02 extra holes per copper atom and the material enters a spin-glass phase. If the material is doped further with Sr^{2+}, superconductivity appears at x = 0.06. Further doping increases carrier concentration and T_c. Maximum T_c is obtained at x=0.15. The T_c drops with further doping and superconductivity disappears at x = 0.3. Therefore, the SC phase is dome-shaped. Other hole-doped

HTSC have a very similar phase diagram to LSCO.

The phase diagram of the electron-doped HTSC is qualitatively similar but quantitatively different from the phase diagram of the hole-doped HTSC. The parent compound R_2CuO_4 (R = Nd, Pr) is also an anti-ferromagnetic insulator (Nd_2CuO_4 has a T_N of 255 K). This is doped with Ce^{4+} to introduce electrons in the copper oxide planes. However, compared to the hole-doped HTSC, anti-ferromagnetism persists up to a much higher doping of about x = 0.14 in NCCO. Superconductivity suddenly appears when the doping is increased beyond x = 0.14 and maximum T_c occurs at x = 0.15. Superconductivity vanishes in NCCO for dopings above x = 0.18. The doping range for the SC phase is the same in polycrystals, single crystals and films of NCCO [8, 10, 11]. In PCCO films, the doping range for the SC phase is somewhat larger, between 0.12 and 0.2 [12]. Maximum T_c occurs at x $\approx$ 0.15 for both single crystals and films of PCCO. In general, the doping range is larger for the anti-ferromagnetic phase and smaller for the SC phase in the electron-doped HTSC compared to the corresponding doping ranges in the hole-doped HTSC. Moreover, the T_c of the hole-doped cuprates is generally much higher than that of the electron-doped cuprates.

Both hole-doped and electron-doped HTSC have similar crystal structures (see Fig. 1.2). Both families consist of alternating block layers and copper-oxide planes. The block layers consist of relatively inert elements that act as charge reservoirs since they supply electrons or holes to the copper-oxide planes. The doped conduction electrons (holes) in the copper-oxide planes determine the electronic properties of the HTSC. LSCO crystallizes in a T-structure while PCCO and NCCO crystallize in a T'-structure [13]. In the T'-structure, there is no "apical" oxygen because the Nd (Pr) ions and oxygen ions are offset.

The HTSC are highly anisotropic with the out-of-plane lattice constant much larger than the in-plane lattice constants. This makes them essentially two-dimensional when considering their physical properties. One should note here that the HTSC are

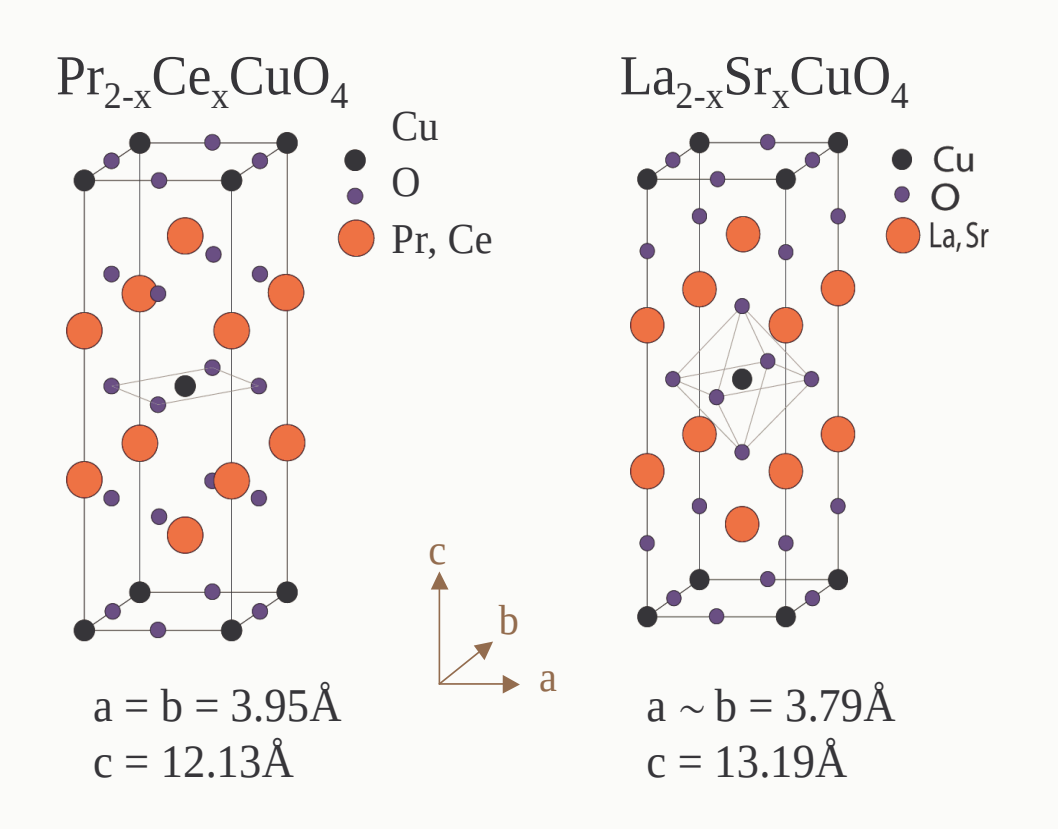

Figure 1.2: Unit cells of $Pr_{2-x}Ce_xCuO_4$ and $La_{2-x}Sr_xCuO_4$. Adapted from Ref. [13]

type-II superconductors, with the Ginzburg-Landau (GL) parameter $\kappa >> 1$ with $\kappa = \lambda_{ab}/\xi_{ab}$. This is because their in-plane magnetic penetration depths (λ_{ab}) are much greater than their in-plane coherence lengths (ξ_{ab}). For example, in hole-doped HTSC, $\lambda_{ab} \approx 2000\ \mathring{A}$ and $\xi_{ab} \approx 20\ \mathring{A}$.

The HTSC have cylindrical Fermi surfaces because of their two-dimensional character. Their Fermi surfaces have been mapped by Angle-resolved Photoemission Spectroscopy (ARPES). The Fermi surface for NCCO is shown in Fig. 1.3. The red regions in Fig. 1.3 describe a Fermi surface with well-defined quasiparticles. The green areas between the red areas are regions where the Fermi surface is not well-defined. These regions are known as "hot spots" and occur at the intersection of the Fermi surface and the diamond-shaped anti-ferromagnetic Brillouin zone. These "hot spots" are regions on the Fermi surface which are separated by the

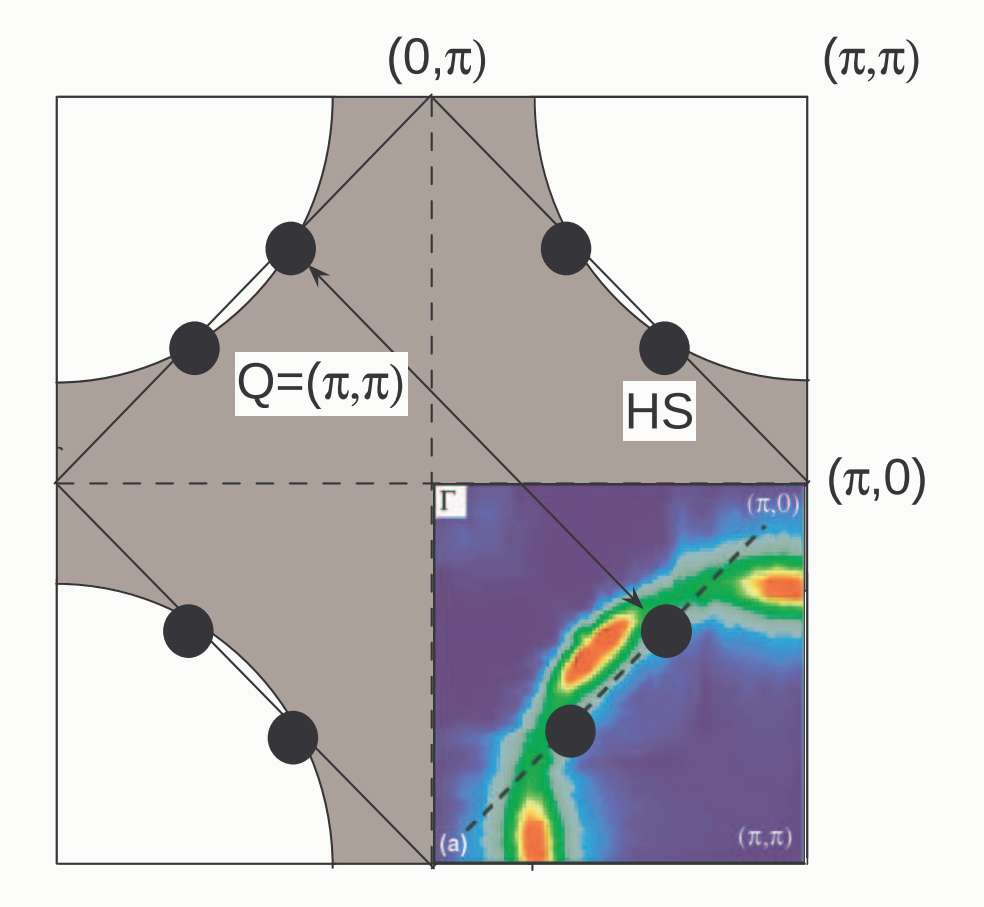

Figure 1.3: The Fermi surface of NCCO: a schematic showing the square-shaped Brillouin zone, the diamond-shaped anti-ferromagnetic Brillouin zone, and the Fermi surface where the gray areas depict filled electronic states. The lower right quadrant shows the Fermi surface mapped by ARPES [14].

anti-ferromagnetic vector $\mathbf{Q} = (\pi,\pi)$ and where the anti-ferromagnetic interactions between quasi-particles are enhanced. Among the numerous theories of superconductivity, the one that describes pairing of the electrons via anti-ferromagnetic spin fluctuations [15] has been given serious consideration. This is because it predicts a directional dependence in the electronic properties of the cuprates: more specifically, it predicts a $d_{x^2-y^2}$ gap symmetry that has been observed in most of the cuprates. The issue of gap symmetry will be discussed later. Secondly, the proximity of the SC phase to the anti-ferromagnetic phase makes it a natural candidate for explain-

ing the origin of superconductivity since it supposes that spin fluctuations persist even after the long-range anti-ferromagnetic order is destroyed. We will revisit this theory later to explain some of the experimental results.

Soon after the discovery of HTSC, considerable effort by thousands of scientists was directed towards understanding the behavior of these complex materials. One of the important research issues is understanding the mechanism that gives rise to superconductivity in these materials. This is the main motivation behind most of the research on HTSC. This is a complex issue that has remained unresolved for eighteen years. Many theories have been put forward to explain superconductivity in HTSC. However, there is no consensus on any one theory. Experiments on magnetic flux quantization and the Josephson effect have shown that, as in conventional superconductors, electron pairing in momentum space is responsible for superconductivity [1]. Moreover, as in conventional superconductors, the Cooper pairs have zero net momentum and the pairing is of the spin singlet form [1]. However, what causes pairing and long range phase coherence in HTSC remains an open question.

In conventional superconductors, phonons provide the "glue" that binds the electrons in pairs (called Cooper pairs). The Cooper pair condensate is described by one BCS wavefunction that signifies long range phase coherence. The overall wavefunction is a superposition of paired states and this superposition is highly entangled. Both pairing and phase coherence occur at T_c. Pairing leads to a gap in the quasi-particle density of states. This is called the superconducting gap in BCS theory and the order parameter in the phenomenological Ginzburg-Landau theory of superconductivity. Pairing due to electron-phonon interaction results in a nearly isotropic gap around the Fermi surface (FS). An isotropic gap is often referred to as an s-wave gap or s-wave pairing symmetry (see Fig. 1.4a). The SC gap is an important signature of superconductivity and quantitative measurements of this property can provide valuable clues about the mechanism that drives superconductivity. The properties (magnitude, symmetry) of the SC gap can provide constraints on theories

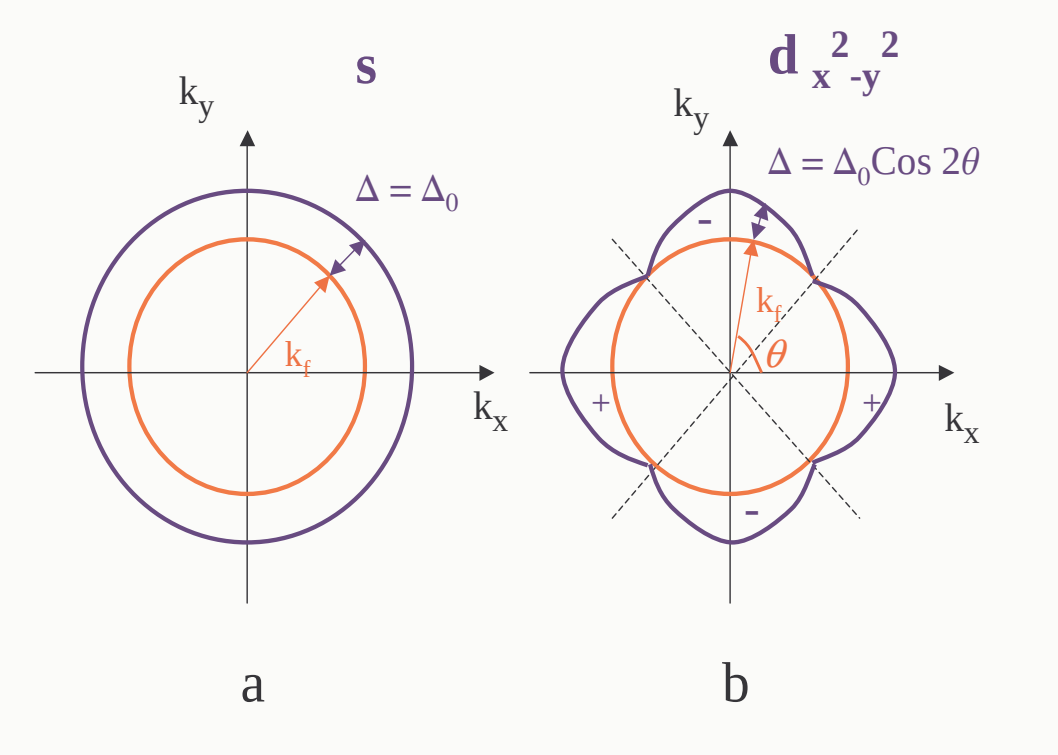

Figure 1.4: s-wave and $d_{x^2-y^2}$ SC gap symmetries.

that attempt to explain the mechanism underlying superconductivity in HTSC.

The SC gap, in general, is a complex quantity and has a magnitude and phase associated with it. It can be written in the general form $\Delta(\mathbf{k}) = |\Delta(\mathbf{k})|e^{i\phi(\mathbf{k})}$. Both the magnitude and phase of the gap may have momentum dependence. The magnitude of an isotropic s-wave gap is independent of momentum and its phase is constant (taken to be zero) in all directions in momentum space. In hole-doped HTSC, at optimum doping, there is abundant experimental evidence that the SC gap is predominantly $d_{x^2-y^2}$ or d-wave [16]. The d-wave gap is shown in Fig. 1.4b. This type of gap is highly anisotropic, with the maximum gap magnitude occurring along the principal axes (k_x, k_y) and going to zero at four points (nodes) along the dotted lines (at 45^o to the principal axes). There is a sign change (or π phase shift) upon crossing the nodes and this means that the phase of the gap changes with direction in k-space. In the over-doped regime of the hole-doped HTSC, there

appears to be a convergence of experimental evidence that the gap retains its d-wave character [17]. However, the situation for the electron-doped compounds remains highly controversial with no convergence of experimental results on the question of the symmetry of the SC order parameter.

The half-integer flux quantization experiment on optimal electron-doped cuprates unambiguously identifies the pairing symmetry as predominantly $d_{x^2-y^2}$ [18]. This conclusion is supported by Angle Resolved Photoemission Spectroscopy (ARPES). Raman Spectroscopy on optimally doped $Nd_{2-x}Ce_xCuO_{4-\delta}$ (NCCO) supports a non-monotonic d-wave gap i.e. a $d_{x^2-y^2}$ gap with higher harmonics that preserve the nodes along Brillouin zone diagonals [19]. Earlier Raman data on NCCO had been interpreted in terms of an anisotropic s-wave gap [20]. Experiments on the temperature dependence of penetration depth have yet to reach consensus on the issue of gap symmetry [21, 22, 23, 24, 25, 26]. The same is true of tunneling experiments [27, 28, 29]. To summarize, the majority of experiments support a d-wave order parameter.

One of the main aims of the work presented in this thesis is to investigate the evolution of the SC gap with doping in the electron-doped cuprates using spectroscopic techniques like tunneling and Raman that directly probe the SC gap. This may lead to a better understanding of the SC order parameter and could resolve the conflicting experimental results. Moreover, recent transport and neutron scattering results [30, 31, 32] suggest the existence of a Quantum Critical Point [33] within the SC phase. Therefore, the work presented here assumes added importance considering the current interest in examining the relationship between the evolution of the order parameter with doping and quantum criticality.

A second important motivation for the spectroscopic measurements presented in this thesis is the study of the non-SC state that exists above T_c or above the upper critical field H_{c2}. An important advantage of the electron-doped materials are the relatively low H_{c2} because of larger coherence lengths ($\xi \approx 60$ $\mathring{A}$ at optimum

doping). H_{c2} is less than 10 T for optimally doped samples of the electron-doped cuprates and such fields are readily available in laboratories. This is important for spectroscopic measurements because higher temperatures ($T > T_c$) smear out the spectra. The non-SC state of these materials can be accessed at the lowest temperature by applying a field larger than H_{c2}. There is a strong belief in the HTSC community that the key to solving the mechanism of superconductivity lies in understanding the properties of the non-SC state.

Before giving a brief review of the spectroscopic methods used for studying the electron-doped HTSC, it would be appropriate to recap the essential features of the BCS theory that are relevant to two important SC properties: the SC gap and SC coherence effects [1, 2]. The BCS theory stipulates that in a superconductor *all* electrons form bound pairs at T = 0. These can be described by a single macroscopic wavefunction which is antisymmetric under exchange of single electrons. The wavefunction originally used by BCS is

$$|\psi_G\rangle = \prod_{\mathbf{k}=\mathbf{k}_1 \ldots \mathbf{k}_M} (u_{\mathbf{k}} + v_{\mathbf{k}} c^{\dagger}_{\mathbf{k}\uparrow} c^{\dagger}_{-\mathbf{k}\downarrow})|\phi_0\rangle \tag{1.1}$$

where $u^2_{\mathbf{k}} + v^2_{\mathbf{k}} = 1$. This form implies that the probability of the pair $(\mathbf{k}\uparrow, \mathbf{k}\downarrow)$ being occupied is $v^2_{\mathbf{k}}$ and the probability that it is unoccupied is $u^2_{\mathbf{k}}$. The probability amplitudes $u_{\mathbf{k}}$ and $v_{\mathbf{k}}$ differ by a constant phase factor. The creation operator $c^{\dagger}_{\mathbf{k}\uparrow}$, for example, creates an electron of momentum $\mathbf{k}$ and spin up. $|\phi_0\rangle$ is the vacuum state with no particles present.

The BCS Hamiltonian consists of a kinetic energy term and a potential energy term: the latter incorporates the weak attractive interaction between the electrons. Using the technique of second quantization (creation and annihilation operators) together with the variational method, the occupation probability amplitudes $u_{\mathbf{k}}$ and $v_{\mathbf{k}}$ can be determined in terms of the quasiparticle kinetic energy and the pair potential Δ. The spectrum of single particle excitations in a superconductor can also be determined. It turns out that there is an energy gap in the spectrum in

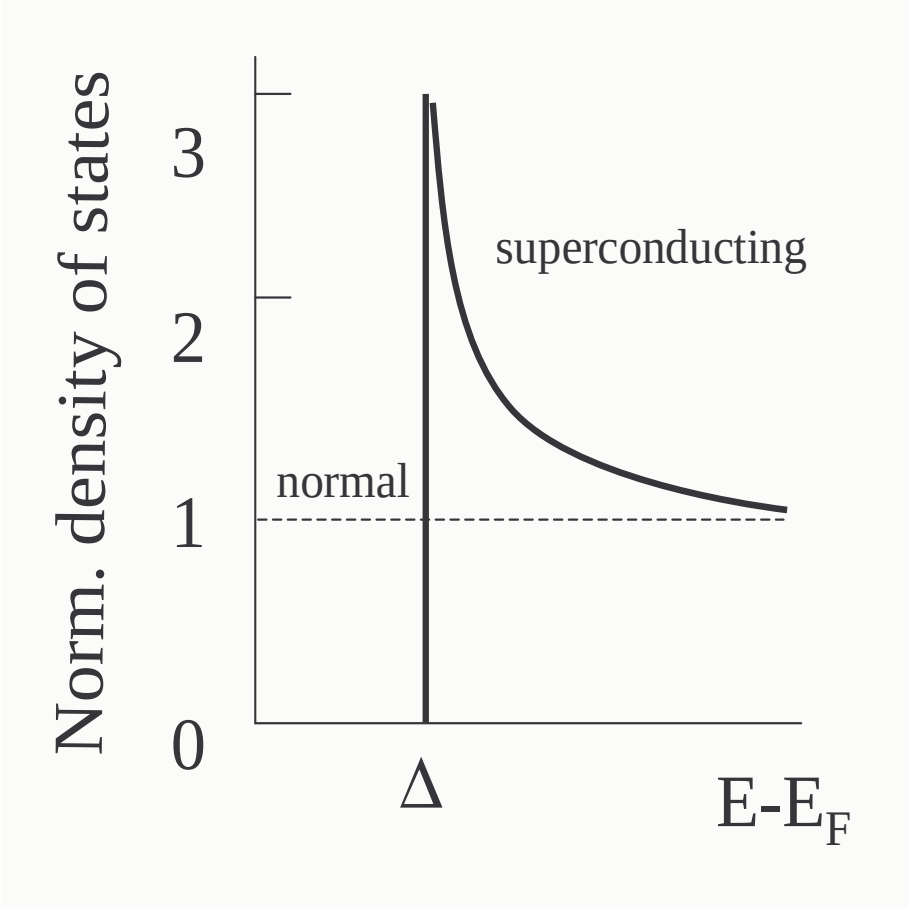

Figure 1.5: Normalized density of states in the SC state at $T = 0$

the superconducting state and this energy gap is the same as the pair potential Δ. There are no single particle states in the gap and a singularity in the density of states occurs at the gap edge (see Fig. 1.5).

While all conduction electrons pair up and condense in the superconducting state at T = 0, the probability amplitudes $u_{\mathbf{k}}$ and $v_{\mathbf{k}}$ ensure that only the condensate near the Fermi energy has its motion affected by the condensation [2]. It is this fraction (the superfluid) that responds to an external perturbation, for example, an electromagnetic wave. The pair potential Δ determines the range of $\mathbf{k}$ values of the Cooper pairs in the condensate that will respond to the external perturbation.

The effect of an external perturbation on the electrons in a metal can be ex-

pressed by the general interaction Hamiltonian:

$$H = \sum_{k\sigma,k'\sigma'} B_{k'\sigma',k\sigma} c^{\dagger}_{k'\sigma'} c_{k\sigma} \tag{1.2}$$

where $B_{k\sigma,k'\sigma'}$ are matrix elements of the perturbing operator between the single-electron states in a normal metal [1]. In the normal state, each term in this sum is independent and the square of each $B_{k'\sigma',k\sigma}$ gives the corresponding transition probability. This is not the case in the SC state. This is because the SC state consists of a coherent superposition of occupied one-electron states and as a result there are interference terms which are not present in the normal state. These interference terms are called **coherence factors** and are simply cross terms between $u_{\mathbf{k}}$ and $v_{\mathbf{k}}$. Their precise form depends on the type of perturbation and interaction. In calculations of transition probabilities, the squared matrix elements $|B_{k'\sigma',k\sigma}|^2$ are multiplied by the coherence factors, $(u_{\mathbf{k}}u_{\mathbf{k}'} \mp v_{\mathbf{k}}v_{\mathbf{k}'})^2$ for scattering from quasi-particles, and $(v_{\mathbf{k}}u_{\mathbf{k}'} \pm u_{\mathbf{k}}v_{\mathbf{k}'})^2$ for creation or annihilation of two quasi-particles. The upper signs are for Type I perturbations and the lower signs are for Type II perturbations. Type I perturbation is even under the time reversal of electronic states ($\mathbf{k} \longrightarrow -\mathbf{k}$) while type II perturbation is odd. The Type I coherence factor for the creation of two quasi-particles from the Cooper pair condensate enter the calculations for Raman scattering cross-section in the SC state.

The BCS theory was successful in explaining almost all the experiments that were carried on superconducting metals. The effect of the coherence factors and energy gap was seen in optical absorption and nuclear-spin relaxation experiments while single electron tunneling directly revealed the energy gap in the single particle density of states. BCS assumed a pairing interaction independent of direction in $\mathbf{k}$-space. This gives an energy gap over the entire Fermi surface. Experiments confirmed a fully gapped Fermi surface for conventional superconductors. In the BCS theory, the superconducting gap and coherence factors are intimately connected and the presence of one implies the presence of the other. However, coherence factors

are a more fundamental property of the SC state than the SC gap [1]. For example, semi-conductors have gaps but are not superconducting, while in superconductors with magnetic impurities there is no SC gap but SC phase coherence still exists. Since HTSC are unconventional superconductors, the SC gap and SC coherence effects cannot be *a priori* assumed to occur simultaneously below T_c. Moreover, some experiments measure the SC gap while others are sensitive to the gap and coherence effects. This issue must be kept in mind when interpreting results from different types of experiments.

1.1 Tunneling Spectroscopy

Tunneling spectroscopy is based on the quantum mechanical tunneling of electrons between two electrodes separated by a thin barrier. When a voltage bias is applied to one electrode with respect to the other, its chemical potential shifts with respect to that of the second electrode. Electrons can now tunnel from the filled states in one electrode to empty states in the other. Within the independent particle approximation, the tunneling current from electrode 1 to electrode 2 is

$$I = A|T|^2 \int_{-\infty}^{\infty} N_1(E)N_2(E+eV)[f(E) - f(E+eV)]dE \tag{1.3}$$

where A is a constant of proportionality, T is a constant tunneling matrix element, $N(E)$ is the density of states in the electrode and $f(E)$ is the Fermi-Dirac distribution function [1].

When both electrodes are normal metals, Eq. 1.3 gives the tunneling current as

$$I_{nn} = A|T|^2 N_1(0)N_2(0)eV \equiv G_{nn}V \tag{1.4}$$

so that the junction is ohmic. The differential conductance G_{nn}=dI_{nn}/dV is a constant independent of voltage. This is not surprising because in this simple calculation it is assumed that, for voltage biases much less than the Fermi energy, the density

of states is essentially constant near the Fermi energy. More sophisticated calculations using the independent-particle model which do not assume a constant $N(E)$, give the surprising result that the density of states does not enter the expression for the differential conductance. This is because in the independent particle model the density of state term is cancelled by the particle velocity term [34]. However, it is possible that in a strongly correlated electronic system, the differential conductance may give partial information about the density of states. No definitive theory of tunneling in strongly correlated electronic systems exists. However, in some cases, partial gaps in the differential conductance have been observed in chromium (antiferromagnetic gap [35]) and in $NbSe_2$(charge density wave gap [36]).

If one of the electrodes is a superconductor, then the application of many-body field theory shows that the differential conductance is proportional to the density of states in the superconductor [2]. One assumes that the normal metal counter-electrode has a well-behaved almost constant density of states near the Fermi energy. When the gap opens up in a superconductor, the quasi-particle states are pushed to the gap edge resulting in a singularity in the density of states:

$$\begin{aligned} \frac{N_S(E)}{N(0)} &= \frac{E}{(E^2-\Delta^2)^{1/2}} \ , \ E > \Delta \\ &= 0 \qquad\qquad\quad \ , \ E < \Delta \end{aligned} \tag{1.5}$$

There are no quasi-particle states within the gap i.e. $E < \Delta$. At low temperatures, the differential conductance directly measures the density of states [1]:

$$G_{NS} \propto N_S(e|V|) \tag{1.6}$$

Rigorous derivation of this result requires many-body calculations. Therefore, it is surprising that this correct result can be obtained from the equation for the current in the independent particle model (Eq. 1.3) by assuming a BCS density of states in the superconductor. This model was used by Giaever to explain his pioneering tunneling results on superconductors.

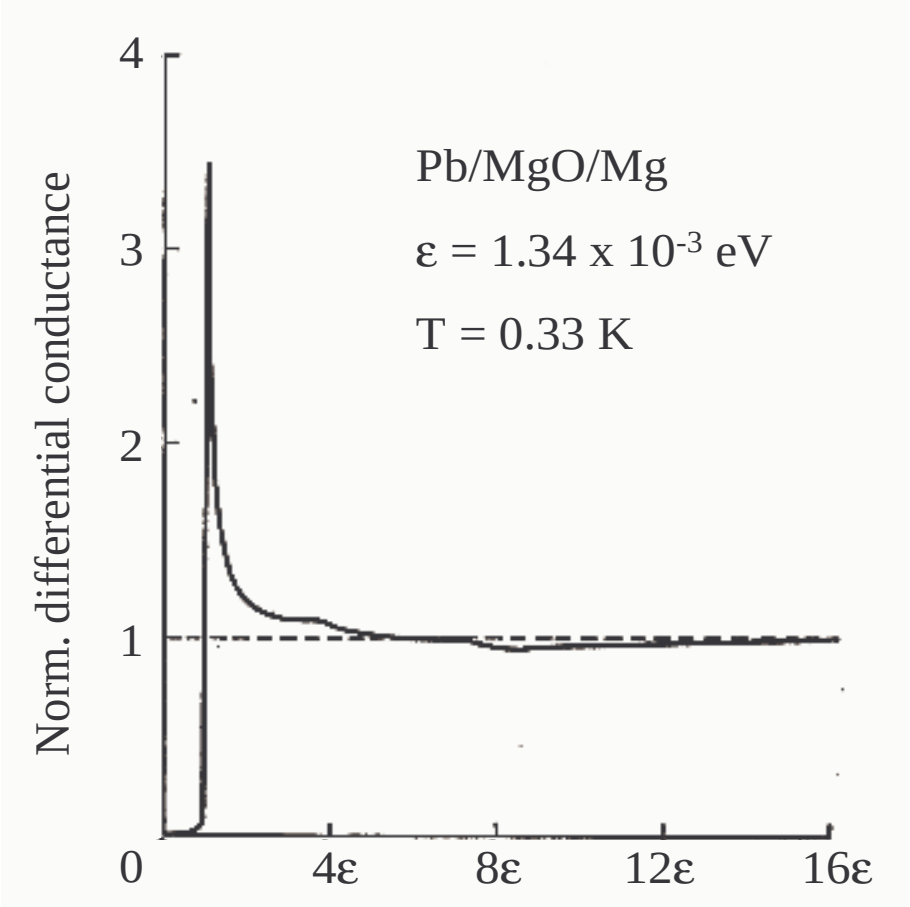

Figure 1.6: Tunneling spectrum of Pb in the SC state. ε denotes the SC gap of Pb (From Ref. [37])

Tunneling spectra are usually plotted as differential conductance on the vertical axis and the bias voltage on the horizontal axis. Sometimes, the current is plotted on the vertical axis instead of the differential conductance.

Soon after BCS published their theory, I. Giaever used tunneling spectroscopy on conventional superconductors to verify the SC density of states (see Fig. 1.6) and the temperature dependence of the gap predicted by BCS . He used Pb as the superconducting electrode and Al (and later Mg) as the normal electrode. The barrier was formed by a natural oxide layer on the Al and Mg films and Pb was evaporated over it.

When both electrodes are superconducting, the tunneling current is proportional

to a convolution of the density of states in both electrodes. Barrier tunneling using a superconducting counter-electrode that formed an oxide barrier was performed on the electron-doped cuprates and will be discussed in detail in Chapter 4.

The tunneling current between a normal and a superconducting electrode can be calculated using various techniques. A formulation by Blonder, Tinkham and Klapwijk (BTK) using the Bogolubov-deGennes equations has been used extensively in recent years to model current-voltage and differential conductance-voltage curves [38]. The BTK formulation is particularly attractive for modelling tunneling spectra obtained with point contacts because it employs a variable barrier parameter (Z) in the model. In point contact tunneling or point contact spectroscopy, a normal metal (superconductor) tip is brought into contact with the superconductor (normal metal). The barrier is usually a natural oxide on the normal metal and/or superconductor surface. By varying the pressure of the point contact, junctions with different barrier strengths can be obtained. Point contact spectrsocopy (PCS) on electron-doped cuprates is discussed in Chapter 3.

We have seen that in normal-insulator-superconductor (NIS) junctions with high Z, the differential conductance is proportional to the density of states. This is not the case if Z=0: a process called Andreev reflection leads to enhancement of the conductance for $E < \Delta$. When the bias voltage is less than the SC gap energy, an electron incident on a metal-superconductor interface cannot enter the superconductor because of the absence of single particle states in the gap. Therefore, it pairs up with another electron and enters the superconductor as a Cooper pair while a hole is reflected back into the normal metal (see Fig. 1.7). This process is called Andreev reflection and leads to an increase in the differential conductance for bias energies less than the gap energy. For intermediate Z, both single-electron tunneling and Andreev reflection processes contribute to the differential conductance.

Tunneling spectroscopy with high barrier junctions and point contact junctions has been extensively employed to study the SC gap in HTSC. The short coherence

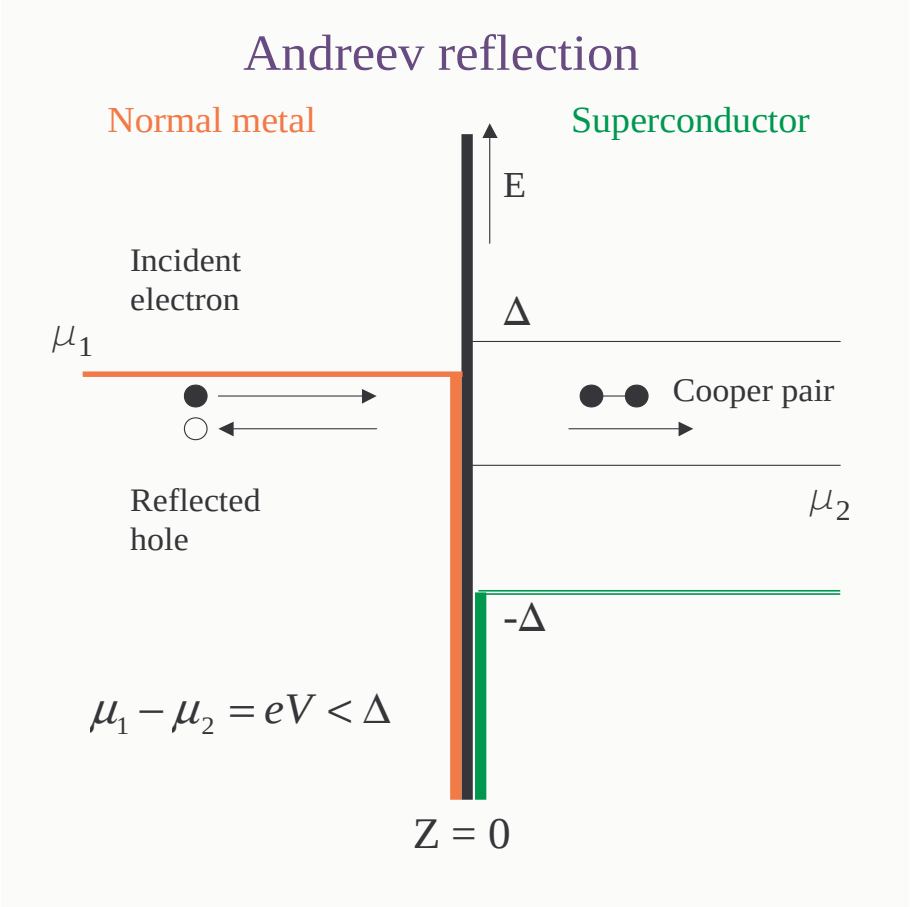

Figure 1.7: Andreev reflection

lengths of HTSC makes tunneling spectroscopy very sensitive to the surface quality of these materials and the yield of good junctions has been low. Tunnneling spectroscopy has probably the best energy resolution compared to other spectroscopic probes. In principle, it can be used to map the momentum dependence of the SC gap provided atomically smooth surfaces of various orientations. However, it is not possible to get such smooth surfaces of different orientations for HTSC without resorting to polishing techniques which in turn can adversely alter surface properties. Therefore, tunneling spectroscopy gives only limited information about momentum dependence of the gap.

One must note that tunneling spectroscopy is sensitive to the phase of the order parameter even when the junction interface is rough. For example, in *d*-wave super-

conductors the phase change of the gap leads to the formation of bound states at the Fermi energy for most surface orientations. This leads to an increase in tunneling conductance at zero voltage bias and it has been observed in several hole-doped HTSC, especially in $YBa_2Cu_3O_{7-\delta}$ (YBCO) [39, 40].

1.2 Raman Spectroscopy

Since its discovery in 1928 by C. V. Raman, the Raman effect has been widely employed to study elementary excitations (e.g. phonons, magnons, quasiparticles) in solids, liquids and gases [41]. In this thesis, the primary focus is on Raman scattering from electronic excitations in the electron-doped HTSC. Raman scattering means inelastic scattering of photons from elementary excitations, so that the scattered photon has a different energy from the incident photon. This difference in energy is imparted to the system being probed with the photon field in the visible range provided by a laser. The frequency shift of the scattered photon with respect to the incident photon is measured: it is called the Raman shift and is plotted on the horizontal axis. The intensity of the scattered photons is also measured and it is proportional to the differential scattering cross-section. The Raman response function (or Raman susceptibility) is obtained after the scattering intensity is normalized by the thermal Bose factor, and is plotted on the vertical axis [42].

Electronic Raman scattering from s-wave superconductors is expected to show no scattering intensity in the spectrum for energy shifts less than the SC gap 2Δ (the factor 2 comes because a bound pair of electrons need to be separated) [43]. Owing to the singularity in the single particle density of states at the gap edge, the spectrum is expected to show a peak near 2Δ (see Fig. 1.8). This is a result of the type I BCS coherence factor. For the pair-breaking 2Δ peak (or coherence peak) to occur in a Raman spectrum, both long range phase coherence in the SC state and a singularity in the single particle density of states at Δ are required.

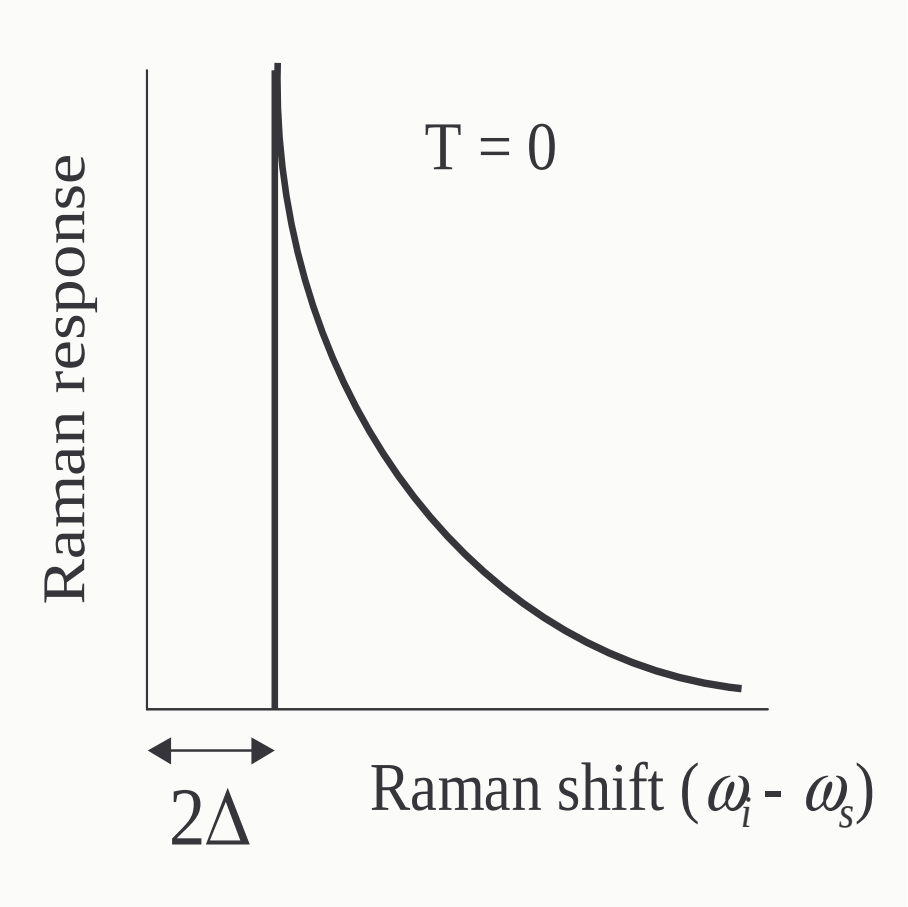

Figure 1.8: Schematic of the Raman Response in the SC state of an *s*-wave superconductor.

Electronic Raman Spectroscopy (ERS) has been used to observe SC gaps in both conventional and high-temperature superconductors. It took more than twenty years from the publication of BCS theory for the first observation of across-the-gap excitations in conventional superconductors. Since the cross-section of inelastic scattering of photons from electrons is very small, its observation required an improvement in the optical measuring equipment and sample quality. Excitations out of the SC state were first observed in $NbSe_2$ [44] and then in Nb, Nb_3Sn and V_3Si [45, 46].

Since the optical penetration depth in HTSC is of the order of thousands of angstroms, optical techniques like Raman spectroscopy are essentially bulk probes. Moreover, in addition to good energy resolution, Raman spectroscopy can give in-

formation about the momentum dependence of electronic properties (e.g. SC gap, scattering rates) by employing polarized light. One should note that Raman spectroscopy is not sensitive to the phase of the SC order parameter.

ERS in the non-SC state of cuprates also yields information about quasiparticle dynamics e.g. scattering rate and relative carrier density [47]. This is discussed in detail in Chapter 6.

The theoretical and experimental aspects of ERS and the results on conventional and hole-doped HTSC in the SC state are discussed in Chapter 5. The Raman data on electron-doped HTSC and its analysis is presented in Chapter 6.

Chapter 2

Samples

The growth and characterization procedures of samples of the electron-doped HTSC are described briefly in this chapter. Point contact spectroscopy (PCS) was performed on PCCO films and barrier tunneling spectroscopy was performed on single crystals of PCCO and NCCO. Single crystals of PCCO and NCCO and films of PCCO were used for Raman spectroscopy. High quality single crystals and films of the electron-doped HTSC have been grown in the Greene group for over a decade and details of growth and characterization methods can be found in several papers and theses [11, 12, 48, 49, 50]

2.1 Films

Pulsed Laser Deposition is used for growing films of PCCO. The basic idea is that intense, repetitive pulses of a laser beam are directed on a stoichiometric ceramic target. These create a plasma that consists of ions of elements in the target. This plasma impinges on a crystalline oriented substrate held at high temperatures. The ions get deposited on the substrate forming a crystalline oriented film with the same composition as the target.

Stoichiometric ceramic targets of PCCO are prepared from high purity powders of Pr_6O_{11}, CeO_2 and CuO. Another cerium source $(NH_4)_2Ce(NO_3)_6$ has occasion-

ally been used instead of CeO_2 with satisfactory results. The powders are weighed, mixed together thoroughly and heated at a high temperature. After the first heat treatment, the mixture is ground into powder and heated again. After the second heat treatment, the mixture is again ground into powder and the powder is compressed into a pellet which is sintered at high temperature. This pellet (target) is used for film growth.

The films for PCS were grown on (100) oriented lanthanum aluminate and (100) oriented strontium titanate substrates. These substrates have a close lattice match with the in-plane lattice parameters of PCCO and the films turn out to be c-axis oriented (c-axis is normal to the plane of the substrate). The deposition was carried out in 240 mTorr of N_2O gas with the substrate held at 770^{o}C. Films for PCS were grown to a thickness of about 3000 Å. The films were annealed in-situ in a vacuum of about 5×10^{-5} Torr at 770^{o}C for several minutes to uniformly remove oxygen and induce superconductivity. Cerium doping can be controlled to a high degree of accuracy in the films. The films are known to reproduce the stoichiometric composition of the ceramic target [12]. Optimally-doped (x=0.15), under-doped (x=0.13) and over-doped (x=0.17, 0.19) films were prepared.

The films were characterized with the following standard techniques. An AC susceptibility setup was used for the determination of T_c. All films that were used for the experiments had their T_c determined with the AC susceptibility setup (see Fig. 2.1 for a typical AC susceptibility measurement). Occasionally, a four-probe resistance measurement was performed on a piece of the film to check the transition into the SC state and the characteristic behavior of the normal state resistance. The behavior of the normal state resistance changes with doping. For example, for an under-doped film there is a characteristic upturn at about 60 K (Fig. 2.2a) while an over-doped film shows a monotonic decrease in resistance with decreasing temperature (Fig. 2.2b). X-ray diffraction was also performed on some of the films to check the orientation of the films. The expected peaks for c-axis oriented films

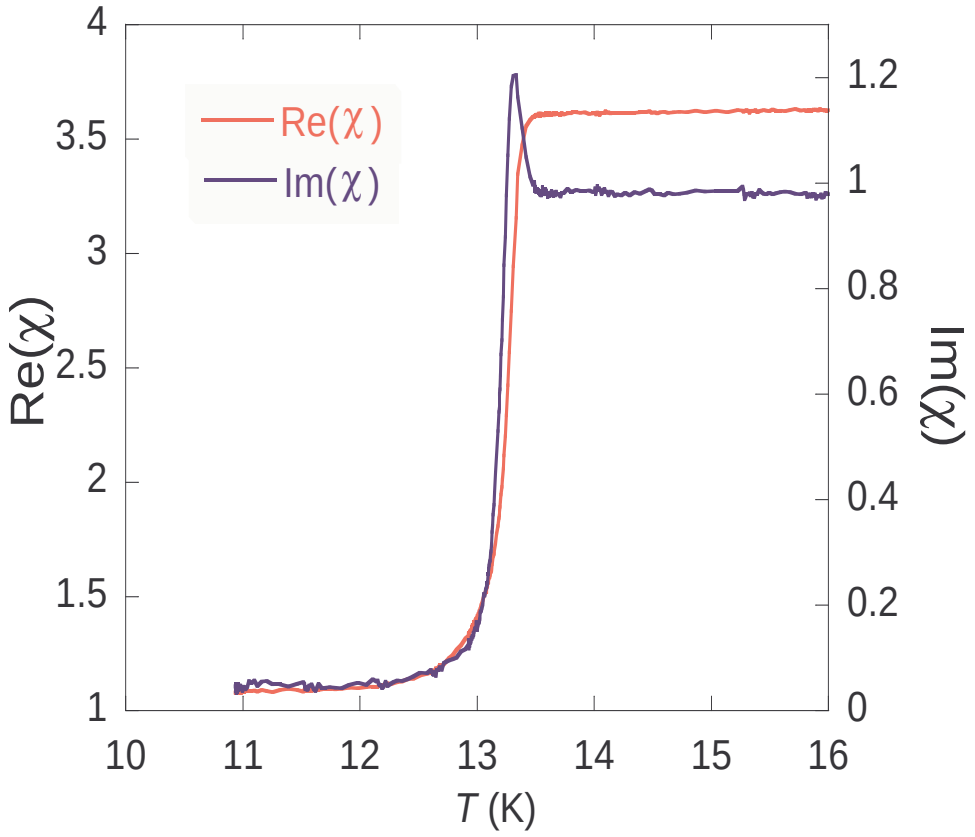

Figure 2.1: A plot of susceptibility vs. temperature showing superconducting transition of a thick ($\approx$ 8000 Å) PCCO film (x = 0.17). The T_c is given by the peak position of Im(χ).

occur in the scan (Fig. 2.3). There are additional weak peaks due to a few percent of (110) oriented phase. This phase is present in all PLD grown PCCO films [12, 26] and efforts to eliminate it completely have not been successful to date [12]. However, since this phase is present only in tiny amounts in the films, it does not affect the experiments presented in this thesis.

Single crystals are ideal for Raman measurements. However, it is difficult to control doping in crystals grown by the flux method. While crystals in the doping range x $\approx$ 0.15 to x $\approx$ 0.17 were obtained and will be discussed in the next section, crystals with dopings at the extreme ends of the SC phase x $\approx$ 0.13 and x $\approx$ 0.18

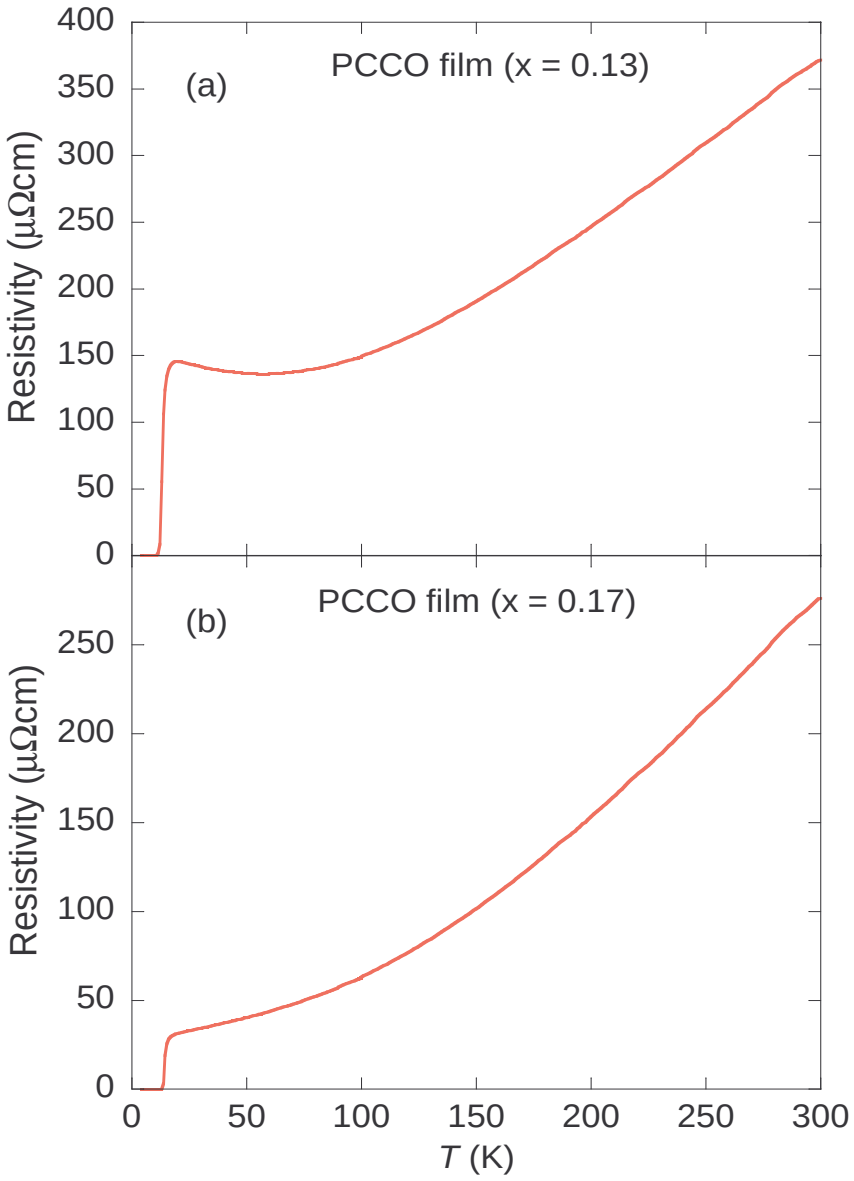

Figure 2.2: Plots of resistivity vs. temperature showing the variation of resistivity along with the superconducting transition. Panel (a) shows data on an under-doped PCCO film (x = 0.13) and panel (b) shows data on an over-doped PCCO film (x = 0.17).

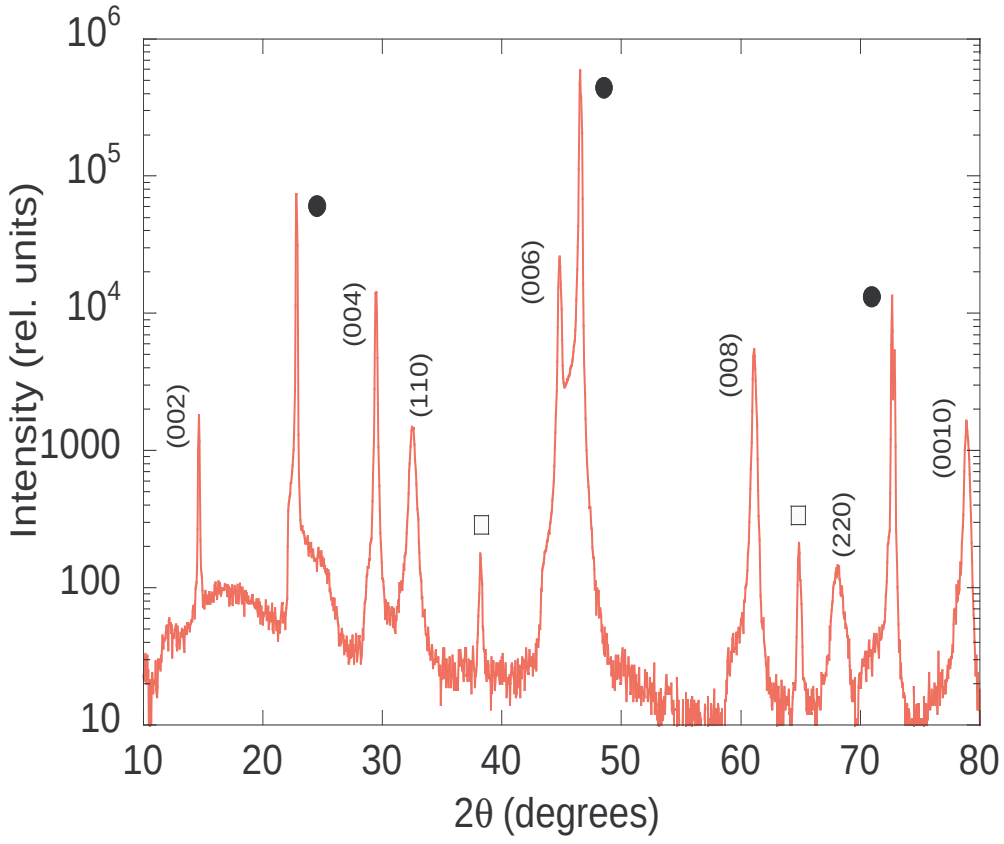

Figure 2.3: X-ray diffraction pattern of an over-doped PCCO film (x=0.17). Note the log scale on the vertical axis. The substrate (STO) peaks are marked by filled circles. The sample holder peaks are marked by empty squares. The PCCO peaks are labelled by the indices of the plane and diffraction order.

could not be obtained. In addition to performing Raman measurements on crystals, it was decided to do Raman measurements on c-axis oriented films because it is possible to prepare films with these extreme dopings. The growth of PCCO films for Raman Spectroscopy posed a major challenge for the reason given below. The optical penetration depth in the electron-doped cuprates near optimal doping is about 2000 Å for visible light. Since light intensity decays exponentially inside the sample, about 14 percent of light intensity will be present at a depth of 2000 Å. Therefore, the film has to be several times thicker than 2000 Å to ensure that light does not reach the substrate. Therefore, films about 8000 to 10000 Å are required to ensure that there is negligible substrate contribution to the Raman spectra. Films that are normally grown for transport and tunneling measurements are 2000 to 3000 Å thick. For growing much thicker films one has to ensure that the films preserve their c-axis orientation and that oxygen is uniformly removed during annealing. The thick films preserve their orientation and this was checked by Rutherford Backscattering (RBS). However, removing oxygen uniformly during annealing was a more difficult task. The annealing conditions of T=770^{o}C and pressure of 5×10^{-5} Torr are close to the phase stability line of the electron-doped cuprates [51]. A few minutes annealing for 3000 Å films was adequate for removing oxygen uniformly and did not result in decomposition. However, thicker films required longer annealing times (in the first approximation, annealing time is proportional to the square of the film thickness from a simple argument based on Einstein's diffusion equation). The longer annealing times at 770^{o}C led to decomposition of the PCCO. After experimenting with different annealing conditions, it was found that a lower temperature (700^{o}C) and longer annealing times were required to remove oxygen uniformly and at the same time preserve the integrity of the PCCO film.

The thick films were grown on strontium titanate substrate and are highly oriented and epitaxial. This was checked with Rutherford Backscattering which gave 10 percent backscattering fraction that is comparable to the results from high qual-

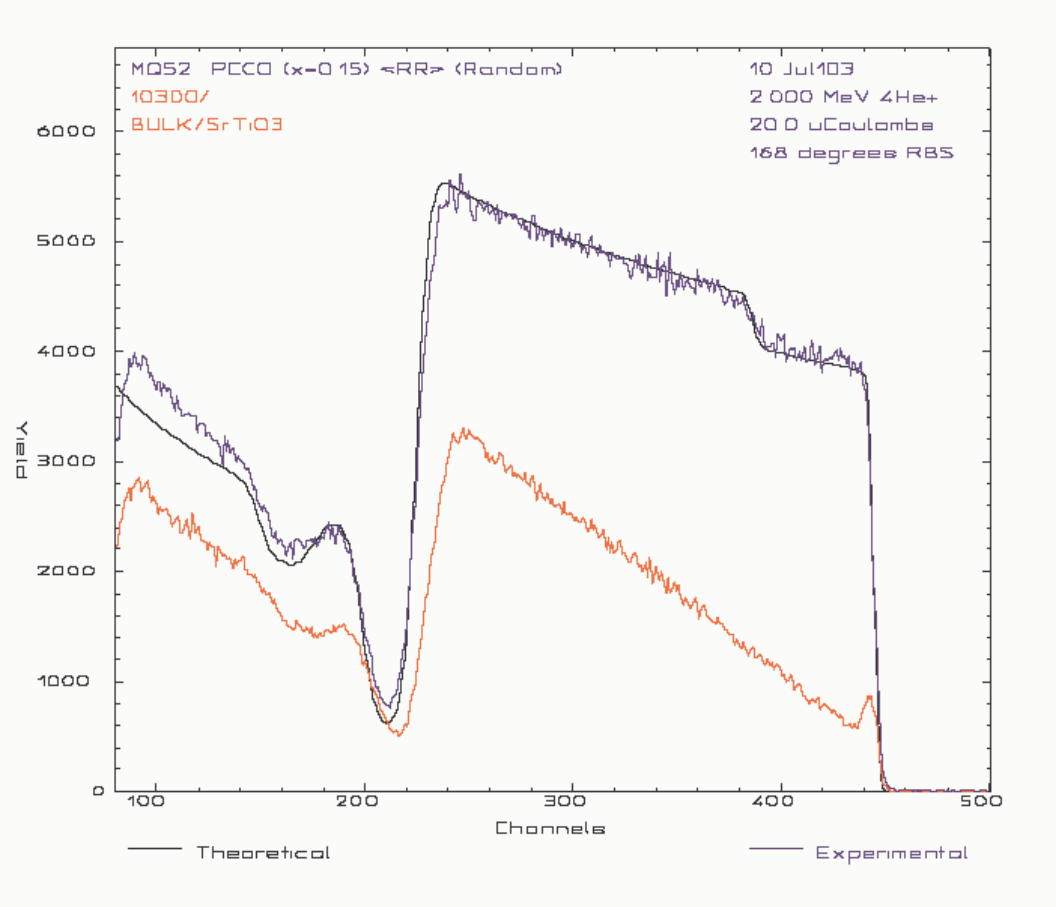

Figure 2.4: Rutherford Backscattering (RBS) data on a thick optimally-doped PCCO film. The film thickness measured by RBS is 10300 $\pm$ 1000 Å. The backscattering yield (vertical axis) for aligned film (red curve) is about 10 percent of the backscattering yield in random direction (blue curve). This backscattering yield percentage is calculated at 430 units along the horizontal axis.

ity 3000 Å thick PCCO films (see Fig. 2.4). The SC transition widths of the thick films are sharp, suggesting good homogeneity (see Fig. 2.1).

2.2 Crystals

Single crystals of PCCO and NCCO are grown by a directional solidification technique using CuO flux. Details of crystal growth can be found in Refs. [49, 50]. After growth, the crystals are annealed in an Ar atmosphere at elevated temperatures for about two days to induce superconductivity. The crystals used for tunneling and Raman experiments are trapezoid shaped platelets with in-plane dimensions of up to a few millimeters and thicknesses of about 20 to 30 μm. The crystals are single phase with no secondary phases visible in the X-ray diffraction data (Fig. 2.5). Their SC transitions are measured with a SQUID magnetometer. A typical SC transition for an optimally doped crystal is shown in Fig. 2.6.

It is easy to obtain optimally doped (x$\approx$0.15) PCCO and NCCO crystals with the flux-method. However, it turned out to be more difficult to obtain over-doped crystals with dopings within the SC phase. Much effort was devoted to synthesizing over-doped crystals and a few batches with Ce doping between 0.16 and 0.18 were obtained [50]. The Ce concentration of the crystals was measured with Wavelength Dispersive X-ray Spectroscopy (WDS). This method gives the Ce concentration (x) to better than $\pm$ 0.005.

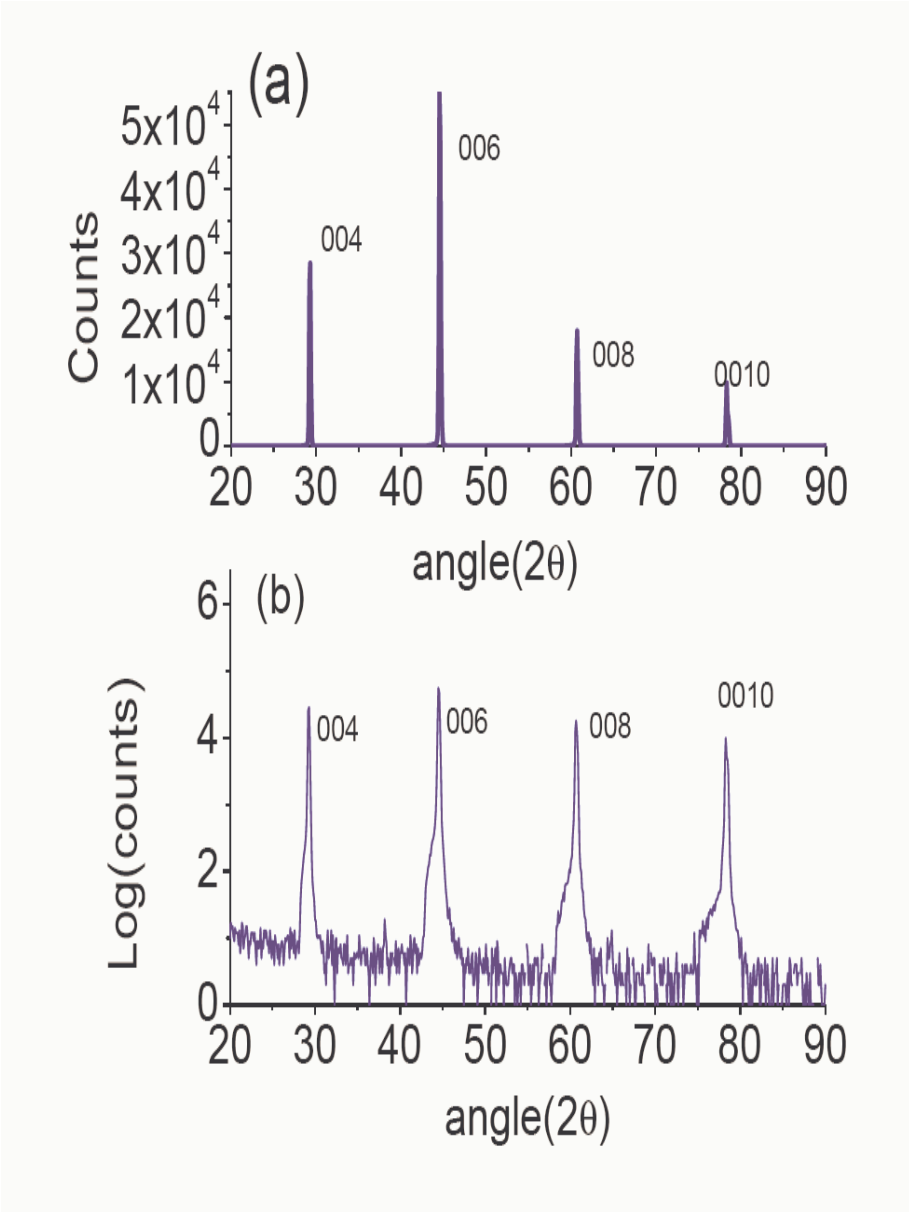

Figure 2.5: X-ray diffraction data on an optimally doped PCCO crystal on (a) linear scale (b) logarithmic scale. The absence of any unaccounted peak shows that the crystal is single phase. From Ref. [50]

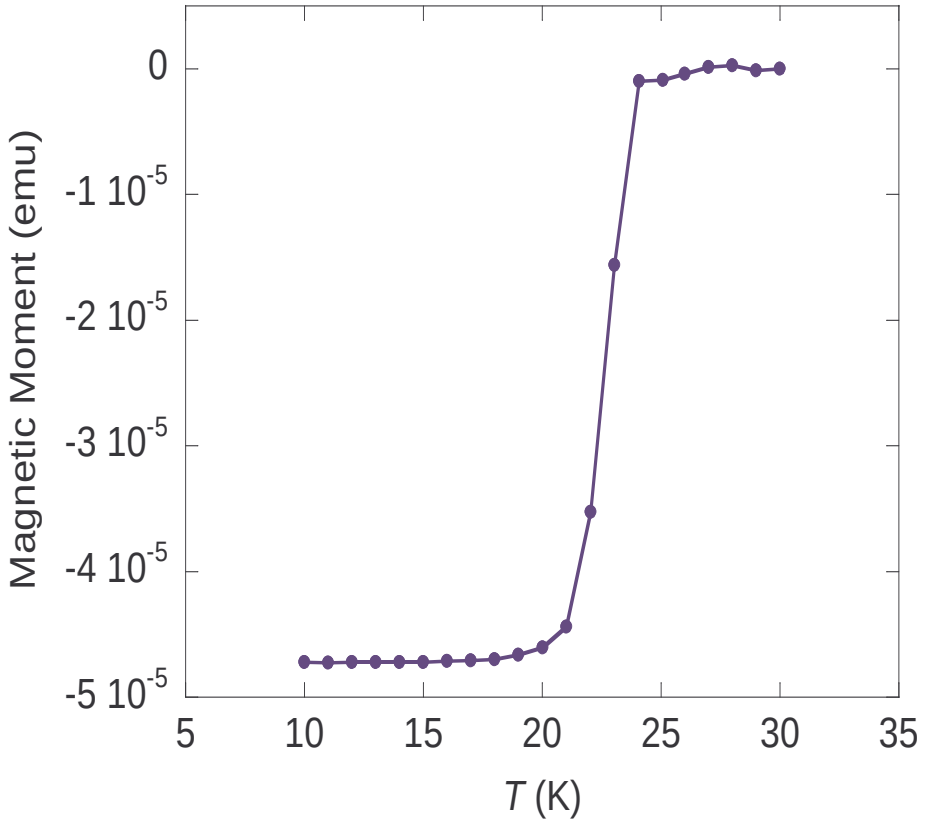

Figure 2.6: Zero field cooled magnetization data of an optimally doped PCCO crystal showing the SC transition.

Chapter 3

Point Contact Spectroscopy

Point Contact Spectroscopy (PCS) data is presented and discussed in this chapter. This chapter begins with a background discussion and motivation for PCS on the electron-doped HTSC followed by a brief description of the Blonder-Tinkham-Klapwijk (BTK) model. The experimental method is discussed next followed by presentation and discussion of the data.

3.1 Introduction

Point contacts between a normal metal and a superconductor have been extensively employed to probe the quasiparticle states of superconductors near the Fermi energy. Point contact spectroscopy experiments have also been done to investigate the pairing symmetry of superconductors and the presence or absence of nodes in the superconducting order parameter [52]. In particular, in the hole-doped (p-doped) copper oxide high T_c superconductors, PCS and high barrier junction tunneling experiments have shown that the pairing symmetry is predominantly $d_{x^2-y^2}$ (d-wave) [53], strongly supporting the results of many other types of experiments [16]. Some of the tunneling experiments have even suggested a doping-dependent order parameter and the existence of a Quantum Critical Point near optimum doping [40]. In the electron doped (n-doped) HTSC, the prior PCS and tunneling data has been

more controversial and there is no consensus at present on the implications of the data. The reason is the absence of a zero bias conductance peak (ZBCP) due to Andreev bound states in the tunneling spectra [54, 28, 27] which argues against the presence of d-wave pairing symmetry while other types of experiments [18, 21, 22] support a d-wave pairing symmetry. In this thesis, more detailed PCS experiments on the electron-doped HTSC $Pr_{2-x}Ce_xCuO_4$ (PCCO) are presented in an attempt to better understand the pairing symmetry in these superconductors at all doping levels.

Several early tunneling spectroscopy and PCS experiments were performed on optimally-doped $Nd_{1.85}Ce_{0.15}CuO_4$ (NCCO) [54, 28, 27] to investigate the density of states and pairing symmetry of this compound. All these experiments revealed a gap-like feature (with "coherence" peaks near the maximum gap) in the conductance-voltage $G - V$ spectra of NCCO with no hint of a ZBCP due to Andreev bound states. This led to the conclusion that the pairing symmetry for NCCO was not d-wave but either conventional or anisotropic s-wave, in stark contrast to the hole-doped HTSCs. However, two other PCS and Scanning Tunneling Spectroscopy experiments observed a ZBCP in optimally-doped NCCO [55, 56]. Recent PCS data on under-doped PCCO provides convincing evidence for a ZBCP due to Andreev bound states [57]. In that work, evidence for a doping-dependent pairing symmetry was also presented.

Penetration depth experiments on NCCO also supported the s-wave scenario [58, 59, 60]. However, it was later realized by Cooper that the magnetic moment of the Nd^{3+} ions would influence these measurements and might point to a misleading conclusion [61]. Subsequent experiments on the related optimally-doped compound, PCCO [21, 22], which is not plagued by the magnetic moment problem, provide evidence for d-wave symmetry. However, other penetration depth experiments on optimally-doped PCCO and NCCO [23, 24] are more consistent with s-wave pairing symmetry. The work of Skinta *et al.* [24] also presents evidence for a doping

dependence of the pairing symmetry.

Strong evidence of d-wave symmetry for optimally-doped NCCO and PCCO was provided by the phase sensitive tri-crystal grain boundary junction experiment [18], angle-resolved photoemission (ARPES) measurements [14, 62] and Raman spectroscopy [19]. However, some of these experiments, like tunneling measurements, are sensitive to the surface of the sample and there is the issue that the surface may be different from the bulk. Moreover, the doping near the grain boundaries may be different from that in the bulk and could influence the results of the half-integer flux quantization and tunneling measurements employing grain boundary junctions. Measurements of bulk properties were expected to finally resolve the question of the pairing symmetry but the results have yet to converge. A very small residual linear term in thermal conductivity measurements of PCCO crystals is evidence for absence of nodes in the gap and does not lend support to a pure d-wave pairing symmetry [63]. Several explanations have been put forward for the absence of the residual linear term including the presence of a complex order parameter and localization of d-wave quasiparticles. The other bulk measurement, specific heat, argues in favor of dirty d-wave pairing symmetry [64]. The term 'dirty' refers to a superconductor in which the quasiparticle mean free path (l) is less than the coherence length (ξ) of the superconductor.

To summarize, despite strong evidence for a d-wave symmetry, there is no consensus on the nature of the pairing symmetry in optimally doped PCCO and NCCO. The most recent PCS and penetration depth data favors a doping-dependent pairing symmetry for these materials: d-wave for under-doped and s-wave for over-doped. In this thesis, an extensive investigation with PCS on PCCO thin films below their superconducting transition temperatures (T_c) was carried out. The $G - V$ characteristics as a function of cerium doping, magnetic field and barrier strength (Z) were obtained.

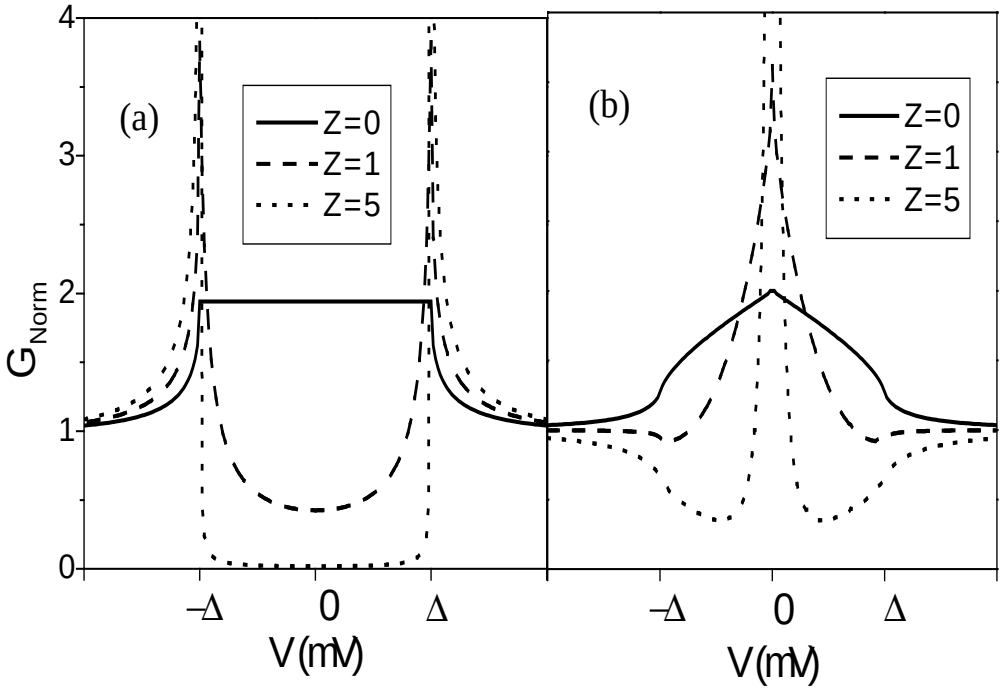

Figure 3.1: (a) Calculated $G - V$ curves for an s-wave superconductor at zero Kelvin using the BTK model (Ref. [38]). (b) Calculated $G - V$ curves for a d-wave superconductor at zero Kelvin for tunneling into (110) orientation (Ref. [65]).

3.2 Theory

The theory of quasiparticle transport in a point contact junction between a normal metal and a conventional BCS-type superconductor has been developed by Blonder, Tinkham and Klapwijk (BTK) [38]. In the BTK model, the superconductor is assumed to have an isotropic gap in momentum space. The barrier between the normal metal and superconductor is modelled by a delta function. The strength of the delta function is characterized by a dimensionless parameter Z. The $Z = 0$ limit signifies a completely transparent junction while $Z >> 1$ is the tunneling limit. Fig. 3.1a shows calculated conductance-voltage ($G - V$) characteristics for different barrier strengths. This model has been very successful in explaining the features of the $G - V$ spectra obtained for point contact spectroscopy in conventional s-

wave superconductors [66]. A major achievement of the BTK model is the unified treatment of the tunneling, transparent and intermediate regimes encountered in point contact junctions.

The BTK model has been modified by Tanaka and Kashiwaya [65] for PCS and tunneling spectroscopy in superconductors with *d*-wave symmetry of the order parameter. The gap in a superconductor with *d*-wave symmetry is of the form $\Delta_{\mathbf{k}}=\Delta_0 \mathrm{Cos}(2\theta_{\mathbf{k}})$ where $\theta_{\mathbf{k}}$ is the angle of a wave vector on the Fermi surface relative to [100]. The order parameter is anisotropic and changes sign in momentum space. Constructive interference between the electron-like and hole-like quasiparticles, which experience different signs of the order parameter, results in formation of surface bound states at the Fermi energy [67]. These surface bound states are also referred to in the literature as Andreev bound states and lead to enhancement of tunneling conductance at zero bias. The zero bias conductance peak (ZBCP) due to Andreev bound states is expected for quasiparticle injection into the *ab*-plane for all surfaces except (100) and (010). The ZBCP reaches maximum height for tunneling into (110) family of planes and Fig. 3.1b shows the calculated $G-V$ spectra as a function of Z for such case. The $G-V$ spectra in *d*-wave superconductors are direction-dependent assuming a specular interface between the normal metal and superconductor. However, in practice the surface of the superconductor is rough on the atomic scale and this results in contribution to the quasiparticle current from facets of various orientations. When the effect of surface roughness is taken into account [68], the $G-V$ spectra for quasiparticle injection into (100) and (010) planes also exhibit a ZBCP. ZBCPs have been observed in hole-doped HTSC, most notably and consistently in $YBa_2Cu_3O_{7-\delta}$ (YBCO) for tunneling into (100) and (110) orientations [40, 69, 39].

The order parameter symmetry may be more complicated than simply *s*-wave or *d*-wave, especially at the surface. This is of relevance because PCS essentially probes surface electronic states. The theory for quasiparticle transport in junctions

on superconductors with more complex pairing symmetries, for example, anisotropic s-wave, extended s-wave and $d_{x^2-y^2} + is$ $(d + is)$ has also been developed [70].

3.3 Experimental method

As discussed earlier in the "Samples" chapter, PCCO thin films were used for PCS. We have grown c-axis oriented PCCO thin films on strontium titanate and lanthanum aluminate substrates using pulsed laser deposition. Details of film growth have been described earlier. Superconducting thin films of PCCO with cerium concentrations of 0.13 (under-doped), 0.15 (optimally-doped), 0.17 and 0.19 (over-doped) were grown. The films have a thickness of 2500-3000 Å. The films were characterized by resistivity, AC susceptibility and X-ray diffraction measurements. The T_c for the films as determined from AC susceptibility and resistivity measurements are in the range 12 ± 1 K for under-doped films (x=0.13), 21 ± 0.5 K for optimally doped (x=0.15) films, 14 ± 1 K for over-doped (x=0.17) films and 7 ± 1 K for over-doped (x=0.19) films.

The 'spear on anvil' technique is widely used for making the point contact junction. A sharp metal tip is carefully brought into contact with the superconductor and the barrier strength is controlled by varying the pressure of the contact with a screw mechanism or a transducer (see, for example, the reviews in Ref. [71, 72]). In some cases, the sharp tip of a superconducting material has been employed with the normal metal as the counter electrode [66]. However, this method is difficult to implement in our experiment for the following reasons. Only c-axis superconducting PCCO thin films can be grown. Attempts at growing a-axis and (110) oriented superconducting PCCO films have not been successful. Since it is required to inject current into the *ab*-plane of this material and the thickness of the films is only 3000 Å, a great deal of difficulty is encountered, not only in positioning the normal metal tip on the edge of the film, but also in varying the contact pressure without the tip

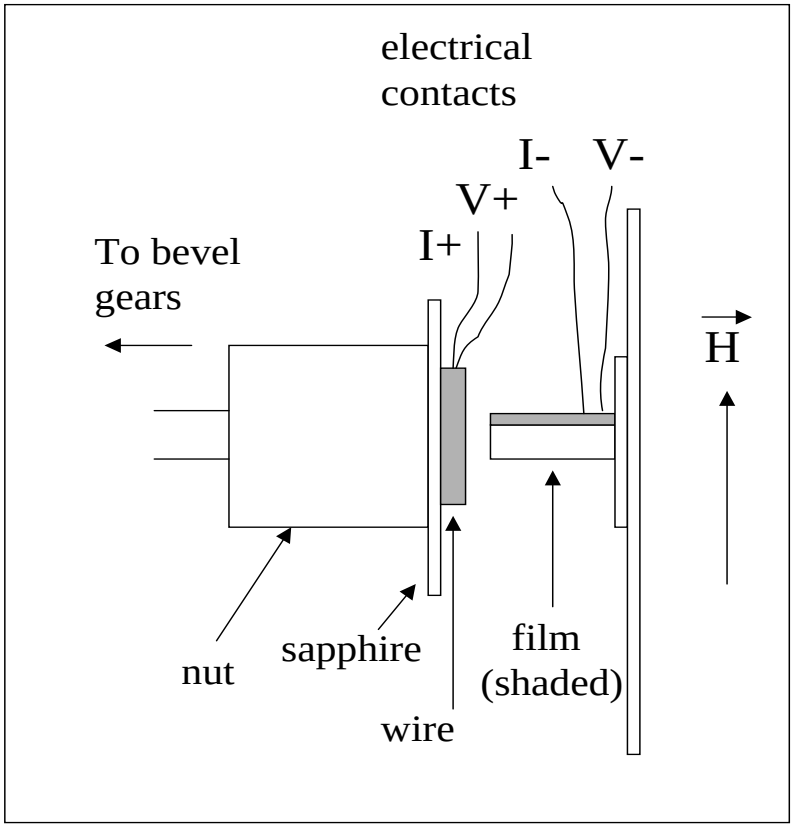

Figure 3.2: A schematic side view of our point contact method.

slipping off the film edge. Hence, an alternative technique for PCS in the *ab*-plane of thin films was devised and a new probe was designed and constructed for this purpose. Also note that a variation of this alternative method has been employed successfully in the past for PCS on superconductors [73].

A schematic side view of our point contact technique is depicted in Fig. 3.2. The film is cleaved in air to expose a fresh edge, electrical contacts on the film are made with Ag-In and it is glued with a quick-setting epoxy to a sapphire base. The film is placed in our PCS probe and a Au or Pt-Rh alloy wire of $0.25mm$ diameter, oriented perpendicular to the plane of the film, is carefully brought into contact with the cleaved edge of the film. The point contact junction is formed between the wire and the sharp edge of the film (see Fig. 3.3). The PCS probe is placed in a

Helium-4 bath which can be pumped down to 1.4 K. In order to study the effect of the magnetic field on the point contact spectra and to drive the PCCO into the normal state, the film is placed with its ab-plane perpendicular to the magnetic field. In this orientation the H_{c2} of the optimally-doped PCCO films is about 8 T (at 1.4 K) determined by resistivity measurements. This arrangement ensures that the film goes into the normal state at fields achievable in our laboratory. Therefore, a bevel gear arrangement is required to change the direction of motion for the point contact to be made. The Au or Pt-Rh wire is glued to a sapphire piece which in turn is glued to the threaded 'nut' on the shaft. The bevel gears can be rotated from outside of the Helium-4 bath. When the bevel gears rotate, the 'nut' along with the wire moves towards the edge of the film. The point contact can be made this way and the pressure of the contact can also be varied to obtain junctions with different barrier strengths. A high pitch anti-backlash worm gear arrangement at the top part of the probe outside the Helium-4 bath ensures that the distance between the wire and the film edge can be controlled to sub-micron precision. One important advantage of this method over the 'spear on anvil' method is that the point contact is relatively stable against mechanical perturbations because the wire is also supported by the edge of the substrate. Four probe measurements were made to obtain the current-voltage ($I-V$) characteristics of our junctions. The $I-V$ data is numerically differentiated to obtain the differential conductance ($G = dI/dV$). A standard lock-in (or derivative) technique was also used to obtain the $G-V$ spectra directly [74].

3.4 Results and Discussion

Since our method of making point contact is unconventional, we decided to demonstrate its validity and effectiveness by doing PCS on optimally-doped c-axis oriented $YBa_2Cu_3O_{7-\delta}$ (YBCO) thin films in the same configuration that we have

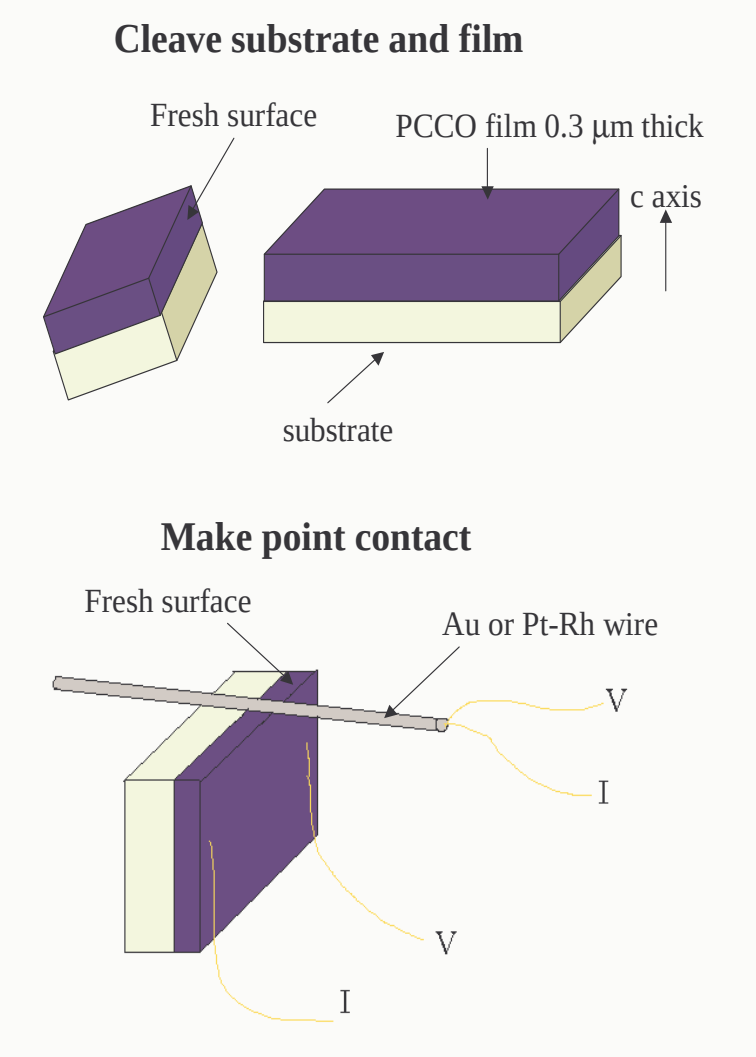

Figure 3.3: Procedure for making point contact junction. The film is cleaved and the wire is brought into contact with the fresh PCCO surface.

used for PCS on PCCO. The reasons for choosing YBCO for this purpose are that YBCO is an HTSC like PCCO and there is a consensus that the pairing symmetry of optimally-doped YBCO is predominantly d-wave and a ZBCP due to Andreev bound states has been observed in tunnel junctions and point contact junctions [40, 39, 75, 76]. The YBCO films have a thickness of 2000 Å and were grown on strontium titanate and neodymium gallium oxide substrates. The films have T_c in the range 89.5 $\pm$ 0.5 K. Since the $G-V$ spectra for a superconductor with d-wave pairing symmetry are orientation-dependent, the films were cleaved in different directions. However, we find no major difference in the features of the $G-V$ spectra for different cleavage orientations which suggests that surface roughness at the atomic scale leads to averaging of contributions from facets oriented in various directions.

Figure 3.4 shows the $G-V$ characteristics for point contact spectroscopy into the ab-plane of YBCO with Pt-Rh alloy wire as the counter-electrode. One can see from the zero field data that the width of the ZBCP is 6 meV and the "coherence" peaks caused by the SC energy gap appear at the accepted gap value of 18 meV. This is qualitatively similar to what is observed in PCS and Scanning Tunneling Spectroscopy on YBCO thin films and crystals [75, 76] and confirms the validity and effectiveness of our point contact method.

We also studied the effect of c-axis oriented magnetic field on the ZBCP as shown in Fig. 3.4. We saw no splitting of the ZBCP at low fields unlike what has been reported for tunnel junctions [40, 39]. We observe that the peak splits explicitly in a magnetic field of 8 T. The origin of the ZBCP splitting in YBCO is still a matter of debate [40, 39]. However, splitting of the ZBCP in a magnetic field has not been observed in other tunneling experiments [77]. Two of the several possible reasons for the absence of splitting of the ZBCP at low fields are that the orientation of the films and surface morphologies of the junction interface are different from the tunneling experiments in Ref. [40, 39]. In our experiment, the magnetic field is along the c-axis and perpendicular to the plane of film. Therefore, vortices enter the

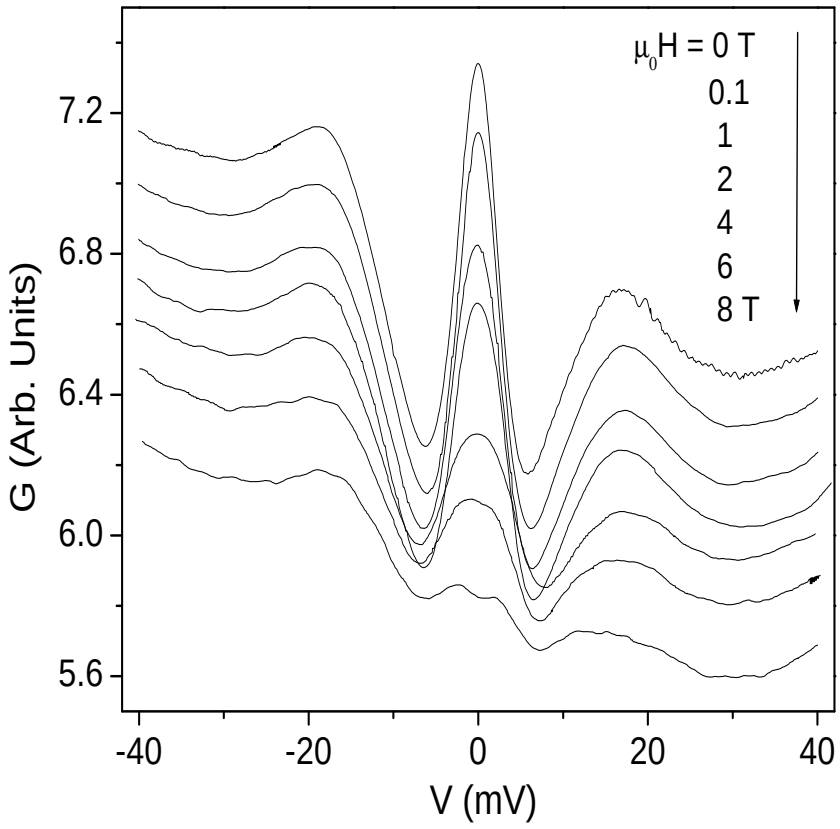

Figure 3.4: $G - V$ characteristics for optimally-doped YBCO taken at T=4.2 K in a magnetic field applied parallel to the c-axis of the film. The spectra are shifted for clarity. The junction resistance ($R_N \equiv 1/G_N$) at high voltage bias is 49 Ω.

film even at very low magnetic fields due to the large demagnetization factor and hence the Meissner currents become almost field independent. The entry of vortices into the film at low fields probably marginalizes the role that Meissner currents are expected to play in the splitting of the ZBCP [68]. Also, it is theorized that the splitting due to a sub-dominant order parameter (is or id_{xy}) may be suppressed for rough junction interfaces, especially if the sub-dominant order parameter is id_{xy} [78]. A third reason for the absence of splitting at low fields in our experiment may be that the splitting of the ZBCP is expected to occur above a critical field whose magnitude is proportional to the transmissivity of the junction [79]. Furthermore,

the transmission coefficient decreases exponentially with increasing barrier strength [74]. Since our point contact junction is more transparent than a tunnel junction, the fields for which we observe splitting are larger than those observed in experiments with tunnel junctions. We also note that the magnitude of the splitting is 2.1 meV at 8 T in our experiment which is in fairly good agreement with the magnitude of the splitting in Ref. [27]. The above discussion on the splitting of the ZBCP in a magnetic field has important implications for our data on under-doped PCCO that is presented later in this chapter.

We have performed a systematic and exhaustive study of PCS in the *ab*-plane of superconducting PCCO thin films of different cerium concentrations and have observed the $G - V$ spectra for different barrier strengths and in magnetic fields. The temperature dependence of the $G-V$ spectra was not investigated because point contact junctions are unstable against thermal expansion. Point contact junctions were made on films with different nominal cleavage orientations. More than fifty point contact junctions have been studied.

For PCS in PCCO films with 0.13 cerium concentration, we observe a ZBCP at low junction resistances and we have studied the ZBCP in a magnetic field applied normal to the ab-plane of the film. The data is shown in Fig. 3.5. The shape and magnitude of the ZBCP suggest that it originates due to Andreev bound states and we have fitted the zero field data to a calculated *d*-wave $G-V$ spectrum in Fig. 3.5a. Tunneling theory developed by Tanaka and Kashiwaya based on a generalized BTK model with a $d_{x^2-y^2}$ order parameter has been used to fit the data [65, 70]. The fit takes into account the temperature dependence of the Fermi function. Besides the gap value (Δ) and the barrier strength (Z), the fitting parameters include the quasiparticle lifetime broadening parameter (Γ), and the angle (α) between the normal to the junction interface and the direction of the maximum gap [100]. The ZBCP is completely suppressed for magnetic fields in excess of H_{c2} which is about 6 T, lending further support to the argument that the ZBCP is related to the

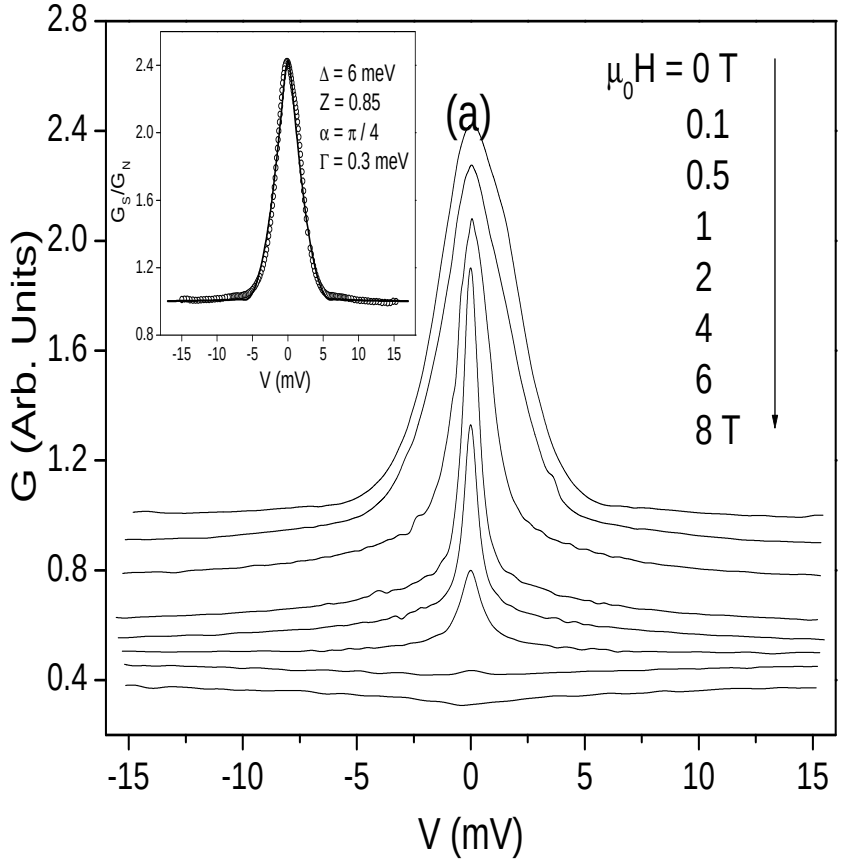

Figure 3.5: $G - V$ characteristics for under-doped PCCO at T = 1.43 K showing the variation of the ZBCP with magnetic field applied parallel to the c-axis. R_N for this junction is 9.8 Ω. The spectra are shifted for clarity. Inset(a): a fit of the zero field ZBCP data (circles) to the calculated conductance for a normal metal/$d_{x^2-y^2}$ superconductor (solid line). The fitting parameters are discussed in the text.

superconductivity of the PCCO. Compared to the $G - V$ spectra on YBCO, the ZBCP is not accompanied by a gap-like feature and "coherence" peaks because of the low barrier strength of this normal metal/PCCO junction. The magnitude and width of the ZBCP decreases with increasing magnetic field and the ZBCP does not split. The decrease in width and height of the ZBCP with magnetic field is probably due to the decrease in magnitude of the superconducting gap. But the exact origin of these changes is not understood at present. The possible reasons for the absence of splitting of the ZBCP in PCCO are the same as those advanced earlier for YBCO. Moreover, the fact that we do not observe a splitting of the ZBCP at all in PCCO may be due to a combination of two phenomena: low Z of our junction and the low H_{c2} of PCCO compared to YBCO. Therefore, the absence of splitting of the ZBCP in a magnetic field in under-doped PCCO is not unexpected.

Fig. 3.6 shows some representative $G-V$ spectra for PCCO $x = 0.13$ for different junction resistances. For a high junction resistance, which implies a higher barrier strength, we observe a gap-like feature with coherence peaks at the gap value. This can be seen more clearly in the inset (Fig. 3.6a). As the junction resistance is decreased, a ZBCP appears along with the gap-like feature shown in greater detail in the inset (Fig. 3.6b). For even lower junction resistance (and lower Z), a pronounced ZBCP is seen whose width is the same as the value of the gap as deduced from the fit in Fig. 3.5a. ZBCPs have been observed for low junction resistances in approximately 30 percent of our junctions and we believe the ZBCP appears when the normal metal electrode is able to penetrate the native surface barrier and make direct contact with the superconductor. For a junction with high barrier strength in a d-wave superconductor, theory predicts a sharp and pronounced ZBCP (see Fig. 3.1b) which we have never observed in our experiments on high Z junctions.

How do we explain this unusual Z-dependence of the $G - V$ spectra? One possibility is the presence of an induced order parameter at the surface for junctions with low transmission coefficient (i.e. high Z). This suggestion is based on the paper

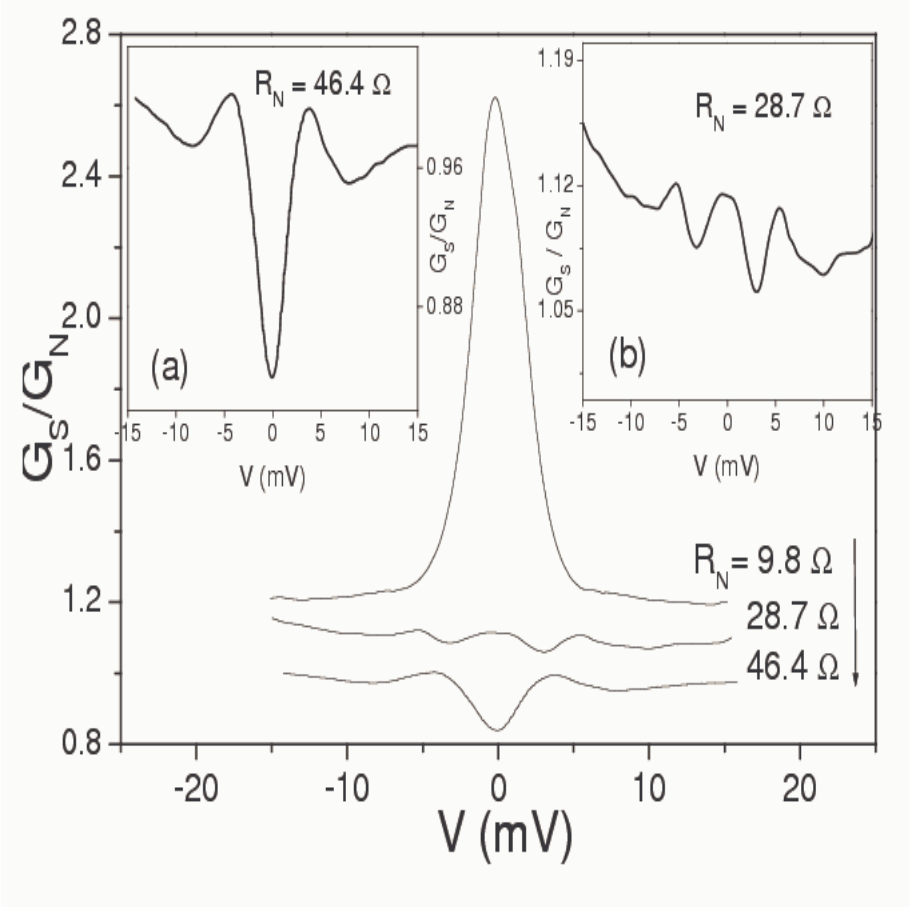

Figure 3.6: $G - V$ spectra for different junction resistances for under-doped PCCO at T = 1.43 K. The conductance in the superconducting state (G_S) is normalized to the conductance at high voltage bias (G_N). The spectra are shifted for clarity. Inset (a) shows in detail the high Z data with $R_N = 46.4\ \Omega$. Inset (b) shows in detail the spectrum with $R_N = 28.7\ \Omega$ where both the superconducting gap and ZBCP are clearly visible and this data can be compared with the zero field data for YBCO in Fig. 3.4.

by Tanuma *et al.* [80] who have proposed that for a high-Z junction in a d-wave superconductor, the $d_{x^2-y^2}$ order parameter is suppressed at the surface and the spectral weight is transferred to a sub-dominant is or id_{xy} order parameter. This effect is maximum for tunneling into (110) orientation of the junction interface. We believe that in the case of PCCO, the magnitude of this induced order parameter exceeds the bulk $d_{x^2-y^2}$ order parameter at the surface, which is plausible according to the theoretical calculations in Ref. [80]. Therefore, we attribute the gap-like feature in the high-Z limit to an induced order parameter whose magnitude ranges between 3 meV and 5 meV as estimated from the separation of the coherence peaks in several of the $G-V$ spectra (for example, see Fig. 3.6a). We note that this induced order parameter is not present in the low-Z junctions and the ZBCP we observe is due to the d-wave nature of the bulk order parameter whose magnitude from the fit in Fig. 3.5a is 6 meV. Another possible explanation for the absence of the ZBCP in junctions with high-Z is that disorder suppresses the ZBCP. This is based on the results of the experiment on tunnel junctions on YBCO in which the effect of disorder on the ZBCP was studied [81]. However, in that experiment, the gap-like feature disappears along with the ZBCP as disorder increases. Since a pronounced gap-like feature is seen in our high-Z data, we think it is unlikely that the absence of a ZBCP is solely due to disorder.

Although the simplest and most likely explanation of the ZBCPs in under-doped PCCO junctions is the d-wave pairing symmetry, we want to point out that ZBCPs due to Andreev bound states are predicted for other exotic symmetries (e.g. extended s-wave, $d+s$ with $d>s$) [65]. The surface orientation dependence of the $G-V$ spectra predicted for the above order parameters is different for each one but we are unable to distinguish between these by our experimental method because our $G-V$ spectra are an average of contributions from facets of various orientations on the atomic scale. The existence of roughness at the atomic scale is supported by our observation that we find no qualitative change in the spectra for quasiparticle

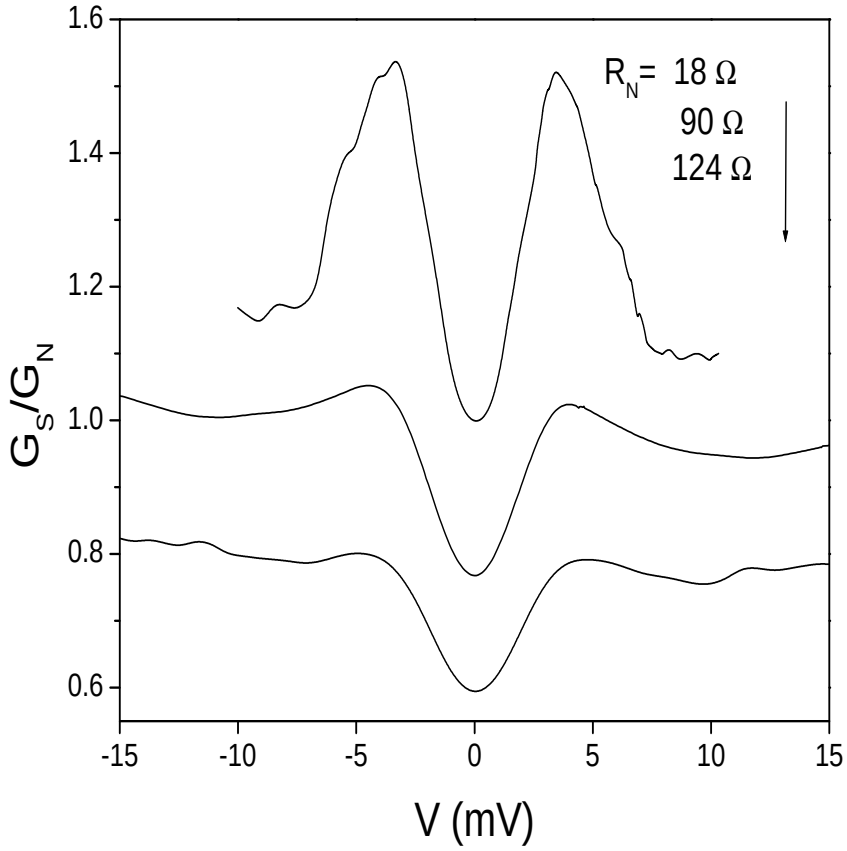

Figure 3.7: Normalized $G-V$ spectra for different junction resistances for optimally-doped PCCO at T = 1.43 K. The spectra are shifted for clarity.

injection into different surface orientations.

The point contact spectra for optimally-doped (x=0.15) and over-doped (x=0.17) PCCO for different junction resistances are shown in Fig. 3.7 and Fig. 3.8 respectively. The $G-V$ features are similar for these two doping levels and we will discuss these together. For high resistance junctions we see gap-like features with coherence peaks at the gap values. This is consistent with previous PCS and tunneling experiments on optimally-doped NCCO and PCCO [54, 28, 27] where no ZBCP was observed. For lower junction resistances and hence lower barrier strengths, we do not observe a ZBCP which suggests the absence of Andreev bound states at the Fermi energy. The shape of $G-V$ spectra are now influenced by Andreev reflections

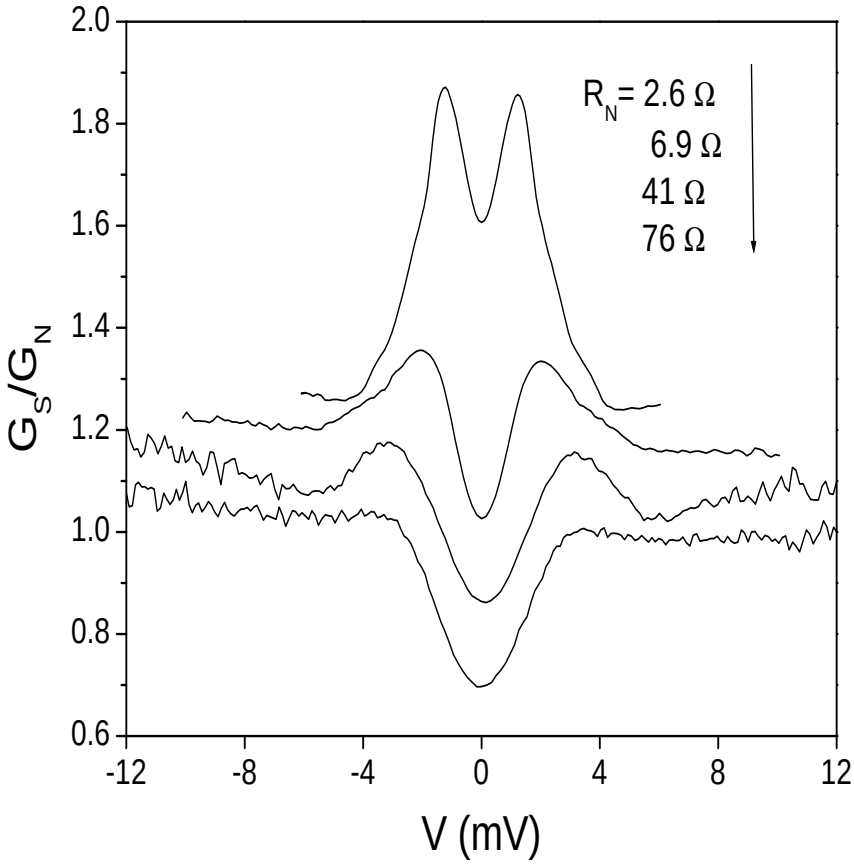

Figure 3.8: Normalized $G - V$ spectra for different junction resistances for over-doped (x=0.17) PCCO at T = 1.43 K. The spectra are shifted for clarity.

and qualitatively resemble those of s-wave superconductors in the low/intermediate Z limit (see Fig. 3.1a). In general, a dip in the conductance at zero bias in low Z junctions suggests absence of nodes in the order parameter [82]. Therefore, keeping in view the shape of our $G-V$ spectra for low Z junctions on under-doped, optimally-doped and over-doped PCCO, we propose a transition from a d-wave order parameter for under-doped PCCO to a nodeless gap for optimal and over-doped PCCO. As an example, we have fitted the $G-V$ data for the lowest junction resistance on over-doped PCCO to the generalized BTK model with isotropic gap as shown in Fig. 3.9a. A slightly better fit is obtained with a $d+is$ pairing symmetry calculation, with equal weights of the real and imaginary parts of the order parameter as shown in Fig. 3.9b. The fit with the $d+is$ order parameter is better because the sum of the squares of the differences between the data points and theory is less than for the fit with the s-wave gap. In calculating the best fit to the data, the lifetime broadening parameter (Γ) is kept as small as possible and the angular integral is taken over the full range $-\pi/2 < \theta < \pi/2$. Both fits include the effect of thermal broadening. The purpose of the fits is to show that in both models the low bias characteristics of the $G-V$ spectra are determined by the fully gapped nature of the order parameter. We also tried a fit to $d_{x^2-y^2}+id_{xy}$ ($d+id_{xy}$) pairing symmetry model with the same constraints on Γ and θ as in the $d+is$ model. However, given the physically reasonable constraints on Γ and θ, the data could not be fit to the $d+id_{xy}$ model.

Our data points to a transition in pairing symmetry with doping and this suggests the existence of a Quantum Critical Point at or near optimum doping. For d-wave superconductors, theoretical considerations limit the pairing symmetry transition across a Quantum Critical Point from d-wave to either $d+is$ or $d+id_{xy}$ [83]. Our low Z data on PCCO is more consistent with a d- to $d+is$ pairing symmetry transition across a Quantum Critical Point near optimum doping. A recent report also suggests a transition in pairing symmetry across a Quantum Critical Point near

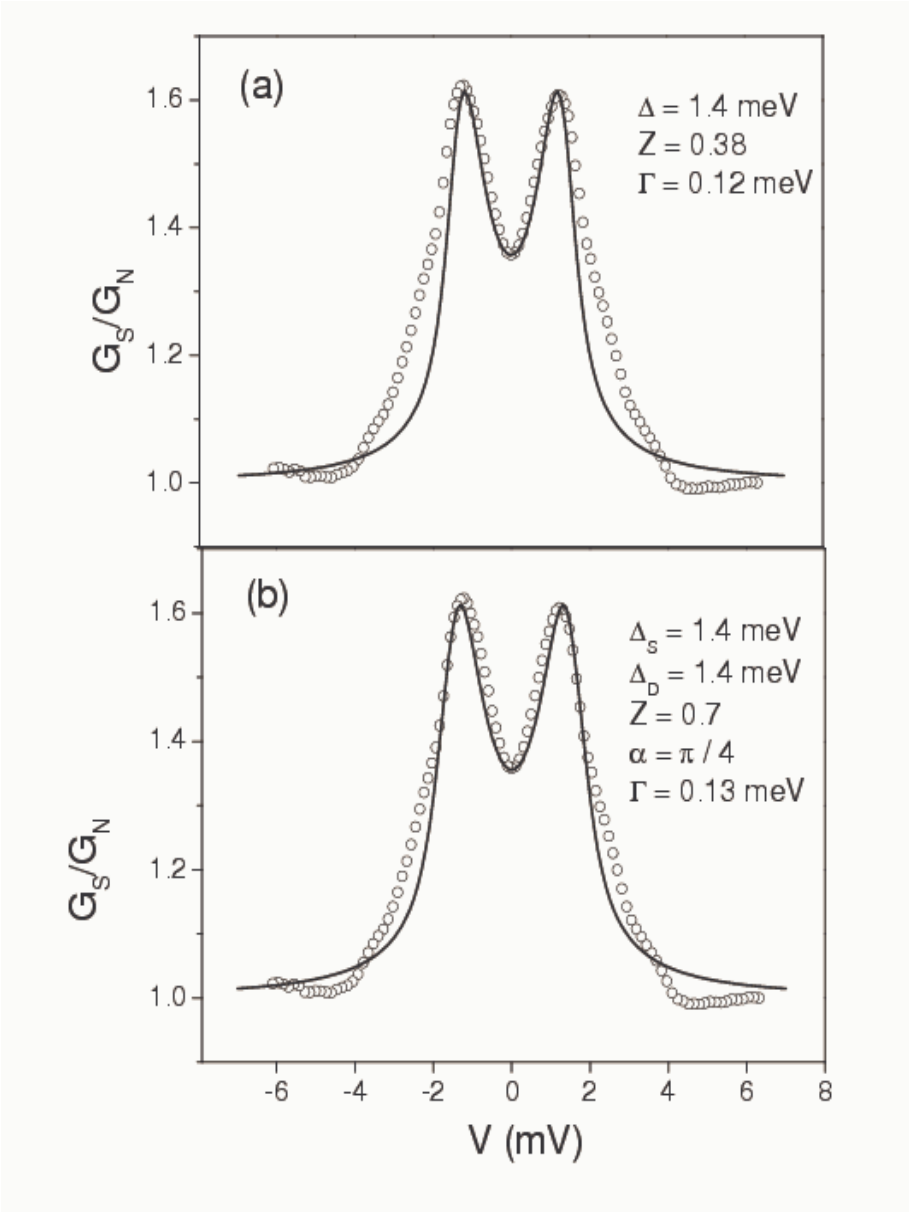

Figure 3.9: (a) A fit of the low resistance ($R_N = 2.6\ \Omega$) $G - V$ spectrum (circles) for over-doped (x=0.17) PCCO to the generalized BTK model with an isotropic gap (solid line).(b) A fit of the same data to $d + is$ pairing symmetry model. The fitting parameters are discussed in the text.

optimum doping in YBCO. [40]. Recent experimental and theoretical works on the electron-doped cuprates also support our view [30, 31, 32, 84].

It has been suggested that the proximity effect for transparent junctions on $d_{x^2-y^2}$ superconductors leads to an induced s-wave order parameter in the normal electrode [85, 86]. This effect is maximum for (100) or (010) surface orientations and does not occur for (110) orientation. If the absence of a ZBCP in our low Z data on optimally-doped and over-doped PCCO is attributed to an s-wave order parameter being induced in the normal electrode due to the proximity effect, then it is difficult to understand why this effect is not observed in our low Z junctions on under-doped PCCO. Therefore, we do not think our data can be explained by an s-wave order parameter induced by the proximity effect. Hence, the $d + is$ order parameter appears to be a property of the surface of optimally-doped and over-doped PCCO.

3.5 Normal State Gap

We have also studied the dependence of the $G - V$ spectra in the tunneling limit on the magnetic field applied perpendicular to the plane of the film (i.e. parallel to the c-axis of the film) and present our data in Fig. 3.10a and 3.10b. Note that the coherence peaks are completely suppressed about 4 T for optimally-doped PCCO and about 2 T for over-doped PCCO. These fields are less than the H_{c2} determined from resistivity measurements which is 8 T for optimally-doped PCCO and 4 T for over-doped PCCO. Notice that the magnitude of the superconducting gap decreases with increasing magnetic field and it evolves into a gap-like feature, qualitatively different from the superconducting gap, at $H \simeq H_{c2}$. We interpret this dip in the differential conductance near zero voltage bias as a normal state gap whose origin has not yet been determined conclusively. We also note that a weak normal state gap is observed in a low Z junction on an under-doped PCCO film (see Fig. 3.5 and

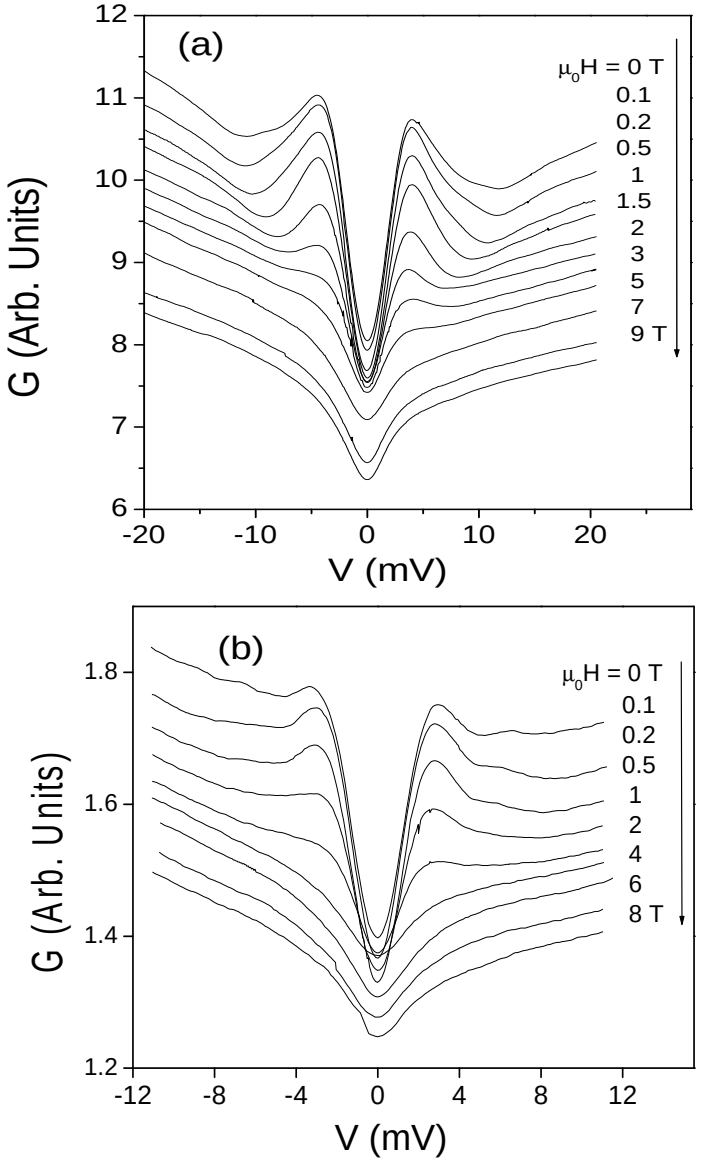

Figure 3.10: Variation of the $G-V$ characteristics of high resistance junctions with magnetic field applied parallel to the c-axis of the films. (a) Optimally-doped PCCO with $R_N = 91\ \Omega$ and (b) over-doped PCCO with $R_N = 57\ \Omega$. The measurements were done at T = 1.43 K. The spectra are shifted for clarity.

Ref. [87]).

A recent report on tunneling in PCCO grain boundary junctions suggests that the suppression of the differential conductance at zero voltage bias of the normal state gap (NSG) decreases with increasing Ce doping [88]. PCCO films with three dopings (0.13, 0.15 and 0.16) were studied. Based on the data from these three dopings alone, it was suggested that the NSG disappears at a doping of x=0.17 which is identified with a Quantum Critical Point within the superconducting dome. To establish the disappearance of the NSG, dopings equal to and greater than x=0.17 should have been studied in the above mentioned work and this was not done. Our tunneling data on x=0.17 PCCO films clearly suggests that the NSG is present at this doping (see Fig. 3.10).

Preliminary PCS data on an over-doped PCCO film with x=0.19 Ce doping (extreme end of the SC phase) suggests that the NSG is also present at this doping. The point contact junction is near the transparent limit (low Z) and Andreev reflection is observed (Fig. 3.11a). This data is qualitatively consistent with a fully gapped Fermi surface and this needs to be confirmed with quantitative fits. Upon application of a magnetic field greater than H_{c2}, Andreev reflection was suppressed and a weak NSG was observed (Fig. 3.11b). The magnitude of the suppression of the conductance at zero voltage bias may depend upon the barrier strength. Therefore, the rather weak NSG for PCCO (x=0.19) film may be due to a low Z junction. Recent tunnel junctions on over-doped (x=0.17 and x=0.19) films confirm the presence of the NSG at these high dopings [89].

Our PCS data can be used to detect the presence of the NSG. However, the magnitude of the suppression in G at zero bias ("depth" of NSG) depends on Z. Therefore, we need to get junctions with the same barrier strengths before we can determine from PCS data if the "depth" of the NSG feature changes with doping. It also appears from the PCS data that the energy scale (voltage bias) of the NSG does not change substantially with doping. This observation is in agreement with

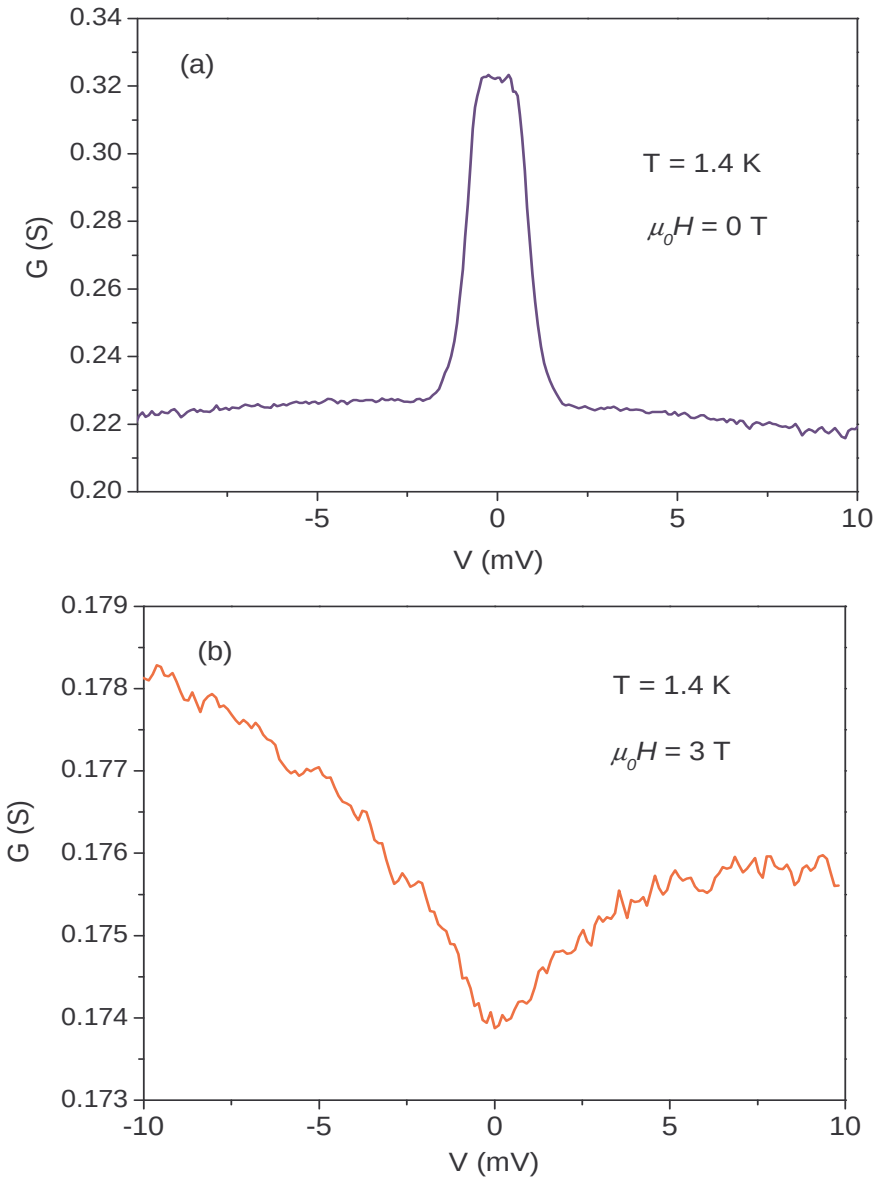

Figure 3.11: $G - V$ characteristics of a low Z junction on an over-doped PCCO (x=0.19) film (a) in zero magnetic field (b) in a magnetic field ($\mu_0 H = 3$ T) larger than H_{c2}.

Ref. [88]. The temperature dependence of the NSG will be discussed in the following chapter on high barrier tunnel junctions. The possible origin of the NSG will also be discussed in that chapter.

3.6 Ballistic and thermal regimes

Finally, we would like to comment on whether our point contact junctions are in the ballistic (or Sharvin) limit i.e. the contact radius (a) is much less than the mean free path (l) [90]. This is considered an important criterion for the validity of PCS. The Sharvin formalism was originally developed to model transport across a micro-constriction between two similar metals [91]. This formalism was extended by Wexler to the case where the micro-constriction has a ballistic as well as a thermal (Maxwell) part [92]. Both the Sharvin and Wexler formulas have been employed in previous works for calculating the contact radii for point contact junctions between a metal and an HTSC. However, there is much debate on whether the Sharvin and Wexler formulas are applicable in their present forms to a point contact junction between two materials with very different Fermi liquid parameters and resistivities [93, 94], as is the case with a normal metal and a high T_c superconductor. Moreover, since the high T_c superconductors have relatively short mean free paths (compared to conventional metals) of the order of hundreds of angstroms, the criterion for point contacts being in the Sharvin limit ($a << l$), as estimated from the Sharvin and Wexler formalisms, have rarely been strictly achieved. In most cases, the contact radius is comparable to the mean free path in the superconductor [57, 75, 95, 96]. Authors have explained this by either considering the less rigorous condition ($a < l$) as sufficient for a ballistic contact, or suggesting that the condition $a \approx l$ leads to a higher effective Z, or postulating the existence of several parallel ballistic contacts. Whatever the case may be, there is some agreement that if the point contact is dominated by the thermal part, its conductance will decrease appreciably at higher

voltage bias ($eV > \Delta$) due to localized heating [66, 90, 95, 97]. In our $G - V$ spectra, the conductance at higher voltage bias is either almost flat or increasing with voltage. Thus, we conclude that our point contact junctions are not in the Maxwell regime and the quasi-particle transport through the junctions is predominantly ballistic. This is a sufficient condition for energy-resolved spectroscopy of point contact junctions.

3.7 Summary

For *low barrier strength junctions* on under-doped PCCO, we observe a ZBCP and show that it is due to d-wave pairing symmetry. We do not observe a ZBCP in low Z PCS data on optimally-doped and over-doped PCCO and this indicates absence of nodes in the gap. Our data, along with theoretical considerations, indicates a $d + is$ pairing symmetry for optimally-doped and over-doped PCCO. We find that our data for low barrier strength junctions for all doping levels can be best explained by a d- to $d + is$ pairing symmetry transition across optimum doping.

We observe gap-like features for *high barrier strength junctions* for all doping levels. For high Z junctions on under-doped PCCO, we believe that the d-wave order parameter is suppressed at the surface and the spectral weight is transferred to an is order parameter which leads to gapped spectra. For high Z junctions on optimally-doped and over-doped PCCO, the gap-like features are due to a fully gapped Fermi surface. The data on low Z junctions on over-doped PCCO suggests that a $d + is$ order parameter leads to this nodeless and fully gapped Fermi surface. Indeed, data from all the previous PCS and tunneling experiments on NCCO and PCCO, which consistently showed a gap-like feature can be explained by an induced is order parameter at the surface of under-doped PCCO, and by an order parameter without nodes for optimally-doped and over-doped PCCO.

We have studied the $G-V$ spectra in magnetic fields up to and greater than H_{c2}

of PCCO. We find that the ZBCP in the $G-V$ spectra of under-doped PCCO does not split in magnetic fields up to H_{c2}. This may be due to one or more of the following reasons: immediate penetration of vortices into our films; surface roughness of our junctions; the high transmissivity of our junctions. For $H \geq H_{c2}$, we observe a gap-like feature in the normal state at the Fermi energy for all the doping levels that we have investigated in these experiments. The normal state gap is of the same order of magnitude as the superconducting gap but differs qualitatively from it. The normal state gap is at least an order of magnitude less than the pseudogap that has been observed in other experiments on NCCO [98, 99].

Chapter 4

Tunneling Spectroscopy

Tunneling between superconductor-insulator-superconductor (SIS) and normal metal-insulator-superconductor (NIS) junctions is described in this chapter. Tunnel junctions were prepared on PCCO and NCCO single crystals with Pb as the counterelectrode. Pb is known to react with the oxygen in the HTSC and forms an insulating oxide barrier [100].

4.1 NIS and SIS tunneling

The theory for NIS tunneling in superconductors with various symmetries of the SC gap has been described in the previous chapter. When both electrodes are superconducting, the tunneling spectrum will depend upon the gap symmetry of both superconductors. Here we consider two cases: the first is that both superconductors have s-wave symmetries, and the second is that one superconductor has s-wave symmetry and the other has d-wave symmetry. A big advantage of using a conventional s-wave superconductor as one of the electrodes is that one can check the quality of the junction by the zero bias conductance value in the SC state. Due to the s-wave gap, the conductance of a good junction at zero bias should be very small and will be given by BCS theory. One can also obtain an NIS junction by quenching the superconductivity of the s-wave superconductor (with lower T_c) by measuring the

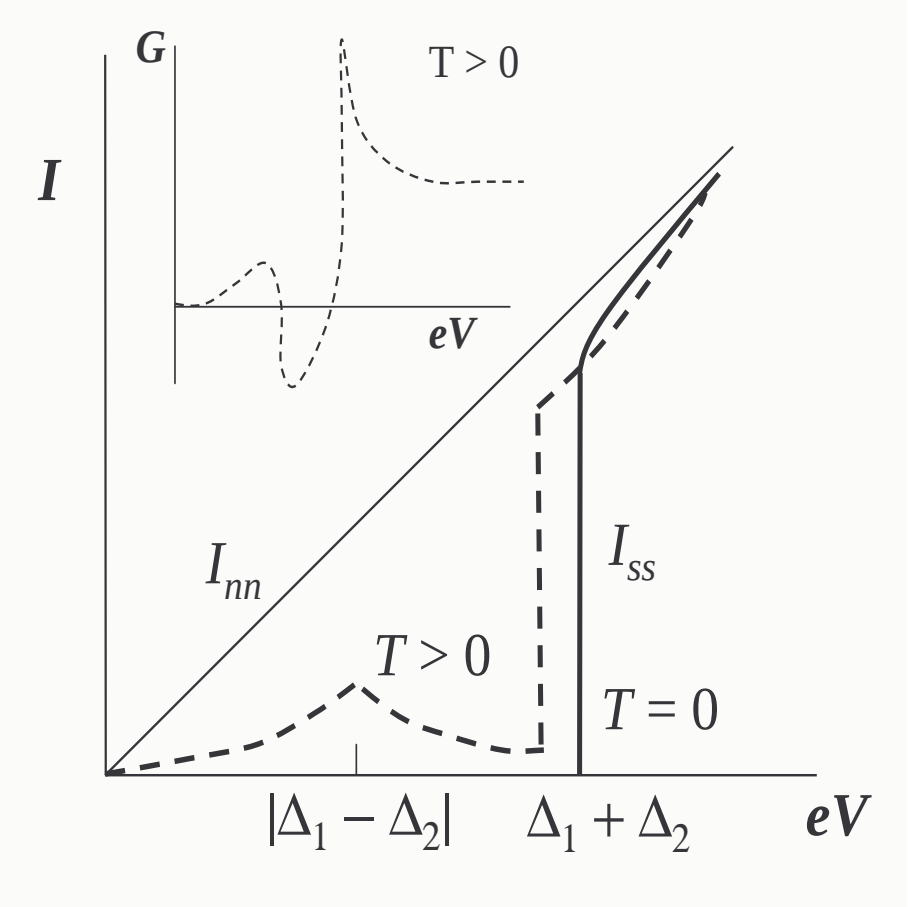

Figure 4.1: Expected $I - V$ spectrum of a tunnel junction between two s-wave superconductors. The solid line is for T=0 and the dashed line is for $T > 0$. The expected $G - V$ spectrum for $T > 0$ is shown in the inset.

tunneling spectra above its T_c value or by applying a field greater than its (upper) critical field.

The tunnel current in an SIS junction when both superconductors have s-wave symmetry is given by an energy integral over the density of states of the two superconductors [1]. At T=0, there is no current until the $eV = \Delta_1 + \Delta_2$. Since, the density of states is infinite at the gap edges, there is a discontinuous jump in the tunnel current at $eV = \Delta_1 + \Delta_2$ (see Fig. 4.1). This means that the differential conductance (G) is zero for $eV < \Delta_1 + \Delta_2$ and becomes infinite at $eV = \Delta_1 + \Delta_2$. For finite temperatures, thermally excited quasi-particles lead to curent flow at lower

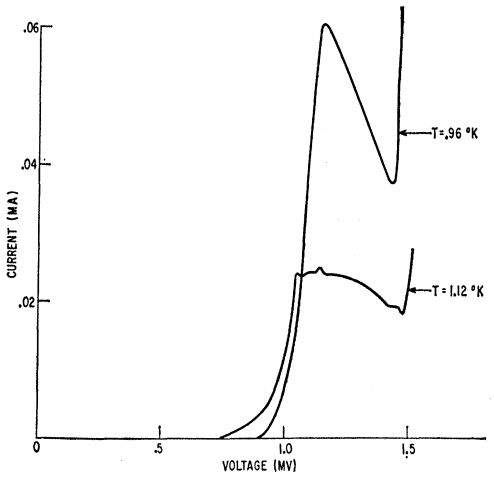

Figure 4.2: $I - V$ spectra of a tunnel junction between Al and Pb at different temperatures. Negative conductance region is observed because a voltage source was used to bias the junction. Figure taken from Ref. [101].

voltages. A peak in current occurs at $eV = |\Delta_1 - \Delta_2|$ because thermally excited quasiparticles in the peak of the density of states at Δ_1 can tunnel into the peaked density of states at Δ_2. For voltage biases between $|\Delta_1 - \Delta_2|$ and $\Delta_1 + \Delta_2$, the current decreases and there exists a negative differential conductance region. A sudden jump in current occurs at $eV = \Delta_1 + \Delta_2$ as for T=0 case (see Fig. 4.1).

The classic behavior of SIS junctions at finite temperatures has been observed in conventional superconductors by Giaever [37] (see Figs. 4.2 and 4.3). The negative G region cannot be observed by a current-source biasing arrangement because there are three possible values of V for a given I and the negative G region is unstable. The negative conductance region can only be observed when a voltage source is used for providing the bias. However, if a current source is used, there will be discontinuity in the $I - V$ and $G - V$ curves in the negative conductance region. Moreover, hysteresis will be observed in the $I - V$ data for increasing and decreasing currents [37].

When one superconductor has a fully gapped Fermi surface (FS) and the other

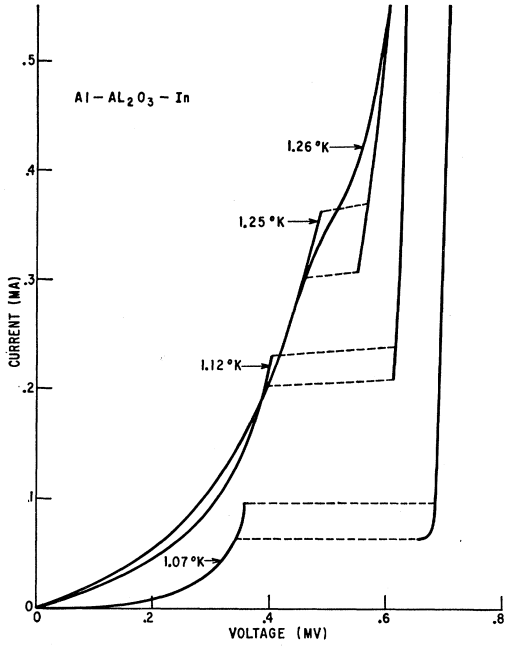

Figure 4.3: $I - V$ spectra of a tunnel junction between Al and In for different temperatures. Hysteresis occurs because a current source was used to bias the junction. Figure taken from Ref. [101].

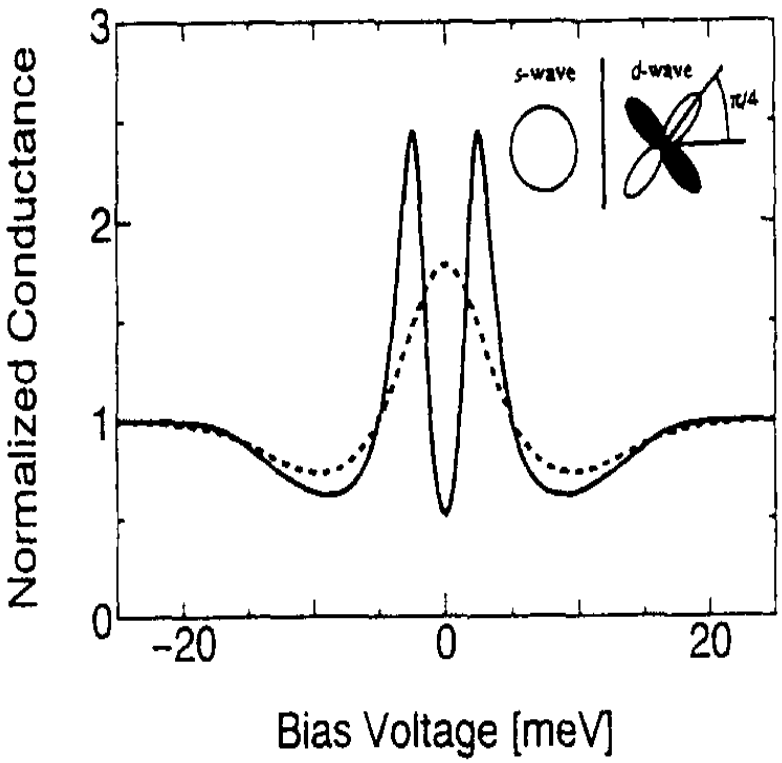

Figure 4.4: Calculated $G - V$ spectrum of a tunnel junction between an s-wave and $d_{x^2-y^2}$ superconductor with tunneling along [110] direction [102]. The solid and dashed lines are the theoretical spectra below T_c ($T = 4.2$ K) and above T_c ($T = 15$ K) of the s-wave superconductor.

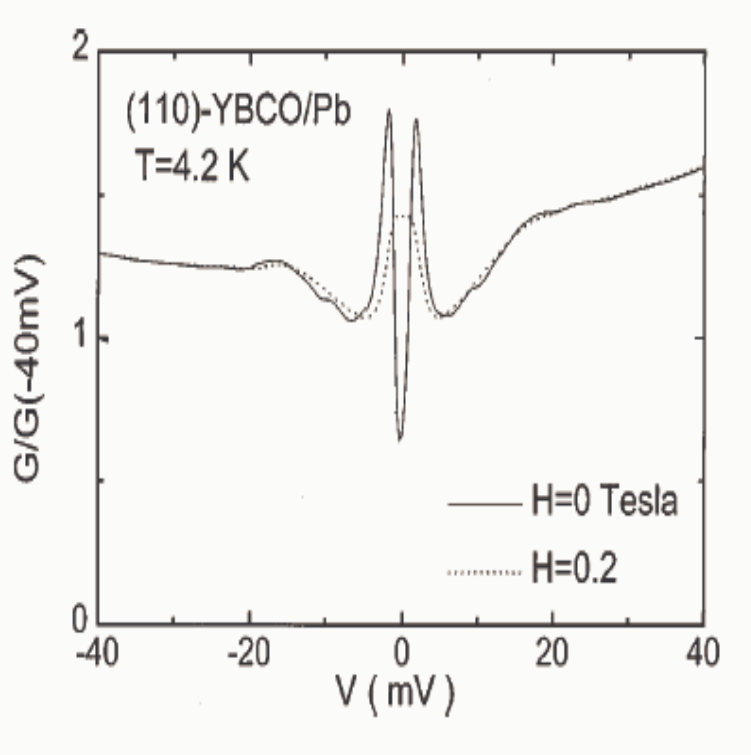

Figure 4.5: Measured $G - V$ spectrum of a tunnel junction between Pb and (110) oriented YBCO film. Taken from Ref. [81]

has d-wave pairing symmetry, then the characteristics of the tunnel current are totally different from the first case described above. These characteristics also depend upon the tunneling direction because of the very anisotropic nature of the d-wave gap. Here we consider the case where the normal to the junction interface is along the nodal direction of the d-wave superconductor i.e. one is tunneling into the (110) planes. It is assumed that the T_c and gap of the s-wave superconductor are much less than the T_c and maximum gap of the d-wave superconductor. The calculated differential conductance shows a peak at the gap edge of the s-wave superconductor because there are nodal quasi-particles in the d-wave superconductor that tunnel into the singular density of states at the gap edge of the s-wave superconductor [102](see Fig. 4.4). A gap-like feature is also observed at the maximum gap value of the d-wave superconductor.

Pb junctions on (110) oriented YBCO films show the features described in the preceding paragraph [81] (Fig. 4.5). Both the Pb and YBCO coherence peaks are seen at their respective gap edges when both electrodes are superconducting. This clearly implies the presence of nodal quasiparticles in YBCO. When Pb is driven normal by a magnetic field larger than its critical field, a ZBCP appears in the NIS tunneling spectrum and the gap-like features of YBCO remain almost unchanged. The ZBCP is a characteristic feature in tunneling spectra of d-wave superconductors. This behavior has also been observed when indium is used as the counter-electrode to form an SIS junction on YBCO [103].

Tunneling between an s-wave superconductor and the (100) face of a $d_{x^2-y^2}$ superconductor is expected to exhibit spectra similar to tunneling between two s-wave superconductors. This is because in this configuration, the maximum gap of the monotonic $d_{x^2-y^2}$ superconductor determines the shape of the spectra and the effect of nodal quasiparticles is reduced considerably.

4.2 Experimental Method

We want to tunnel into the ab-plane of the PCCO and NCCO crystals. The top surface of the crystal is covered with a layer of photo-resist to prevent c-axis contribution to the tunnel current. The crystal is cleaved to expose a fresh surface normal to the ab-plane and Pb is evaporated to form a junction (Fig. 4.6). The crystals are cleaved along random directions and therefore, the direction of the tunneling current with respect to the Cu-O bond direction is not known. Moreover, the junction interface is likely to be rough on the nano-scale, and the tunneling current will flow into facets of different orientations. This compromises the momentum resolution of tunneling. However, tunneling remains sensitive to the phase of the SC gap and to the presence or absence of nodes in the gap.

The $I-V$ characteristics are obtained with a four probe measurement. The $I-V$

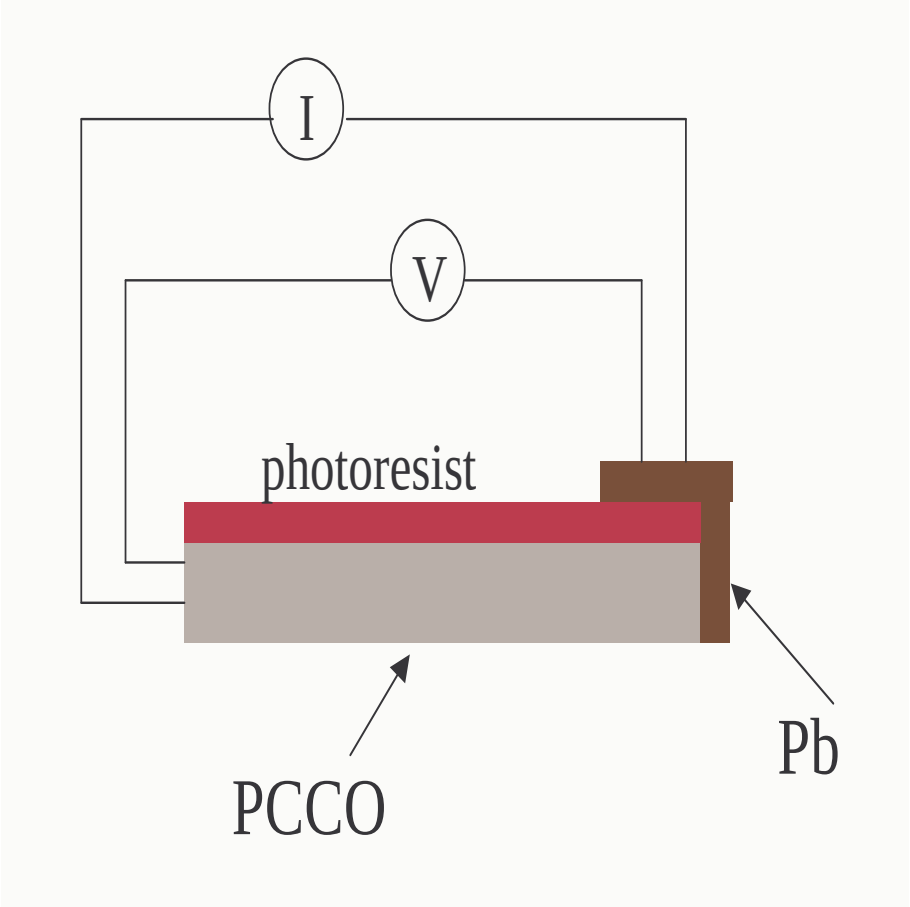

Figure 4.6: Method for high barrier tunneling on crystals of electron-doped cuprate superconductors.

spectra are numerically differentiated to obtain the $G-V$ spectra (G=dI/dV). A lock-in (derivative) technique is also used to obtain the the $G-V$ spectra directly and this method reduces noise in the spectra.

The crystal is cleaved in air before being transferred to the evaporation chamber for depositing Pb. This is because it has been shown that *ex situ* Pb junctions formed on c-axis oriented NCCO films are much better than *in situ* Pb junctions [100]. It has also been shown that Pb reacts with the oxygen in the NCCO to form a PbO_x barrier. *In situ* Pb evaporation causes Pb to react with oxygen at the regular sites leading to suppression of superconductivity in NCCO at the junction interface. When the NCCO film is exposed to air, oxygen is adsorbed on to the surface. When

Pb is now deposited, it reacts with this excess oxygen to form the oxide barrier. The NCCO surface remains superconducting because now oxygen deficiencies at the regular sites do not occur.

The yield of good junctions on optimally doped PCCO and NCCO crystals is about 20 percent. In the next section we present the first report of high quality tunnel junctions on PCCO/NCCO with the tunneling current exclusively along the *ab*-planes.

4.3 Results and Discussion

The $G - V$ spectra of tunnel junction on an optimally doped PCCO crystal ($T_c = 22 \pm 1$ K) are show in Fig. 4.7a,b and c. The spectrum for an SIS junction with both PCCO and Pb in the SC state is shown in panel (a). Pb goes normal when a magnetic field of 0.1 T is applied. The junction is now an NIS junction and its tunneling spectrum is shown in panel (b). A field of 12 T applied along the c-axis of PCCO drives it into the non-SC state and the resulting spectrum showing the NSG is given in panel (c). The spectra are obtained at $T = 1.8$ K.

The small conductance at zero bias indicates the high quality of the tunnel junction. The low zero bias conductance is due to the *s*-wave SC gap of Pb and low leakage current. The leakage current is estimated to be a few percent of the tunnel current. The weak feature near 9 meV in the SC state of Pb is due to a Pb phonon and this also points to a high quality tunnel junction. Two features are immediately noticeable in the SIS junction. There is a significant coherence peak at 5 meV and a "kink" at 1.9 meV. When Pb is driven normal, the kink disappears and the spectral weight around 5 meV is significantly reduced. The spectrum now shows only the SC features of PCCO with the coherence peaks at 4.3 meV and a zero bias conductance of about fifty-five percent of the normal state conductance.

The SIS spectrum does not display the classic features of SIS junctions made with

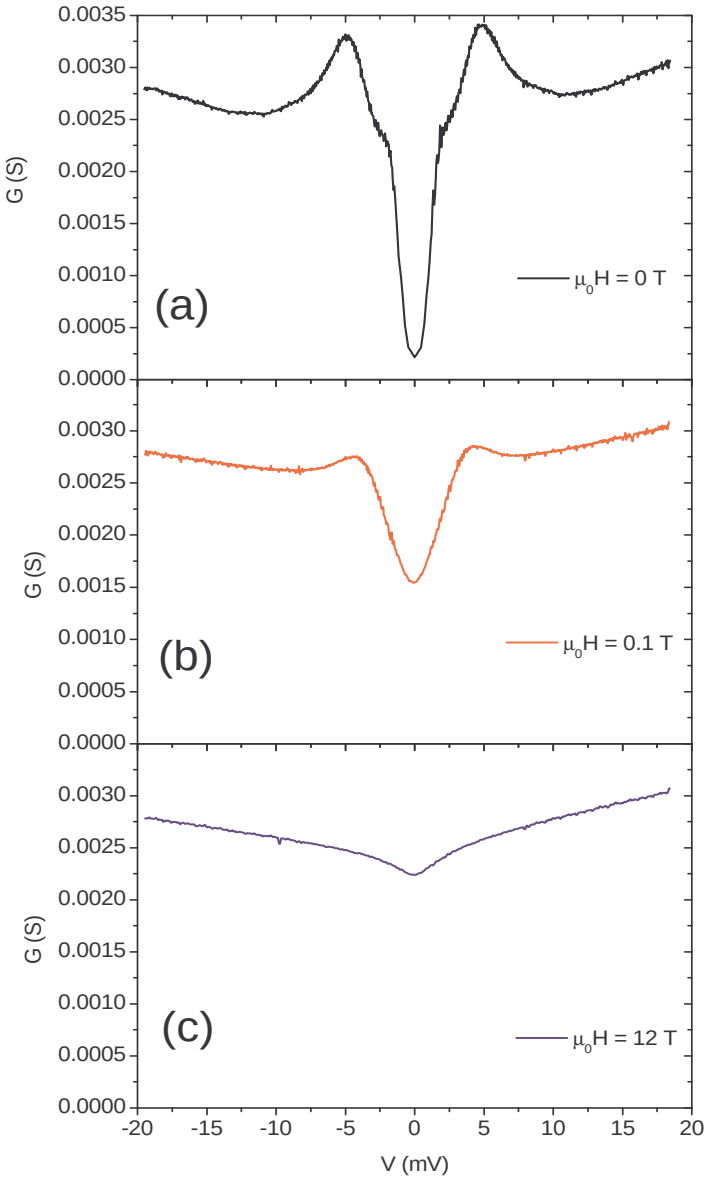

Figure 4.7: $G-V$ spectra of tunnel junction between Pb and PCCO (x=0.15) crystal at $T = 1.8$ K in (a) in zero magnetic field, (b) in 0.1 T (c) in 12 T. The magnetic field is perpendicular to the *ab*-plane. The tunneling current is along the *ab*-planes.

conventional superconductors. We know that Pb has an s-wave gap. If optimally-doped PCCO also had a fully gapped FS, discontinuity and hysteresis in the $I-V$ and $G-V$ spectra would have been observed for increasing and decreasing current bias. This is expected because of the unstable negative conductance region and the use of a current source. However, this behavior is not observed. Moreover, a pronounced peak should occur in the $G-V$ spectrum at $\Delta_{PCCO} + \Delta_{Pb}$. If Δ_{PCCO} is taken to be about 4.3 meV (from the position of the coherence peaks in panel (b)) and Δ_{Pb} is 1.4 meV, then the sum of the two gaps is 5.7 meV and this is larger than the observed peak position of 5 meV. One can argue that quasi-particle lifetimes are shorter in PCCO and this leads to broadening effects in the tunneling spectra. This broadening may cause $\Delta_{PCCO} + \Delta_{Pb}$ peak to occur at a different position than expected for classical s-wave superconductors. Moreover, quasi-particle lifetime broadening could also wash out the negative conductance region. Indeed the kink at 1.9 meV may be a Δ_{PCCO} - Δ_{Pb} feature. However, in theory, this kink should occur at 2.9 meV in the absence of quasi-particle lifetime broadening effects.

The Pb/PCCO spectrum does not resemble the spectrum for Pb/YBCO junction either (compare with Fig. 4.5). In the Pb/YBCO junction, there is a sharp coherence peak at Δ_{Pb} (due to nodal quasiparticles in YBCO) and a weaker coherence peak at Δ_{YBCO}. There is no significant additional spectral weight near Δ_{YBCO}. When superconductivity of Pb is quenched by a small magnetic field, the Pb coherence peaks disappear and there is little change in the YBCO coherence peaks. Moreover, a ZBCP appears in the spectrum and this is a decisive signature of d-wave superconductivity in YBCO. In Pb/PCCO junction, there is no sharp Pb coherence peak. If the kink at 1.9 meV is taken to be due to Pb alone, then this means that there is only a limited density of nodal quasi-particles in PCCO. The enormous shift of spectral weight of the Pb coherence peak to above the PCCO coherence peak position means that there is significant contribution to the conductance from the gapped regions of the FS in PCCO. One can attempt to explain

the tunneling data by invoking a non-monotonic d-wave gap first proposed to explain the Raman data on optimally doped NCCO [19]. The non-monotonic d-wave gap will be discussed in detail in Chapter 6. Here we briefly describe its basic features. The non-monotonic d-wave gap has nodes in the (0,0)$\rightarrow(\pi,\pi)$ direction like the monotonic $d_{x^2-y^2}$ gap. However, the non-monotonic d-wave gap is maximum near the nodal directions and not in the $(\pi,0)$ direction like a $d_{x^2-y^2}$ gap. This leads to a restricted nodal phase space and could explain the limited density of nodal quasi-particles in PCCO. Moreover, for this type of gap, the tunneling has to be predominantly in the (110) direction to emphasize the nodal character. If the junction interface is not in the (110) direction and/or is faceted, then the tunneling current will be dominated by contributions from the gapped regions and will lead to the SC spectral weight of Pb to be mostly shifted to above the PCCO gap. The absence of a ZBCP in the tunneling spectrum of PCCO could also be due to this restricted nodal phase space in PCCO. The absence of the ZBCP can also be attributed to the larger quasiparticle scattering rate in PCCO (compared to YBCO) that could prevent the formation of the ZBCP. Even though there is no ZBCP, the significant zero bias conductance in the junction on optimally-doped PCCO means that there are quasi-particle states in the gap. We have considered the possibility that the kink at 1.9 meV may be due to some normal regions on the PCCO side of the junction interface. However, this is unlikely because in junctions where the SC features of PCCO are weaker, there is no significant increase in the Pb coherence peak near the Pb gap value (see Fig. 4.10).

The magnetic field and temperature dependence of a Pb/PCCO(x=0.15) crystal junction is shown in Fig. 4.8a and b. A field of 6 T completely suppresses the coherence peaks. There is a small change in zero bias conductance between 6 and 8 T. There is essentially no difference in the spectra between 8 and 12 T. Therefore, H_{c2} is at least 6 T for optimally doped PCCO. From the temperature dependence of the spectra one can estimate the T_c of the junction to be between 18 and 22 K.

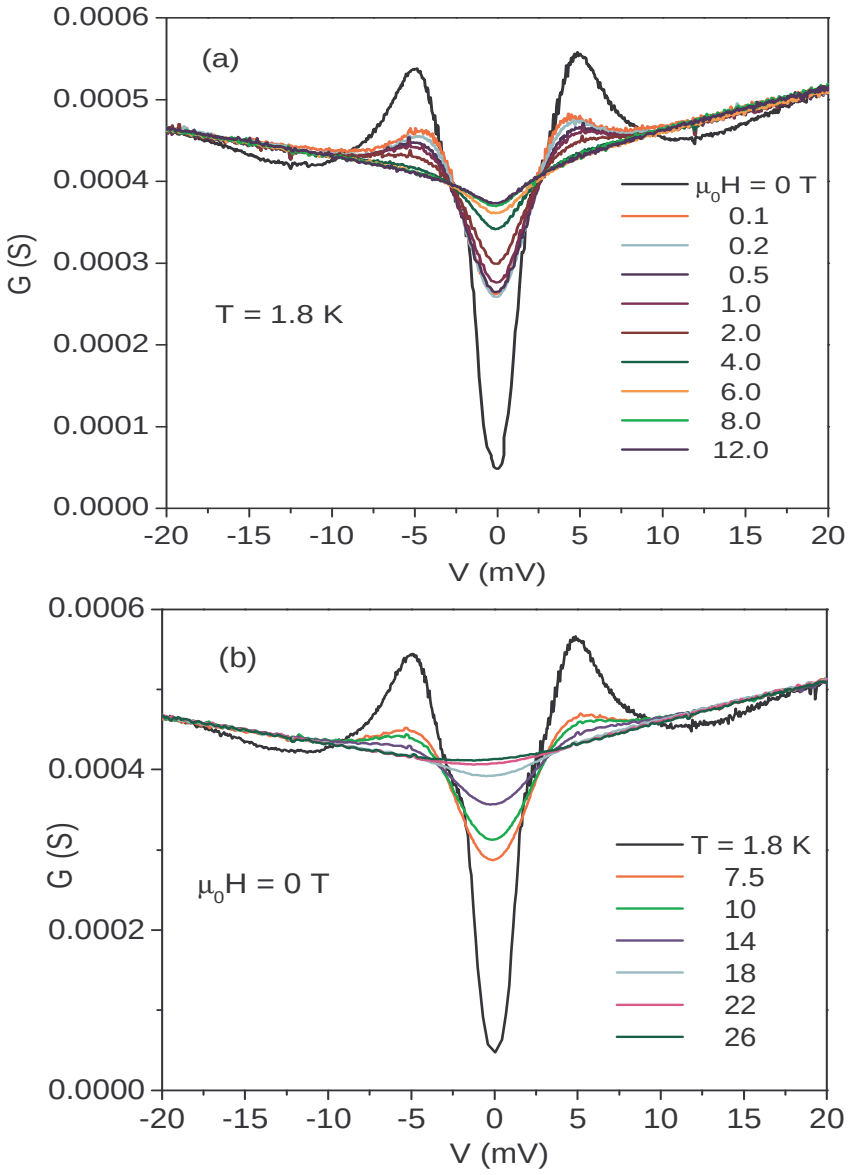

Figure 4.8: Magnetic field (panel a) and temperature (panel b) dependence of $G-V$ spectra of a tunnel junction between Pb and PCCO (x=0.15) crystal.

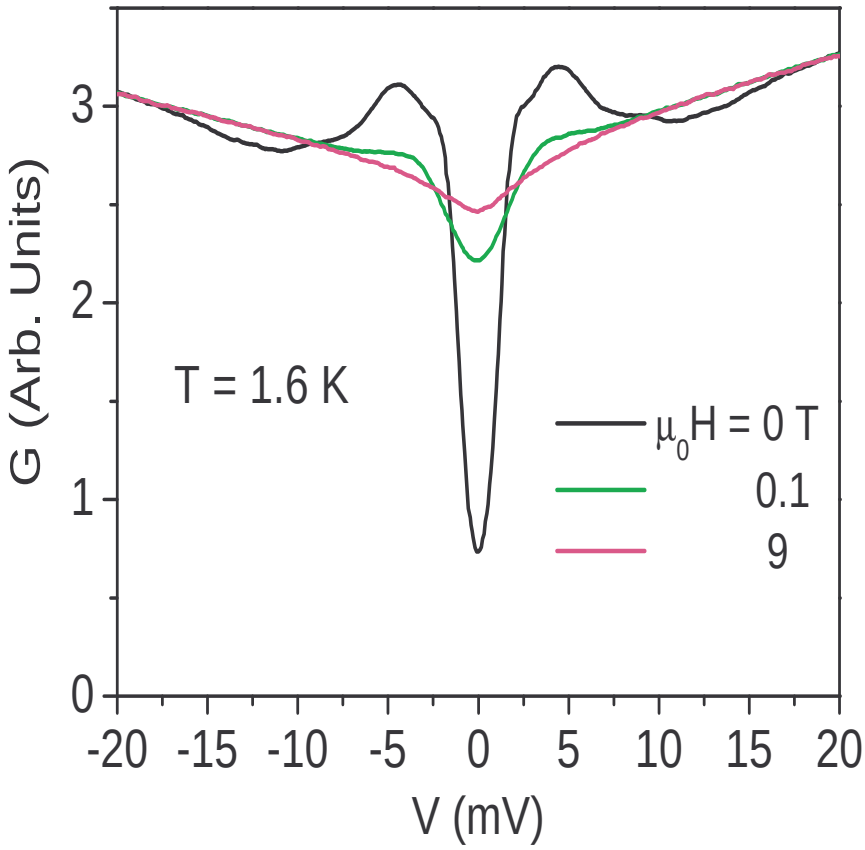

Figure 4.9: $G - V$ spectra of a tunnel junction between Pb and optimally doped NCCO crystal.

This is in good agreement with the bulk T_c of the crystal which is 22 K.

The tunneling spectra of a Pb/NCCO junction is shown in Fig. 4.9. The NCCO crystal is close to optimum doping with a T_c of 21 K. This junction has a higher leakage current compared to the best Pb/PCCO junctions. However, the features in the SIS and NIS junctions are similar to those in Pb/PCCO junctions. The kink in the SIS junction occurs at 2 meV and the coherence peak is positioned at 4.5 meV. This peak loses intensity when Pb is driven normal suggesting that its spectral weight comes from the high density of states at the Pb gap edge coupled with the density of states at the NCCO gap edge.

Several unsuccessful attempts were made to obtain a high quality tunnel junction

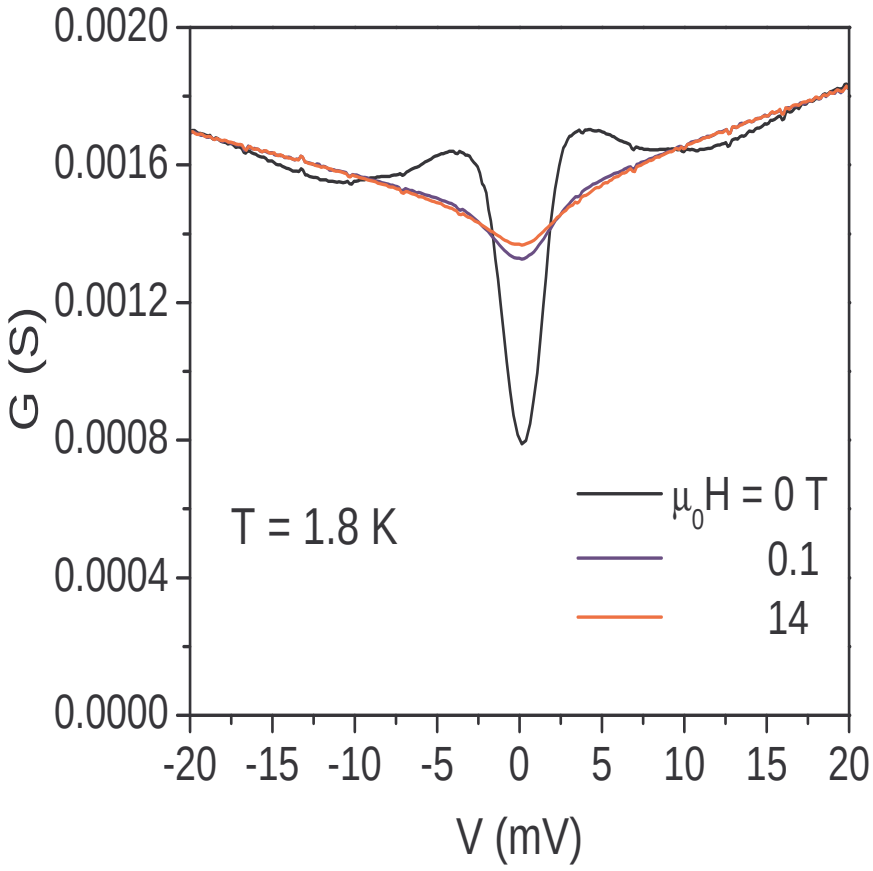

Figure 4.10: $G - V$ spectra of a tunnel junction between Pb and an over-doped PCCO crystal (x $\approx$ 0.17, $T_c \approx$ 13 K).

on over-doped PCCO crystals. The best junction obtained so far has a fairly high zero bias conductance suggesting a significant leakage current (see Fig. 4.10). There is no feature around 2 meV. There is a pronounced peak at 3.9 meV which gets suppressed when Pb is driven normal by a magnetic field of 0.1 T. The SC features of PCCO are extremely weak. One requires a better tunnel junction on an over-doped PCCO crystal which shows clear SC signatures of PCCO before one can make a definite statement about the gap symmetry in the over-doped regime.

In all point contact and tunnel junctions, one sees a partial suppression of conductance near zero bias when PCCO/NCCO is driven normal by a magnetic field. This is the normal state gap (NSG). The temperature dependence of the normal

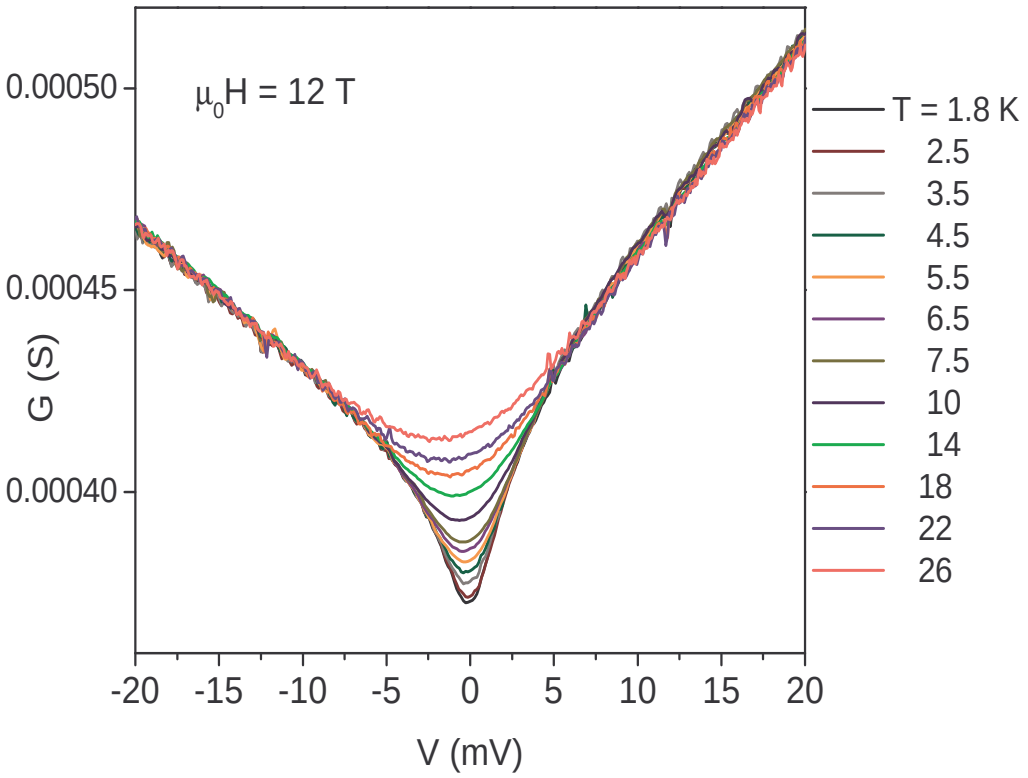

Figure 4.11: Temperature dependence of the normal state gap in the tunneling spectrum of a Pb/PCCO(x=0.15) crystal.

state gap is shown in Fig. 4.11. A previous report claimed that the NSG disappears suddenly at a particular temperature less than T_c of the PCCO film [88]. We see a "smooth" rather than a "sudden" disappearance of the NSG. Moreover, to obtain the temperature dependence of the NSG one has to take into account the effect of thermal smearing.

The tunneling spectra in the non-SC state of optimally-doped PCCO crystal obtained at 1.8 K and 26 K are shown in Fig. 4.12. The spectrum at 1.8 K shows the NSG. This data is taken and thermally smeared with the Fermi function at a temperature of 26 K (see, for example, Ref. [87] for details). The thermally smeared data is shown as red circles in Fig. 4.12. The thermally smeared data still shows a weak gap compared to the actual data at 26 K that shows no gap at all. Clearly,

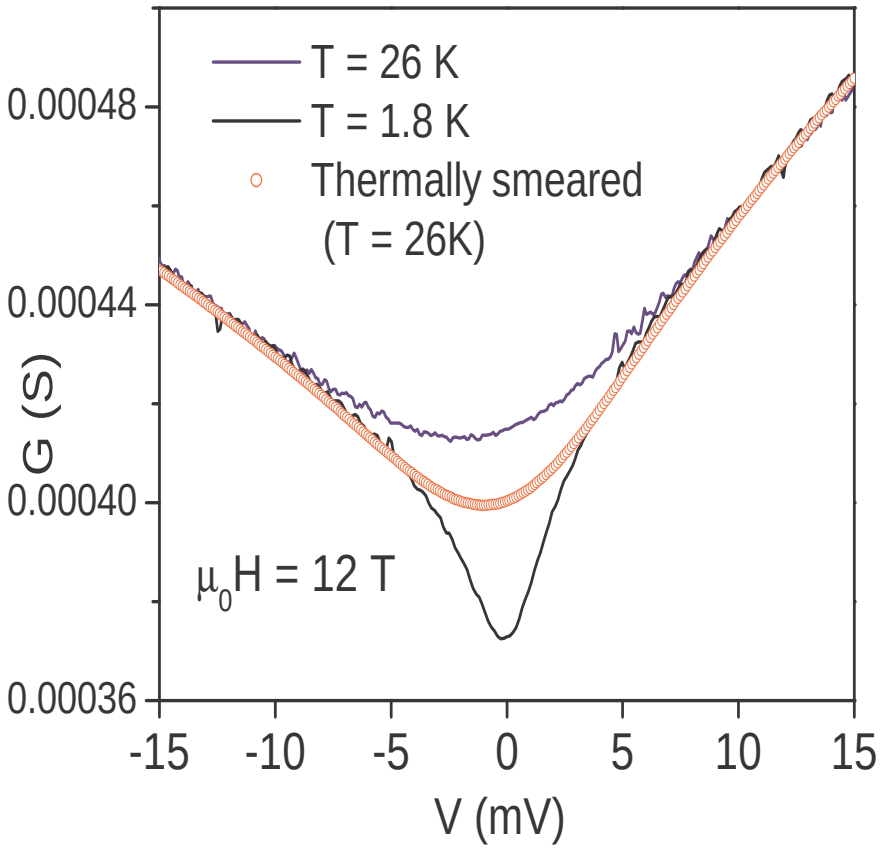

Figure 4.12: Effect of thermal smearing on the normal state gap.

the NSG has a temperature dependence of its own and our analysis shows that the NSG vanishes at a temperature below 26 K.

The NSG has been called the "pseudogap" in analogy with the pseudogap observed in the hole-doped HTSC [88]. The origin of the pseudogap in the hole-doped HTSC is not yet known. The origin of the NSG in the electron-doped cuprates is also a mystery. However, we can put forward possible explanations. One explanation of the NSG is that it arises from electron-electron Coulomb interactions [87]. Another physically profound possibility is that the NSG could be due to antiferromagnetism, similar to the weak partial gap observed in the tunneling spectra of antiferromagnetic chromium [35]. An interesting explanation could be that the NSG is due to a charge density wave, similar to the charge density wave gap observed

in the tunneling spectra of $NbSe_2$ [36]. Or the NSG could be due something more mundane, for example, non-equilibrium effects that lead to partial blockade of states near the Fermi energy when the occupation function at the injection energy exceeds the equilibrium Fermi function value. This blockade occurs if the tunneling rate is higher than the quasi-particle relaxation rate [104, 105].

The energy scale of the NSG is of the order of 5 meV. If the NSG is due to a suppression of the density of states, it should be observable in other experiments. So far this low energy NSG has not been reported in any other type of experiment. One reason could be that the NSG is a rather weak effect. Secondly, the NSG appears to coexist with the SC gap and disappears at or below T_c as reported in Ref. [88]. Preliminary analysis of our tunneling data at the lowest temperature (T = 1.8 K) shows that quasiparticle states are conserved in the SC phase only if the NSG coexists with the SC gap.

4.4 Summary

We report the first high quality tunnel junctions prepared on single crystals of the electron-doped cuprates with the tunneling current along the *ab*-planes. The tunneling data on optimally doped crystals is inconsistent both with a clean *s*-wave gap and with a simple monotonic $d_{x^2-y^2}$ gap. The data can be explained by a non-monotonic *d*-wave gap with limited phase space around the nodes. This form of the gap may be responsible for the low density of nodal quasiparticles as well as the absence of the ZBCP due to Andreev bound states. Tunnel junctions on over-doped crystals have not yet reached the same high quality that we have obtained on optimally-doped crystals. Therefore, we cannot at present make a definitive statement about the gap symmetry in over-doped samples with this experimental technique.

The normal state gap is observed in the tunneling spectra once the samples

are driven normal by $H > H_{c2}$. Analysis of the variation with temperature of the NSG shows that it has a temperature dependence of its own and that it vanishes at or below T_c of the optimally doped sample. The smooth evolution of the normal state tunneling spectra with temperature does not support the notion of "sudden" disappearance of the NSG as reported in Ref. [88]. Preliminary analysis of the data in the SC state shows that the NSG appears to coexist with the SC gap.

Chapter 5

Electronic Raman Spectroscopy

This chapter is devoted to Electronic Raman Spectroscopy (ERS) measurements on single crystals and films of PCCO and NCCO with various cerium dopings covering the entire superconducting phase diagram of these cuprates. The superconducting state was probed with Raman scattering and the evolution of the pair-breaking 2Δ peak was studied as a function of light polarization, temperature and magnetic field. This chapter begins with an introduction to Raman scattering followed by a review of the theory underlying ERS, experimental method and Raman measurements on conventional superconductors and hole-doped cuprates.

5.1 Introduction

The discovery of inelastic scattering of light from elementary excitations was made in 1928 by C. V. Raman and, about the same time, by Mandelstam and Landsberg [41]. Inelastic scattering of light means that the scattered photon has a different frequency from the incident photon. This phenomenon is referred to as the Raman effect. It was clear soon after its discovery that a new field of research had been opened up. Subsequently, the Raman effect was used extensively to study various elementary excitations including phonons, magnons, quasiparticles and plasmons in condensed media. A new impetus was given to research in Raman scattering by the devel-

opment, in the 1960s, of laser sources that provided intense monochromatic light. This made possible the observation of inelastic scattering from processes with much smaller cross-sections [41].

Soon after the publication of the BCS theory, Abrikosov and Fal'kovskii [106, 107], in 1961, theorized that the signature of superconductivity should manifest itself in Raman scattering through the opening of a gap for frequencies $\omega < 2\Delta$. However,the cross section of the inelastic scattering of light from electronic excitations out of the Cooper pair condensate was predicted to be extremely weak. Therefore, even after the availability of laser sources, attempts in the 1960s and 1970s to observe this effect were unsuccessful. Moreover, excellent rejection of the elastically scattered light was required to reveal the small gap of conventional superconductors. This was beyond the capability of the equipment available at the time. After concerted efforts by experimentalists to improve rejection of elastically scattered (stray) light in their optical equipment and the availability of better quality samples, the first observation of excitations out of the SC state in the form of Raman active gap modes was made in $NbSe_2$ [44]. Subsequently 2Δ coherence peaks were observed in Nb_3Sn and V_3Si [45, 46].

In type I superconductors, the optical penetration depth is a few hundred ångstrom while the coherence length is about an order of magnitude larger. Therefore, in such materials, Raman spectroscopy probes only a few hundred ångstrom and is essentially a surface probe. In conventional type II superconductors e.g. Nb_3Sn, the optical penetration depth is almost as large as the coherence length and ERS is said to be a bulk probe in this case. In HTSC, the coherence lengths are typically few tens of angstroms and the optical penetration depths are about two orders of magnitude larger. Therefore, in HTSC, ERS certainly probes the bulk of the samples and is a method of choice compared to ARPES and Tunneling Spectroscopy. The instrumental energy resolution of ERS is better than 0.2 meV (≈ 1.5 cm^{-1}). However, as in all spectroscopies, the resolution of structures in the spectra is limited by

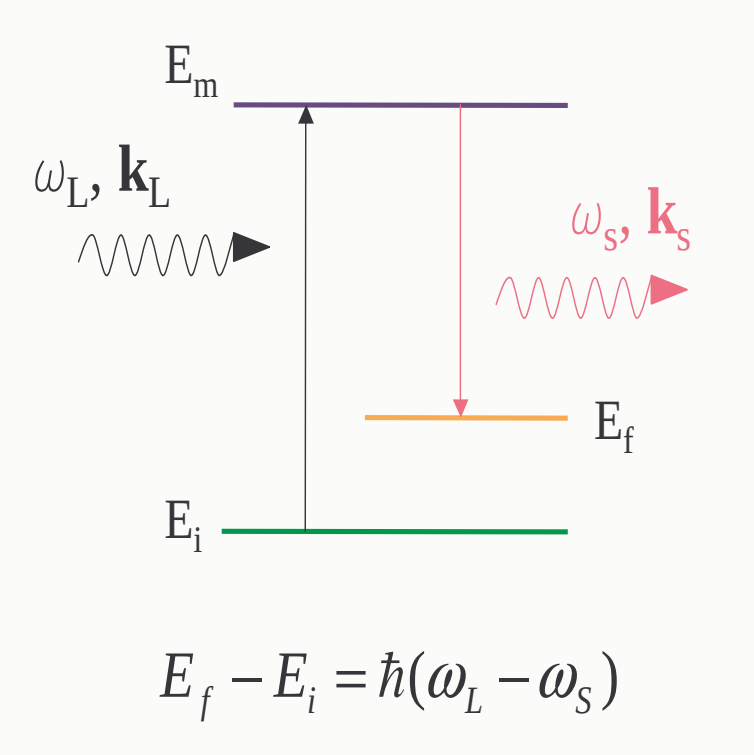

Figure 5.1: Raman scattering via intermediate state

thermal smearing and quasi-particle lifetime broadening and depends on the temperature of the sample (≈ 0.5 meV at $T = 4$ K) and the quasi-particle scattering rate. By using polarized light, the momentum dependence of the superconducting gap can also be studied. ERS is indeed an attractive technique for investigating the superconducting state in HTSC materials.

5.2 Theory

This section is based on several ERS papers and articles cited in chronological order [108, 43, 109, 110, 111, 112, 113, 114].

The Hamiltonian for the interaction of light with a particle of charge e is

$$H = \frac{1}{2m}[\mathbf{p} - \frac{e}{c}\mathbf{A}(\mathbf{r},t)]^2 + e\varphi(\mathbf{r},t) + V(\mathbf{r}) \tag{5.1}$$

There are no sources ($\varphi = 0$) and using the transverse (Coulomb) gauge $\nabla.\mathbf{A} = 0$,

the Hamiltonian becomes

$$H = \frac{\mathbf{p}^2}{2m} + V(\mathbf{r}) - \frac{e}{mc}\mathbf{p}.\mathbf{A}(\mathbf{r},t) + \frac{e^2}{2mc^2}\mathbf{A}^2(\mathbf{r},t) \tag{5.2}$$

The first two terms are the unperturbed Hamiltonian. The next two terms give the interaction between light and the charged particle and can be treated as a perturbation. The $\mathbf{p}.\mathbf{A}$ term in first order perturbation theory gives rise to electric dipole transitions (optical absorption, stimulated and spontaneous emission). The same term evaluated in second order perturbation theory along with the term quadratic in the vector potential evaluated in first order perturbation theory lead to Rayleigh and Raman scattering. In Rayleigh (elastic) scattering, the incident and scattered photons have the same energy. In Raman (inelastic) scattering the scattered photons have a different energy (frequency) from the incident photons. Consequently, the charged particle goes into a state whose energy differs from its initial state by the same value as the difference between the energies of the incident and scattered photons (see Fig. 5.1 for scattering via intermediate states). Of course, in this process, both energy and momentum are conserved. The $\mathbf{p}.\mathbf{A}$ term leads to scattering via intermediate states. These could be virtual states or real states given by the band structure. In the latter case, the scattering is resonantly enhanced. Here we will deal with the theory of Raman scattering from electronic excitations.

In a simple metal in the vicinity of the Fermi energy, an electron-hole excitation is created in the course of the scattering process. If only intraband transitions are considered, the energy interval of interest is given by , $\Delta E = qv_F$, where q is the magnitude of momentum transferred to the electron and v_F is the Fermi velocity. For visible light, $q \approx 0.002$ $\mathring{A}^{-1}$. In a metal $v_F \approx 2$ eV $\mathring{A}^{-1}$. This gives $\Delta E \approx 4$ meV, i.e., the electronic scattering is confined to a narrow energy range. This is due to the small momentum transfer that the photon of visible light can provide and this restricts excitations to close vicinity of the Brillouin zone center (Brillouin zone dimensions are of the order of inverse angstroms). The high-T_c cuprates, however,

posses a broad incoherent background and the electronic scattering extends over an energy range in the order of eV. This has been described phenomenologically by the Marginal Fermi Liquid (MFL) model [115].

First consider in some detail the scattering from a single electron before generalizing to an arbitrary number of electrons. The electron is in a Bloch eigenstate $|\mathrm{n}_i,\mathbf{k}_i\rangle$ with band index n_i, momentum $\mathbf{k}_i$ and energy $\mathrm{E}_{n_i,\mathbf{k}_i}$. The electromagnetic fields are denoted by vector potentials $\mathbf{A}_L$ and $\mathbf{A}_S$ of the incident laser and scattered light respectively.

$$\mathbf{A}_L = A_L^0 \mathbf{e}_L a_{\mathbf{k}_L} e^{i(\mathbf{k}_L.\mathbf{r}-\omega_L t)} + \texttt{hermitian conjugate} \tag{5.3}$$

$$\mathbf{A}_S = A_S^0 \mathbf{e}_S a_{\mathbf{k}_S} e^{i(\mathbf{k}_S.\mathbf{r}-\omega_S t)} + \texttt{hermitian conjugate} \tag{5.4}$$

Here $a_{\mathbf{k}_{L,S}}$ are annihilation operators of the laser and scattered photons. First let us apply first order perturbation theory in the form of Fermi's Golden Rule to the term in the Hamiltonian quadratic in the vector potential. Fermi's Golden Rule for transition amplitude is

$$T_{if} = \frac{2\pi}{\hbar}\delta(E_f - E_i)\langle f|H'|i\rangle \tag{5.5}$$

and this gives the transition amplitude without intermediate virtual states.

$$T_1 = \frac{2\pi e^2}{\hbar m c^2}\mathbf{e}_S.\mathbf{e}_L\langle A_S A_L\rangle \delta_{n_f,n_i}\delta_{\mathbf{k}_f,\mathbf{k}_i+\mathbf{q}}\delta(E_{n_f,\mathbf{k}_f} - E_{n_i,\mathbf{k}_i} - \hbar\omega) \tag{5.6}$$

The difference in the photon frequencies is $\omega = \omega_L$ - ω_S and the difference in photon momenta is $\mathbf{q} = \mathbf{k}_L$ - $\mathbf{k}_S$. The matrix elements of the photon states are denoted by $\langle\ \ \rangle$. The conservation of energy and momentum is embedded in the delta functions.

The second order amplitude involving the $\mathbf{p}.\mathbf{A}$ term requires a summation over all possible intermediate states and is composed of two terms: one term comes from the annihilation of the incident photon and creation of a scattered photon and the second term from the process in reverse order. For simplicity, the second process

is denoted by (L$\longleftrightarrow$S) because it is obtained by substitution of $\omega_L \longleftrightarrow$ -ω_S and $\mathbf{k}_L \longleftrightarrow$ -$\mathbf{k}_S$. Momentum conservation contracts the sum over intermediate electron momenta and one obtains

$$T_2 = \frac{2\pi e^2}{\hbar m^2 c^2}\langle A_S A_L\rangle \delta_{\mathbf{k}_f,\mathbf{k}_i+\mathbf{q}}\delta(E_{n_f,\mathbf{k}_f} - E_{n_i,\mathbf{k}_i} - \hbar\omega)\sum_{n_m}\Gamma_{fmi}(\mathbf{q},\mathbf{k}) \tag{5.7}$$

with matrix elements

$$\Gamma_{fmi}(\mathbf{q},\mathbf{k}) = \frac{\langle n_f, \mathbf{k}_i+\mathbf{q}|e^{-i(\mathbf{k}_S.\mathbf{r}-\omega_S t)}\mathbf{e}_S.\mathbf{p}|n_m,\mathbf{k}_i+\mathbf{k}_L\rangle\langle n_m,\mathbf{k}_i+\mathbf{k}_L|e^{i(\mathbf{k}_L.\mathbf{r}-\omega_L t)}\mathbf{e}_L.\mathbf{p}|n_i,\mathbf{k}_i\rangle}{E_{n_i,\mathbf{k}_i} - E_{n_m,\mathbf{k}_i+\mathbf{k}_L} + \omega_L + i\eta} + (L \longleftrightarrow S) \tag{5.8}$$

When the above is generalized to many electrons, the exact initial and final many-electron states are not known. Thus Eq. 5.6 and Eq. 5.7, modified for many-electron states, are impossible to evaluate exactly. However, these equations can be considered as arising from an effective perturbative Hamiltonian of the form

$$H_R = \frac{e^2}{mc^2}\langle A_S A_L\rangle e^{-i\omega t}\hat{\rho}_{\mathbf{q}} \tag{5.9}$$

where the dimensionless effective density perturbation operator is

$$\hat{\rho}_{\mathbf{q}} = \sum_{n_f,n_i,\mathbf{k}} \gamma_{n_f,n_i,\mathbf{k}} {c^\dagger}_{n_f,\mathbf{k}+\mathbf{q}} c_{n_i,\mathbf{k}} \tag{5.10}$$

The annihilation and creation operators for electrons are $c_{n_i,\mathbf{k}}$ and ${c^\dagger}_{n_f,\mathbf{k}+\mathbf{q}}$ respectively. The transition matrix element is also known as the Raman vertex or Raman form factor:

$$\gamma_{n_f,n_i,\mathbf{k}} = \mathbf{e}_S.\mathbf{e}_L\delta_{n_f,n_i} + \frac{1}{m}\sum_{n_m}\Gamma_{fmi}(\mathbf{k}) \tag{5.11}$$

The photon differential scattering cross section can now be calculated by applying Fermi's Golden Rule to the effective perturbation Hamiltonian.

$$\frac{d^2\sigma}{d\Omega d\omega} = r_0^2\frac{\omega_S}{\omega_L}S(\mathbf{q},\omega,\beta) \tag{5.12}$$

where $r_0 = e^2/mc^2$ is the classical radius of the electron and the generalized dynamical structure factor

$$S(\mathbf{q},\omega,\beta) = \sum_{i,f} \frac{1}{Z} e^{-\beta E_i} |\langle f|\hat{\rho}_{\mathbf{q}}|i\rangle|^2 \delta(E_f - E_i - \omega) \tag{5.13}$$

Here, $e^{-\beta E_i}/Z$ is the probability of the initial state in thermodynamic equilibrium. The states $|i\rangle$ and $|f\rangle$ are now exact many-body states. The structure factor is an equilibrium property of the electron system in the absence of the perturbation and can be interpreted as the power spectrum of the charge density fluctuations at angular frequency ω. However, it is not possible to calculate the structure factor using the above equation because the initial and final many-electron states are still not known.

One can now use an important result from statistical mechanics, the Fluctuation-Dissipation theorem, that relates the power spectrum of the charge density fluctuations to the imaginary part of a density-density response function:

$$S_{\gamma\gamma}(\mathbf{q},\omega) = -\frac{1}{\pi}[1 + n(\omega)]\mathrm{Im}\chi_{\gamma\gamma}(\mathbf{q},\omega) \tag{5.14}$$

The density-density response function is often referred to as the Raman response function or Raman susceptibility $\chi_{\gamma\gamma}(\mathbf{q},\omega)$. $n(\omega)$ is the Bose-Einstein distribution function. The subscripts γ denote the dependence of the Raman response function on the Raman vertex.

From BCS theory, the imaginary part of the Raman response function (Imχ or χ") in the SC state at zero temperature is given by

$$\mathrm{Im}\chi(\omega,\mathbf{q}) = \int \frac{d^3k}{(2\pi)^3} \gamma(\mathbf{k})^2 \frac{EE' - \epsilon(\mathbf{k})\epsilon(\mathbf{k})' + \Delta(\mathbf{k})^2}{2EE'} \delta(\omega - E - E') \tag{5.15}$$

In the above equation, $E(\mathbf{k}) = \sqrt{\epsilon(\mathbf{k})^2 + \Delta(\mathbf{k})^2}$ is the quasiparticle energy, $\epsilon(\mathbf{k})$ is the band dispersion relative to the Fermi energy and $\Delta(\mathbf{k})$ is the superconducting order parameter. Also, $\epsilon(\mathbf{k})' = \epsilon(\mathbf{k}+\mathbf{q})$. The factor $[EE' - \epsilon(\mathbf{k})\epsilon(\mathbf{k}') + \Delta(\mathbf{k})^2]/2EE'$ is the BCS coherence factor for a pair-breaking type-I perturbation.

The Raman response function due to the breaking of Cooper pairs in a superconductor and including Coulomb screening can also be written as:

$$\mathrm{Im}\chi_{\gamma\gamma}(\mathbf{q},\omega) = \langle\gamma_{\mathbf{k}}^2\lambda_{\mathbf{k}}\rangle - \frac{\langle\gamma_{\mathbf{k}}\lambda_{\mathbf{k}}\rangle^2}{\langle\lambda_{\mathbf{k}}\rangle} \tag{5.16}$$

In this equation, the Raman vertex $\gamma_{\mathbf{k}}$ depends on the scattering geometry and describes the strength of interaction of the photons with the quasiparticle excitations, $\lambda_{\mathbf{k}}$ is the Tsuneto function defined below, and the angular brackets denote momentum sums over the Fermi surface.

$$\lambda(\mathbf{k},\omega,T) = \frac{\Delta(\mathbf{k})^2}{E(\mathbf{k})^2}\tanh[\frac{E(\mathbf{k})}{2k_BT}][\pm\delta(2E(\mathbf{k})\mp\omega)] \tag{5.17}$$

The first term of Eq. 5.16 is the unscreened Raman response and is a simplification of Eq. 5.15 for negligible momentum transfer i.e. $\mathbf{q}\rightarrow 0$. It can be seen that the Raman response depends upon the square of the superconducting order parameter and therefore Raman scattering is not sensitive to the sign of the order parameter.

If one assumes small momentum transfer and incident light energies smaller than the optical band gap (nonresonant scattering), the Raman vertex can be written in terms of the curvature of the energy band dispersion (also referred to as the inverse effective mass tensor or Raman tensor):

$$\gamma(\mathbf{k}) = m\sum_{\alpha,\beta} e_\alpha^S \frac{\partial^2\epsilon(\mathbf{k})}{\partial k_\alpha \partial k_\beta} e_\beta^L \tag{5.18}$$

Here e^L and e^S are the respective polarization vectors of the incident laser and scattered photons and α and β are summation indices which correspond to different projections of the momentum $\mathbf{k}$. The light polarization vectors select elements of the Raman tensor.

The dispersion relation for the one-layer cuprates in the tight-binding approximation is given by

$$\epsilon(\mathbf{k}) = -2t[\cos(k_xa)+\cos(k_ya)] + 4t'\cos(k_xa)\cos(k_ya) - \mu \tag{5.19}$$

where t and t' are the nearest-neighbor and next-nearest -neighbor hopping parameters respectively, a is the in-plane lattice constant of the tetragonal unit cell and μ is the chemical potential. The inverse effective mass tensor can be derived from the dispersion relation and the Raman vertices are related to different elements of the tensor. For example, for crossed polarization vectors, the following relations between polarization and **k**-space are found

$$\gamma_{xy} \propto 4t' \sin(k_x a) \sin(k_y a) \tag{5.20}$$

$$\gamma_{x'y'} \propto t(\cos(k_x a) - \cos(k_y a)) \tag{5.21}$$

with x=[100], y=[010], x'=[110] and y'=[$\bar{1}$10]. The Cu-O bonds are along the [100] and [010] directions.

The symmetry of the underlying crystal can be taken into account by expanding the Raman vertex in terms of a complete set of crystal harmonics Φ_L defined on the Fermi surface:

$$\gamma(\mathbf{k}) = \sum_{L,\mu} \gamma_L^\mu \Phi_L^\mu(\mathbf{k}) \tag{5.22}$$

The index L represents the Lth-order contribution to the vertex which transforms according to the μ-th irreducible representation of the point group symmetry of the crystal. The quantum numbers L, μ classify the anisotropy of the Raman fluctuations around the Fermi surface. The full momentum dependence is described by the addition of the basis functions with different weights γ_L^μ. In principle, all even L channels contribute to the Raman vertex for bands that are non-parabolic. By choosing light polarization vectors appropriately, one can select different L, μ channels which allow for different projections on to the Fermi surface. By selecting fluctuations on different regions of the Fermi surface, Raman scattering can provide information about the strength of the pairing at different **k**-regions on the Fermi surface. It is through the coupling of the Raman vertex and the energy gap that the polarization dependence of the spectra can be used to determine the momentum dependence of the order parameter.

It turns out that for a constant isotropic vertex ($L = 0$), the long-range Coulomb forces completely screen the response and the contribution to Raman scattering in the zero momentum transfer limit comes from energy bands with non-parabolic dispersion, i.e. from $L = 2$ and higher terms that represent intracell fluctuations. Since the sum in Eq. 5.22 converges rapidly, the $L = 2$ terms suffice to describe the Raman response. For tetragonal symmetry (D_{4h})of the crystal (relevant for the cuprates), one gets the following form for the Raman vertices

$$\gamma_{B_{1g}} \propto \cos 2\phi, \quad \gamma_{B_{2g}} \propto \sin 2\phi, \quad \gamma_{A_{1g}} \propto 1 + \cos 4\phi \tag{5.23}$$

where ϕ is the angle between $\mathbf{k}$ and the Cu-O bond direction within the CuO_2 plane, and the subscripts B_{1g}, B_{2g} and A_{1g} are the irreducible representations of the D_{4h} point group [116].

The first term on the right side of Eq. 5.16 is the "bare" Raman response which represents the attractive pairing interaction in the superconducting state while the second term arises as a result of Coulomb interactions (screening). The second term is zero for the non-symmetric B_{1g} and B_{2g} channels but contributes to partial screening in the fully symmetric A_{1g} channel. The "bare" Raman response can be rearranged to give

$$\mathrm{Im}\chi(\omega) \propto \frac{N_F}{\omega}\mathrm{Re}\langle\frac{\gamma(\mathbf{k})^2\Delta(\mathbf{k})^2}{\sqrt{\omega^2 - 4\Delta(\mathbf{k})^2}}\rangle \tag{5.24}$$

where N_F is the single particle density of states at the Fermi energy and the angular brackets denote a momentum integral over the Fermi surface. It is clear from Eq. 5.15 that if the superconducting gap is isotropic, then a "Cooper-pair breaking" coherence peak will manifest itself in the Raman spectrum at $\omega = 2\Delta$ and that there will be no Raman scattering intensity below this frequency. For anisotropic gaps with or without nodes, the position of the coherence peaks will depend upon the gap topology and upon properties of the Raman vertex whose selection depends on the polarization vectors of the incident and scattered photons.

The polarization directions of the incident laser ($\mathbf{e}_L$) and scattered ($\mathbf{e}_S$)photons

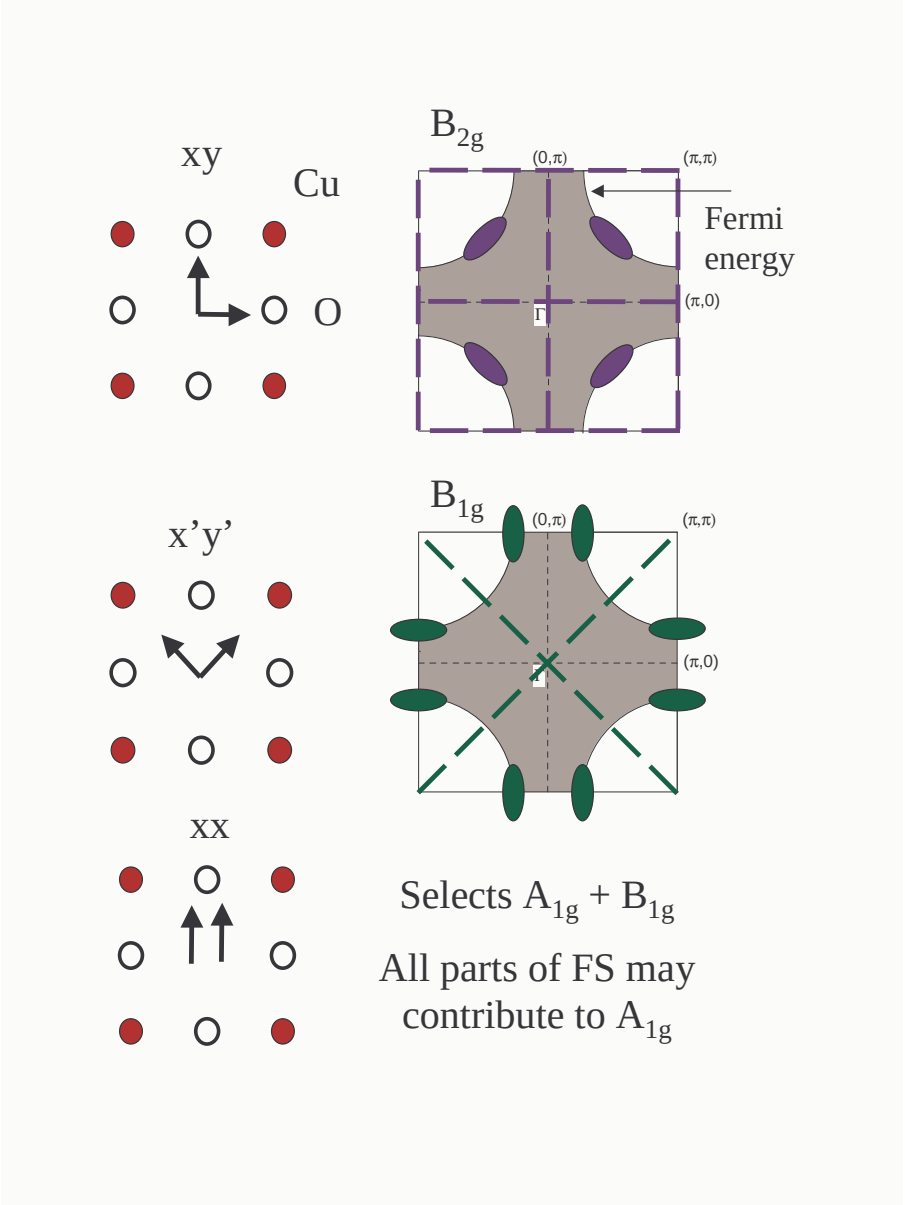

Figure 5.2: Probing the Fermi surface with polarized light. The squares represent the Brillouin zone. The area shaded gray represents filled quasiparticle states up to the Fermi energy. The B_{2g} channel probes the region shaded blue and the B_{1g} channel probes the region shaded green.

are indicated by ($\mathbf{e}_L$,$\mathbf{e}_S$) with x=[100], y=[010], x'=[110] and y'=[$\bar{1}$10]. The Cu-O bonds are along the [100] and [010] directions. The data in this thesis were taken in (x,y), (x',y') and (x,x) scattering geometries. For the tetragonal D_{4h} symmetry exhibited by the crystal lattices of PCCO and NCCO, these geometries correspond to B_{2g}+A_{2g}, B_{1g}+A_{2g} and A_{1g}+B_{1g} representations. Scattering in the A_{2g} channel is very weak in the cuprates. By using circularly polarized light, we confirmed this experimentally for both PCCO and NCCO. Therefore, for the two crossed polarization scattering geometries one essentially measures the B_{2g} and B_{1g} channels (also known as the non-symmetric channels). The electronic Raman response function for a given geometry ($\mathbf{e}_L$,$\mathbf{e}_S$)is proportional to the sum over the density of states at the Fermi surface weighted by the square of the momentum ($\mathbf{k}$) dependent Raman vertex (Eq. 5.15). In addition to the magnitude of the SC order parameter, ERS can provide information about its $\mathbf{k}$ dependence because the quoted scattering geometries selectively probe different regions of the FS. For the B_{2g} channel, the Raman form factor is maximum at the $(\pi/2, \pi/2)$ and equivalent regions of the Brillouin zone and vanishes along (0,0)$\rightarrow(\pi,0)$ and equivalent lines. The B_{1g} vertex is maximum at the $(\pi,0)$ and equivalent points and vanishes along the (0,0)$\rightarrow(\pi, \pi)$ and equivalent lines. This information will be used later to explain and interpret the ERS data on superconductors. See Fig. 5.2 for a pictorial representation of the relationship between light polarization and regions of FS. The Raman spectra in the A_{1g} channel (also called the fully symmetric channel) can be determined after subtracting the spectra measured in the (x',y') scattering geometry from those measured in the (x,x) scattering geometry. All regions of momentum space may contribute to the A_{1g} channel.

In a magnetic field perpendicular to the *ab*-plane of the samples, the Raman backscattering measurements have to be performed with circularly polarized light in the right-left (RL) and right-right (RR) scattering geometries. This is because the magnetic field does not affect the polarization of circularly polarized light. For the

tetragonal D_{4h} symmetry, the RL geometry corresponds to B_{1g}+B_{2g} representation. For the incident wavelength of 647 nm, it has been shown using linearly polarized light that the scattering in the B_{2g} channel is about an order of magnitude greater than that in the B_{1g} channel [19]. Therefore, the B_{2g} channel dominates the spectra in the RL scattering geometry. The RR scattering geometry corresponds to A_{1g}+A_{2g} representation. Since scattering in the A_{2g} channel is negligibly weak, the RR scattering geometry essentially probes the A_{1g} symmetry.

One of the main assumptions underlying the theory of Raman scattering in superconductors outlined above is that the optical band gap is larger than the incident photon energy and only intraband scattering contributes to the spectra. In the cuprates, this assumption does not hold and when the incident photon energy is similar to the optical band gap, interband transitions lead to a resonant enhancement of the Raman signal. Theoretical calculations of the cross-sections in the vicinity of resonances becomes difficult because it requires the knowledge of all bands involved. However, the theory outlined above serves as a useful starting point for analyzing the Raman spectra. Moreover, it has been observed experimentally that the position of the coherence peaks and the selection rules are quite robust and do not change significantly if the scattering is resonantly enhanced. [110, 19, 117]

5.3 Experiment

In the Raman experiment in zero magnetic field, monochromatic laser light is incident on the sample surface at an angle ($\approx 18^o$) to the normal to the surface of the sample to prevent directly reflected light from entering the Raman spectrometer. Due to the high refractive index of the cuprates, the incident photons propagate at a small angle to the surface normal. The inelastically scattered photons are mostly scattered back into a solid angle Ω. This is known as the backscattering geometry. The laser, Raman spectrometer, external optical equipment and the cryostat rest

upon a heavy bench to minimize effects of vibrations. The Raman spectra are taken in the dark with extraneous sources of light switched off.

The single crystal and films are glued to a copper holder with either silver paint or GE varnish. The copper holder is screwed on to a non-magnetic stainless steel rod that is inserted inside a optical cryostat with fused silica windows at one end for letting light through. The cryostat can be cooled through a continuous flow of cold helium gas and can operate in a temperature range between 300 K and 1.6 K. A liquid helium reservoir is attached to the cryostat from which helium gas is drawn into the cryostat through a needle valve. This occurs because the pressure inside the cryostat is kept below the pressure in the reservoir by a vacuum pump connected to the cryostat. Liquid helium is continuously sucked into the reservoir through a transfer line from a liquid helium dewar. A heater coil and thermometer are located inside the cryostat near the sample and allow the temperature to be monitored and controlled.

A schematic diagram of the Raman setup is shown in Fig. 5.3. The monochromatic linearly polarized light is provided by a Kr^+ laser. This laser can provide discrete wavelengths in the visible and near infrared (IR) spectral range. Most of the measurements on PCCO and NCCO were performed with 647 nm red wavelength. The 799 nm wavelength in the near IR was also used for some of the measurements. One advantage of using longer wavelength light is that the intensity of elastically scattered light decreases for longer wavelengths and the Raman spectra can be measured down to a few wavenumbers from the laser line. This turns out to be important because the low frequency behavior of the Raman spectra in the superconducting state can reveal the presence or absence of nodes in the order parameter.

Electronic Raman scattering is in general a very weak second-order effect with a small scattering cross-section. Normally, to obtain a good signal to noise ratio for the coherence peaks in the superconducting state requires long exposure times (one

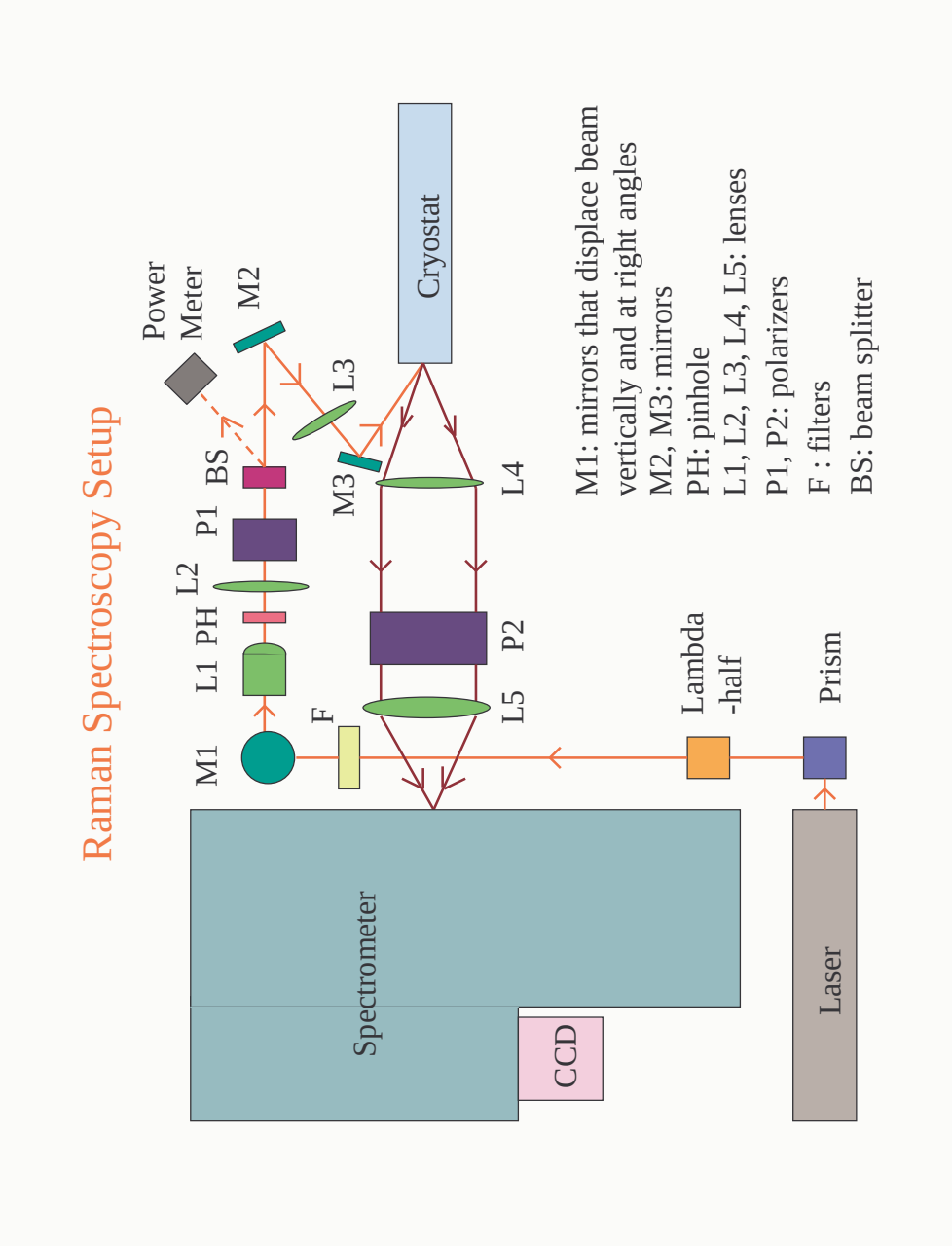

Figure 5.3: A schematic diagram of Raman spectroscopy setup

to two hours). The scattering intensity is proportional to the incident laser power but in the superconducting state the power has to be kept very low ($\approx$ 0.5 mW or less) in order to minimize heating that could drive the superconductor into the normal state. This issue becomes quite acute in the over-doped and under-doped samples of PCCO and NCCO which have a low T_c. It turns out that the scattering in the B_{2g} channel is in resonance for the 647 nm wavelength light. This increases the coherence peak intensity by several times in that channel and leads to better signal to noise ratio.

The laser produces weak secondary plasma lines in addition to the primary excitation. These plasma lines need to be filtered out because they can appear in the spectra at low frequencies. To accomplish this, the laser light is dispersed by a prism and then focused by a lens (L1) on to a pin-hole (PH) with diameter of a few microns. The focal length of the lens is different for different wavelengths. Therefore, the distance between the lens and the pin-hole is adjusted until only the primary wavelength is focused through the pin-hole and the secondary wavelengths are filtered out. This arrangement is also known as a "spatial" filter. The pin-hole arrangement can be adjusted by the operator to obtain a homogeneous beam.

The incident polarization direction can be changed with an optical device known as $\lambda/2$ (lambda-half) retarder. The $\lambda/2$ and a polarizer downstream of it enable the operator to select the polarization direction of the incident light. Two sets of neutral density filters (F) are used to adjust the power of the incident laser to the desired level. A beam splitter sends a small fraction of the power to the detector of a power meter. The known attenuation factor allows the power meter to read out the actual incident power. Incident powers used are typically 3-4 mW for measurements above T_c, and about 0.5 mW for measurements in the SC state to minimize heating of the sample.

The lenses L2 and L3 ensure that the incident light gets focused on to the sample in the cryostat with a spot size of 50 μm by 100 μm. The optical cryostat is

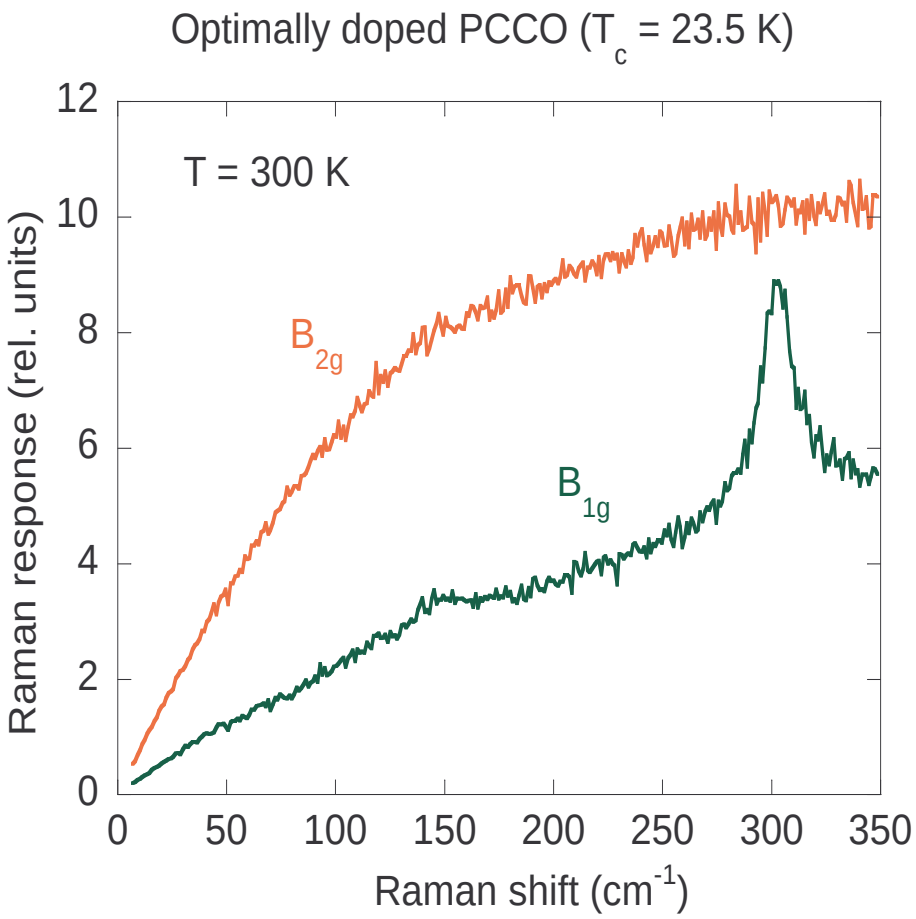

Figure 5.4: The low frequency part of Raman spectra from an optimally doped PCCO crystal in B_{2g} and B_{1g} channels obtained at room temperature.

mounted on a stage that can be moved in all three XYZ directions. This is required for focusing the laser spot on the sample and for choosing particular regions of the sample for the experiment. The back-scattered light is collected by a collimating lens (L4) forming a parallel beam which is incident upon the Analyser (P2). The polarized scattered light is focused by lens L5 on to the entrance slit of the Raman spectrometer. A camera connected to a monitor screen allows the operator to view the sample and laser spot and make necessary adjustments.

The polarization axis of the Analyser is always parallel to the optical bench and allows light parallel to the optical bench to pass through. The polarization of the incident light can be changed with the lambda-half and polarizer P1 so that

experiments with crossed and parallel polarizations can be performed. Crossed polarization means that the scattered and incident light has polarization vectors perpendicular to each other and parallel polarization means that the direction of polarization of incident and scattered light is the same. For accessing different channels (B_{1g}, B_{2g}, A_{1g}), the sample has to be oriented such that the polarization vectors are parallel to or 45 degrees to the Cu-O bonds (see Fig. 5.2). This can be done by rotating the rod on which the sample is mounted. For the films the Cu-O bonds are parallel to the substrate edges. For crystals, this information needs to be determined. Usually, the Cu-O bonds are along one of the longer edges of the trapezoid-shaped crystals. This is checked by taking a spectrum at room temperature with crossed polarizations and the incident polarization along the edge or perpendicular to the edge. If the Cu-O bonds are along the relevant edge then one is probing the B_{2g} channel and the B_{1g} active phonon should not appear in this channel. If a sign of B_{1g} phonon is seen in the spectrum, the crystal is rotated slightly and the spectrum retaken and this procedure is repeated until there is no sign of B_{1g} phonon in the spectrum. Thus the Cu-O bond direction is determined. The B_{1g} active phonon is an oxygen vibration mode whose frequency at room temperature is about 300 cm^{-1} for PCCO and 335 cm^{-1} for NCCO. See Fig. 5.4 for the B_{1g} and B_{2g} spectra showing the presence and absence of this phonon respectively.

A stated earlier, the incident laser light is directed at an angle of about 18^o to the surface normal of the crystals and films. Most of the inelastically scattered light is scattered backwards along the surface normal. This (pseudo)backscattering geometry prevents most of the specularly reflected laser light from entering the spectrometer inlet slits. Moreover, the (pseudo)backscattering geometry helps in rejection of luminescence from the substrate. Even with one micron thick films, a few percent of laser light reaches the substrate and causes a luminescent "shadow" spot that has a small partial overlap with the main laser spot. The main spot is accommodated within the slits in such a way so as to minimize luminescence from

entering the slits. This results in some loss of Raman signal. However, the Raman spectra from the films are scaled such that the B_{1g} phonon intensity in the films matches the B_{1g} phonon intensity in the crystals of similar Ce doping.

The Raman spectrometer at Lucent-Bell Labs is a custom high performance spectrometer that was designed for maximum throughput of inelastically scattered light and rejection of stray light (see Fig. 5.5). It consists of three stages containing highly dispersive diffraction gratings and parabolic/spherical mirrors. The resolution and desired frequency range depends on the number of grooves per mm of the grating as well as the wavelength of the incident light. The spectrometer has excellent rejection of elastically scattered laser light compared to standard spectrometers and Raman frequency shifts down to a few wavenumbers can be measured with it. A "cut-off" slit in the intermediate stage has to be adjusted to eliminate stray light in the spectra. The temperature of the room is controlled because thermal expansions/contractions may cause reduction of throughput and errors in measuring frequency shifts.

The inelastically scattered light passes through an exit slit and on to a liquid nitrogen cooled charge coupled device (CCD) that acts as a light detector. The CCD consists of a two-dimensional array of photo-sensitive elements composed of silicon, each of which generates photoelectrons and stores them as a charge. Charges are stored on each individual pixel as a function of photons striking that pixel. Each column of pixels represents a frequency shift and the charges on the rows of each column are added at the end of the exposure time to give the relative intensity of light. Since the intensity of inelastically scattered light is weak, the pixel columns are typically "binned" together in groups of four to obtain better signal to noise ratio. This is done at the expense of resolution of the frequency shift, which after binning, is still good and is about 1 cm^{-1} ($\approx$ 0.13 meV) for 647 nm laser light. Each period of exposure time is called a "frame". Typically, each frame is a minute long and twelve frames are averaged to improve signal to noise ratio. In the superconducting

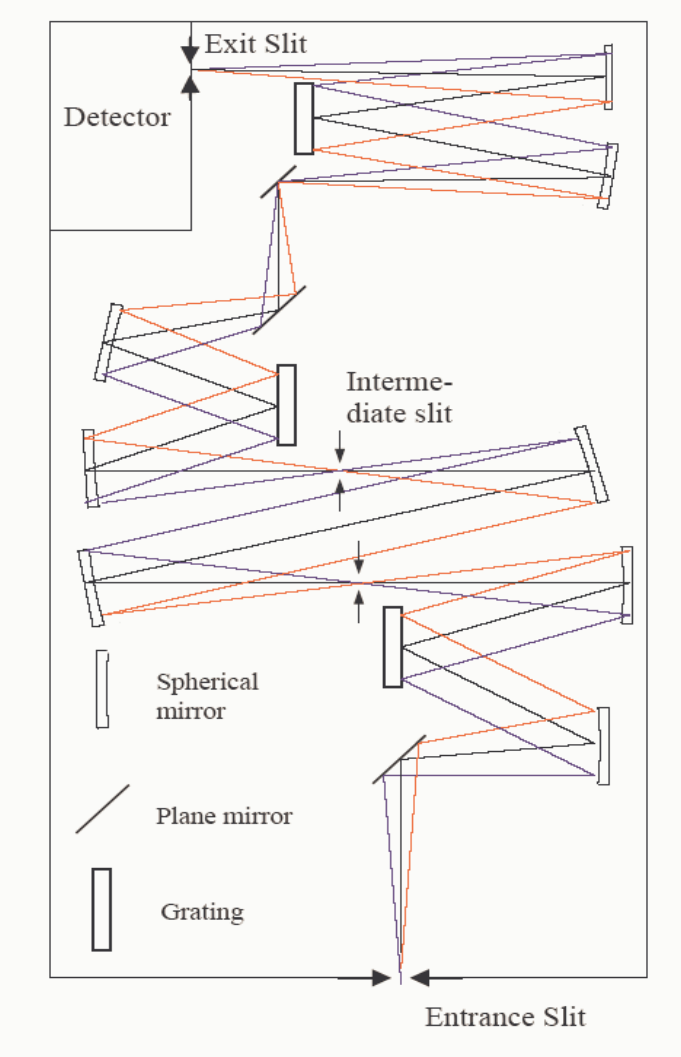

Figure 5.5: Schematic diagram of the Raman spectrometer. The colors are a guide to the eye for following different optical paths. Taken from Ref. [118].

state, where significantly lower incident laser power is used to minimize heating, each frame is taken for five minutes and twelve frames are averaged together.

The spectrometer settings, for example, the widths of the entrance and exit slits, the position of the"cutoff", power readings etc. are controlled remotely by a Labview computer program. The CCD operation, which includes duration of each frame, the number of frames and the binning, is controlled by a proprietary software by Princeton Instruments called Winspec. The spectral data essentially consists of the intensity of light and the frequency shift values. Before the data can be plotted, "spikes" in the data due to muons going through the pixels need to be removed. The flux of muons varies with solar activity and the probability that a muon will pass through a pixel causing a spike is proportional to the duration of a frame. So a five minute frame is likely to contain more spikes than a one minute frame. On average, there is one spike per one minute frame. A spike usually affects one data point i.e.(a "bin" of four pixels) but could also affect adjacent data points in a frame. A spike causes a significant increase in the measured intensity and this actually makes it easier to handle them. The spikes are handled with a computer program that does statistics on the data from all the frames and uses these statistics to detect and remove spikes. It is also important that many frames of data are taken for an efficient removal of spikes. After the spikes are removed, the "background" due to electrical noise in the CCD is subtracted from the spectra. Many "background" frames are obtained with all lights off and then averaged together. Each frame is of one minute or five minute duration.

It can be seen from equations 5.12 and 5.14 that the differential scattering cross-section is proportional to the imaginary part of the Raman response function. The solid angle for all experiments presented here is the same and is a constant factor that is ignored in the analysis since we are interested in the variation of the scattering with frequency i.e. $\mathrm{d}\sigma/\mathrm{d}\omega$. It is also extremely difficult to calculate the absolute value of differential cross-section because it depends on unknown frequency-

dependent factors, for example, the self-absorption of the samples and the losses due to external optical equipment. Therefore, $d\sigma/d\omega$ is evaluated in arbitrary units and its relative variation for samples of different dopings is the relevant issue.

$$\frac{d\sigma}{d\omega} \propto \lambda^2 \frac{d\sigma}{d\lambda} \tag{5.25}$$

This equation merely relates the derivative of the cross-section with respect to frequency to the derivative with respect to the wavelength (λ) of scattered light.

$$\frac{d\sigma}{d\lambda} \propto \frac{I}{t} \frac{1}{P\lambda_L} \frac{1}{R} \tag{5.26}$$

Here I/t is proportional to the number of scattered photons of a particular wavelength (or frequency) per unit time reaching the CCD. "I" is the output of the detector and "t" is the time in seconds for one frame. "P" is the incident laser power and λ_L is the wavelength of the laser. Therefore, $P\lambda_L$ is proportional to the number of incident photons per unit time. The quantity $d\sigma/d\lambda$ is proportional to the scattered photon flux per unit time normalized to the incident photon flux per unit time and the response (R) of the spectrometer and CCD. This response is a function of frequency and is determined using a calibrated source of pure white light from a lamp.

The imaginary part of the Raman response function is obtained first by computing $d\sigma/d\omega$ from the raw data (I) using the above equations and then dividing $d\sigma/d\omega$ by the Bose factor $(1+n(\omega))$. The Bose factor takes care of the temperature dependent Bose-Einstein statistics obeyed by the photons. The form of this factor is correct for scattered photons that are Stokes-shifted i.e. their frequency is less than the frequency of the incident photons. In all our Raman experiments, we measure Stokes-shifted spectra. The Raman data presented in this thesis consists of plots of the imaginary part of the Raman response function in relative units on the vertical axis versus the frequency shift (Raman shift) in wavenumbers on the horizontal axis. Following the conventions in the Raman literature, the vertical axes

are labelled the "Raman Response" where it is understood that it is the imaginary part of the Raman Response function that is being measured.

Some modifications in the external optics need to be made when performing measurements in a magnetic field. The cryostat has to be inserted into the bore of a horizontal solenoidal superconducting magnet from Oxford Instruments. Since the sample is well inside the bore, the pseudo-backscattering geometry used in zero field for preventing the specularly reflected light from entering the spectrometer cannot be used here. The lens L3 and the mirror M3 are removed. Another mirror is placed in front of the optical window of the cryostat such that it reflects only one-third of the incident laser light on to the sample at an angle of almost 90 degrees to the ab-plane of the sample. The incident light is focused into a spot almost 50 μm diameter by a lens on to the sample. This lens replaces lenses L3 and L4 and also collects the scattered light from the sample forming a parallel beam. Most of the specularly reflected laser light is still prevented from entering the spectrometer because of a small angle (a degree or so) between the normal to the sample surface and the incident light.

The Raman spectra in a magnetic field are acquired using circularly polarized light. A special polarizer called the "Berek" ($\lambda/4$ retarder) is employed to convert linearly polarized light into right circularly polarized light. The scattered light consists of both right and left circularly polarized light. A $\lambda/4$ plate is placed before the Analyzer P2 and converts left circularly polarized light into light polarized along the axis of the Analyzer which allows it to pass through into the spectrometer. This is the right-left scattering geometry. The right-right scattering geometry is accessed by rotating the $\lambda/4$ plate by 180^o about the vertical axis.

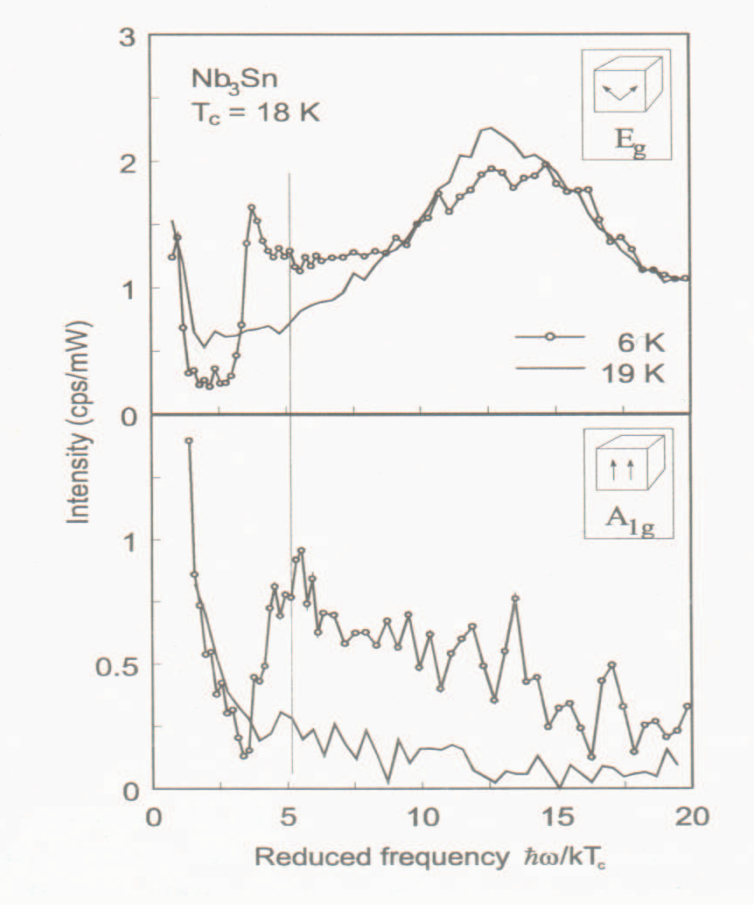

Figure 5.6: Raman spectra from Nb_3Sn. (from Ref. [113])

5.4 Electronic Raman Spectroscopy of conventional superconductors

The first report of signatures of superconductivity obtained from Raman spectroscopy was on $NbSe_2$ [44]. The observed features occurred below T_c and vanished at H_{c2}. These features were interpreted as bound states within the SC gap. Later, coherence peaks due to pair-breaking excitations were observed in Nb_3Sn and V_3Si [45, 46].

Fig. 5.6 shows the pair-breaking features in the SC state of Nb_3Sn for two scattering symmetries [113]. Notice the sharp drop in scattering below the coherence peaks. This is expected for a superconductor with a fully gapped FS (s-wave gap). Also

notice an intensity threshold in the E_g channel with some residual scattering. There should be no Raman scattering below the gap energy in an s-wave superconductor and the residual scattering has been attributed to degraded surface layers.

In order to obtain reference spectra for an s-wave superconductor, we performed ERS on a sample of $NbSe_2$. This material has a T_c of 7.2 K, is essentially two-dimensional and cleaves easily to yield an atomically flat surface that is ideal for ERS. Spectra shown in Fig. 5.7 were obtained in E symmetry for cross-polarization [(xy)] and in A symmetry [$(xx\text{-}xy)$] using parallel polarization [(xx)].

One can see that excitations out of the SC state result in re-normalization of the spectra below T_c. The SC order parameter couples with the charge density wave in this material to give Raman active "gap modes" in A and E symmetries at frequencies just below 2Δ. Scattering decreases rapidly for frequencies below the gap modes reaching a threshold with small residual scattering. The small residual scattering may be attributed to minor changes in the background noise of the CCD. To summarize, we obtained reference spectra for a clean s-wave superconductor in order to compare with the spectra for over-doped PCCO and NCCO.

5.5 Electronic Raman Spectroscopy of hole-doped high-temperature superconductors

Early ERS on the p-doped cuprates showed symmetry dependent pair-breaking peaks and a continuously decreasing scattering intensity below them with no threshold. The spectra were different enough from those of conventional s-wave superconductors to invite several novel explanations [119]. Later on, the spectra were interpreted in terms of d-wave symmetry of the SC order parameter. Many different types of experiments now support d-wave pairing symmetry in the p-doped cuprates.

A $d_{x^2-y^2}$ order parameter has a maximum gap at the (π,0) and equivalent points.

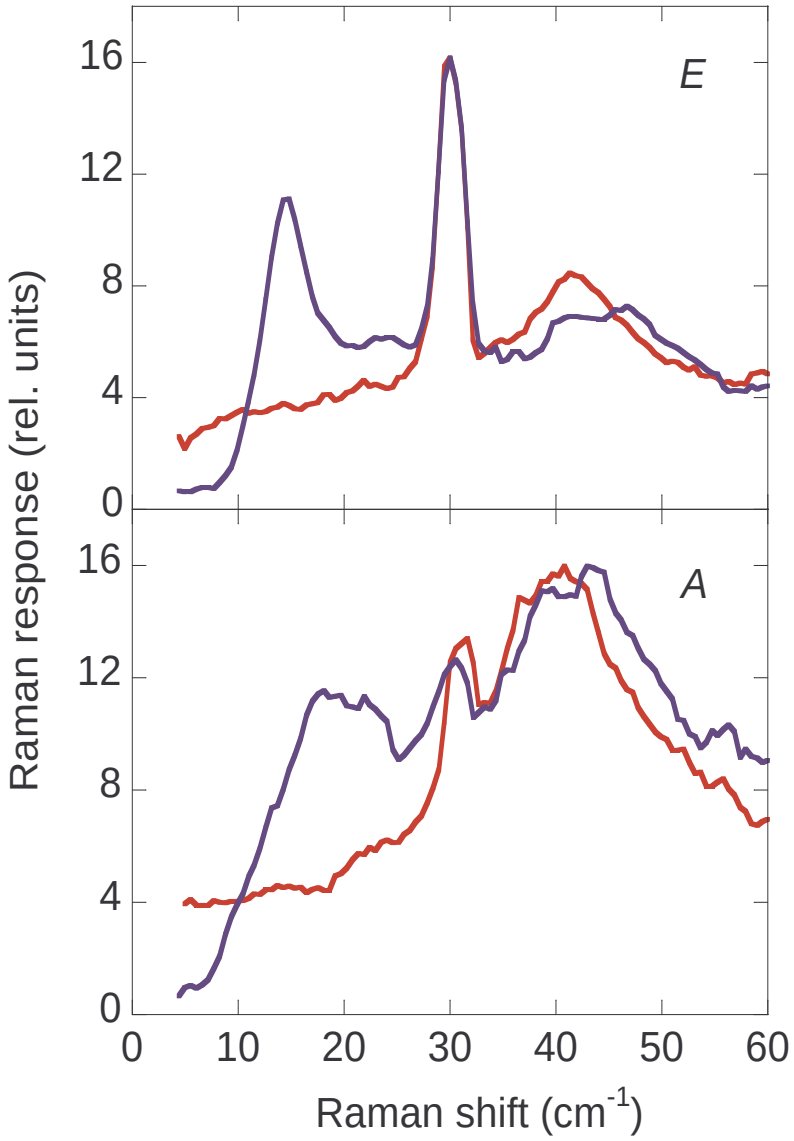

Figure 5.7: Raman spectra from $NbSe_2$ in E and A symmetries. Spectra are obtained with 799 nm incident laser light in the normal state at $T = 12$ K (red curves) and in the SC state at $T = 4$K (blue curves).

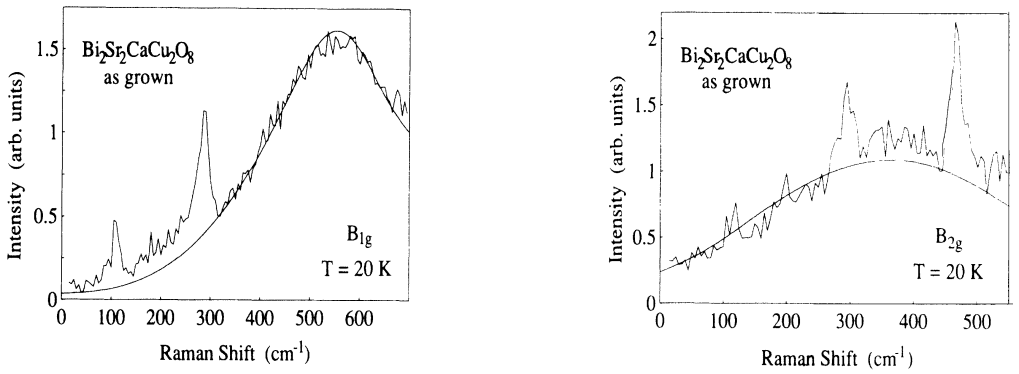

Figure 5.8: Raman spectra from optimally doped Bi-2212. The smooth solid lines are fits to the data. The maxima of the fits correspond to the coherence peak positions. Note that the coherence peak occurs at a higher energy in the B_{1g} channel ($\approx$ 550 cm^{-1}) compared to the B_{2g} channel ($\approx$ 350 cm^{-1}) as expected for a $d_{x^2-y^2}$ order parameter. The sharp features are due to phonons. Taken from Ref. [120].

The gap vanishes along the (0,0)$\rightarrow$(π,π) direction. Therefore, ERS in the B_{1g} channel is expected to show the coherence peak at higher energies compared to the spectra in B_{2g} and A_{1g} channels (see Fig. 5.8). This has been experimentally confirmed in several p-doped cuprates [120, 121, 122].

Another feature of a clean $d_{x^2-y^2}$ order parameter ($\Gamma << 2\Delta$) is that the sub-gap scattering will have a characteristic low frequency dependence in different channels. For $\omega \rightarrow 0$, $\chi"_{B_{1g}} \propto \omega^3$, $\chi"_{B_{2g}} \propto \omega$ and $\chi"_{A_{1g}} \propto \omega$. These low-frequency power laws have also been confirmed for p-doped cuprates.

In over-doped Bi-2212, however, all channels showed symmetry independent coherence peak positions [123, 124, 125]. However, the low frequency behavior was different in the B_{1g} and B_{2g} channels. In the B_{1g} channel, starting from the lowest frequency, the data was linear giving way to a cubic frequency dependence at higher frequencies. In the B_{2g} channel the data was linear. These low frequency power laws led to a consensus that the SC order parameter retained nodal character in over-doped Bi-2212. However, no quantitative model for explaining the symmetry

independent coherence peak positions exists.

Chapter 6

Electronic Raman spectroscopy of $Pr_{2-x}Ce_xCuO_{4-\delta}$ and $Nd_{2-x}Ce_xCuO_{4-\delta}$

This chapter begins with a discussion of early Raman measurements on NCCO followed by comparison with more recent data on optimally-doped NCCO. The polarization dependence of Raman data on various dopings of PCCO and NCCO in zero magnetic field is presented next. This is followed by analysis and discussion of data at different temperatures and magnetic fields.

6.1 Discussion of Raman data on optimally doped NCCO

The first Raman scattering measurements on the electron-doped cupartes that showed the pair-breaking 2Δ coherence peaks in the SC state were performed by Stadlober *et. al.* [20]. Their data in the B_{1g} and B_{2g} symmetries is shown in Fig. 6.1. One can see that the Raman data is unlike the data on the hole-doped cuprates. First, positions of the coherence peaks in the two channels are almost the same, with the peak position in the B_{2g} channel slightly larger than the peak position in the B_{1g}

channel. This is not expected for Raman data on a superconductor with a monotonic $d_{x^2-y^2}$ order parameter where the coherence peak position in the B_{1g} channel should be larger than in the B_{2g} channel. Secondly, a sub-gap threshold in scattering is observed in both channels. These two features led the authors to interpret their data in terms of a slightly anisotropic s-wave gap. This was in accord with early tunneling and penetration depth data on NCCO that suggested an s-wave gap. One should point out that there was considerable residual sub-gap scattering in the Raman data which the authors attributed to Rayleigh scattering of the laser light and/or to scattering from degraded surface layers. Moreover, their data was measured down to a Raman shift of only 25 cm^{-1}.

The observation of the half-flux quantum in a tri-crystal grain boundary junction experiment [18] on optimally doped PCCO and NCCO provided unambiguous evidence for a predominantly $d_{x^2-y^2}$ gap in these materials (at optimum doping). Moreover, the interpretation of the penetration depth data on NCCO was questioned when it was pointed out that the magnetic moments of Nd^{3+} ions may alter the temperature dependence of the penetration depth [61]. Subsequent penetration depth studies on PCCO, which does not suffer from the magnetic moment problem, revealed the presence of a superconducting gap with nodes [21, 22]. These results led to a renewed interest in repeating the Raman measurements on NCCO.

Blumberg *et al.* carried out ERS on an optimally doped NCCO crystal [19]. Their results are shown in Fig. 6.2. They found that, in accordance with the earlier data, the coherence peak position was larger in B_{2g} channel compared with that in the B_{1g} channel. However, they also found that there was no scattering threshold in the Raman spectra down to much lower frequency shifts (10 cm^{-1}). The scattering decreased smoothly below the gap down to the lowest measured frequency shift. This led the authors to conclude that the data was incompatible with a clean s-wave gap and the gap had nodes. Moreover, a cubic low frequency power law was observed in the B_{1g} channel data [126]. This meant that the nodes were in the (0,0)$\rightarrow(\pi,\pi)$

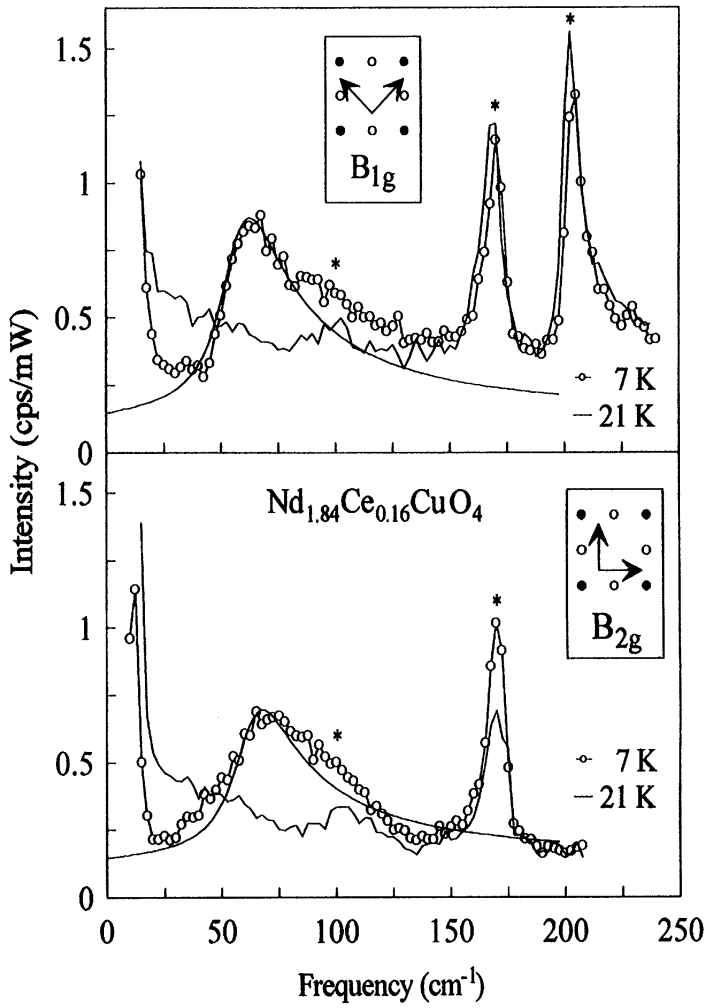

Figure 6.1: Electronic Raman spectra of NCCO near optimum doping. The figure is taken from Ref. [20]. The smooth solid lines are fits to anisotropic s-wave gap.

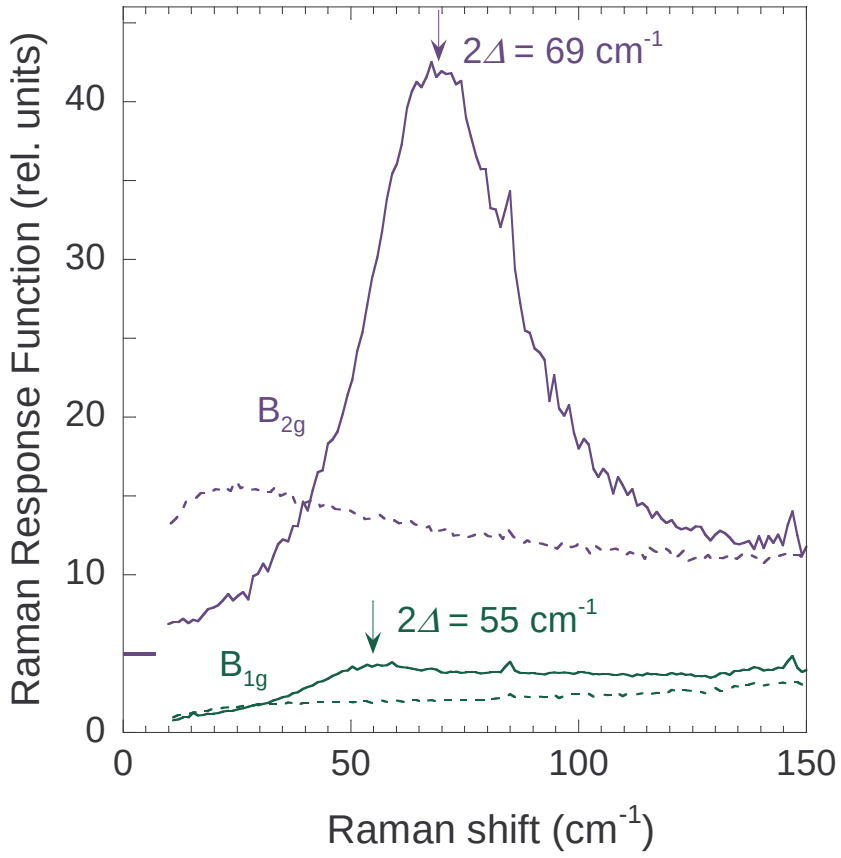

Figure 6.2: Electronic Raman spectra of NCCO at optimum doping. The figure is adapted from Ref. [19]. The spectra are obtained in the SC state at $T = 5$ K.

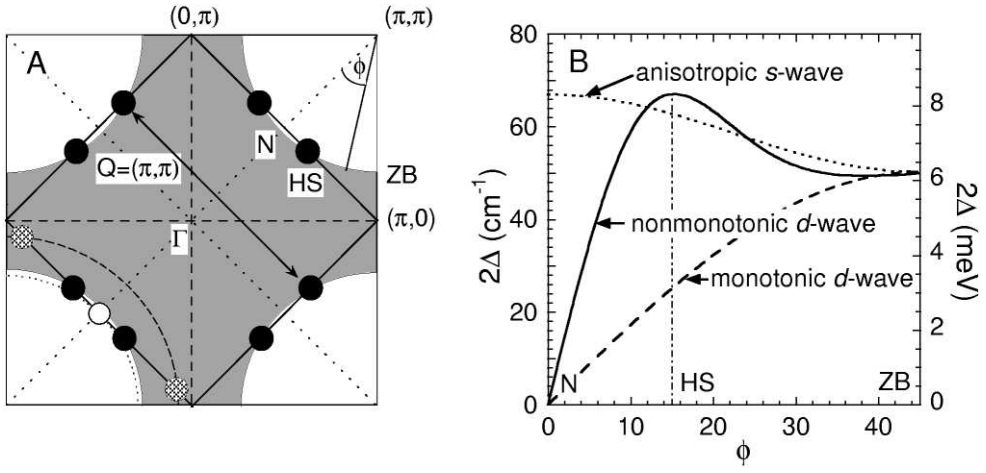

Figure 6.3: Schematic representations of (A) the Fermi surface of NCCO and (B) functional forms of various order parameters. The figure is taken from Ref. [19].

direction as expected for a predominantly $d_{x^2-y^2}$ gap. However, the coherence peak positions in the two non-symmetric channels did not support a conventional $d_{x^2-y^2}$ gap. Blumberg *et al.* [19] explained the data by postulating a non-monotonic d-wave gap with the gap maxima closer to the nodal direction than to principal axes of the Brillouin zone. In addition to the $\sin 2\phi$ form of the monotonic $d_{x^2-y^2}$ gap (ϕ is the angle measured from the Brillouin zone diagonals), the non-monotonic d-wave gap has higher harmonics (eg. $\sin 6\phi$, $\sin 10\phi$ etc.) that preserve the nodes in the (0,0)$\rightarrow$(π,π) direction and allow for a gap maximum closer to the nodal direction (see Fig. 6.3B). This explains why the coherence peak position is larger in the B_{2g} channel.

The position of the maximum gap most likely corresponds to the position of the "hot spots". These "hot spots" occur at the intersection of the FS with the antiferromagnetic Brillouin Zone where antiferromagnetic fluctuations enhance interactions between electronic excitations and are believed to mediate pairing in the SC state (see Fig. 6.3A). The "hot spots" are connected by the $\mathbf{Q} = (\pi,\pi)$ vector. In the electron-doped HTSC, the "hot spots" exist closer to the (0,0)$\rightarrow$(π,π) diag-

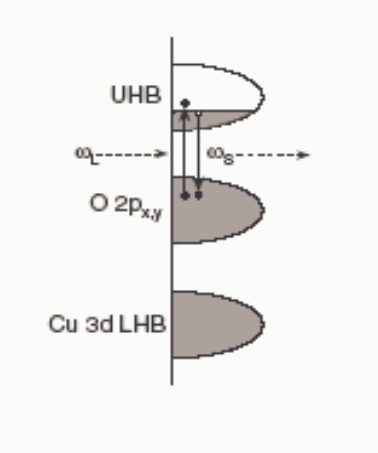

Figure 6.4: Schematic diagram for the resonant electronic Raman scattering process in electron-doped cuprates. The figure is taken from Ref. [19].

onal (solid circles) and lead to enhanced 2Δ peak energy in the Raman spectra in B_{2g} symmetry compared to B_{1g} symmetry. This is in contrast to the hole-doped HTSC where the "hot-spots" exist closer to the principal axes of the Brillouin Zone (hatched circles) and consequently the 2Δ features occur at higher energies in the B_{1g} Raman spectra [120, 121].

The resonant Raman excitation profile was also studied in Ref. [19]. The intensity of the 2Δ peak was obtained as a function of discrete laser excitation frequencies from blue to near IR. It was observed that the 2Δ peak intensity in the B_{1g} channel does not change much with laser excitation wavelength. The intensity in the B_{2g} channel shows a resonant enhancement by an order of magnitude for 647 nm (red) excitation wavelength (1.9 eV photon energy) compared to the intensity obtained with blue light. The resonant enhancement is due to inter-band transitions with the oxygen $2p$ band as the intermediate state. This is the same state seen in optical conductivity near 2.1 eV. ARPES spectra also exhibit a band that is peaked at 2.6 eV below the Fermi energy near the $(\pi/2, \pi/2)$ point. The excitation out of this band to the Upper Hubbard Band (UHB) may cause the 2.1 eV transition in the optical conductivity. The slight downscale in energy is due to final state interactions.

Fig. 6.4 shows a schematic diagram for resonant electronic Raman scattering in the electron-doped cuprates. The lower Hubbard band (LHB) and the oxygen band are fully occupied in the parent compound. Doped electrons shift the Fermi energy to the UHB. Resonant enhancement of the Raman scattering process occurs when the energy of the incoming or scattered photons, or both, is the same as the energy gap between the UHB and the oxygen band.

6.2 Doping and polarization dependence of the SC gap

We have performed a systematic study of the polarization dependence of the Raman spectra of electron-doped cuprates with different Ce doping levels that cover the entire SC phase. The spectra were obtained in the SC state at the lowest achievable temperature ($\approx$ 4 K) and also just above the respective T_c of the samples. The spectra were taken with 647 nm and 799 nm incident laser light. PCCO crystals and films as well as NCCO crystals were used in this study.

The Raman data on the PCCO samples for B_{2g}, B_{1g} and A_{1g} symmetries is presented in Fig. 6.5. In the B_{2g} and A_{1g} channels, the pair-breaking 2Δ peaks appear in the SC state for all dopings. In the B_{1g} channel, the 2Δ peaks are absent in the under-doped film and the most over-doped film. This suggests that the gap vanishes along the principal axes (0,0)$\rightarrow$(π,0) of the Brillouin Zone for these dopings and is primarily of B_{2g} character. The gap is anisotropic for optimum doping (x $\approx$ 0.147, $T_c \approx$ 23.5 K) with the peak energy being larger for the B_{2g} channel compared with that in B_{1g} channel. Below the 2Δ peak, the spectra go smoothly towards zero in both symmetries and there is no Raman intensity threshold down to the lowest frequency measured (7 cm^{-1}). The absence of a threshold found in s-wave superconductors [45, 46]precludes any interpretation in terms of a clean fully

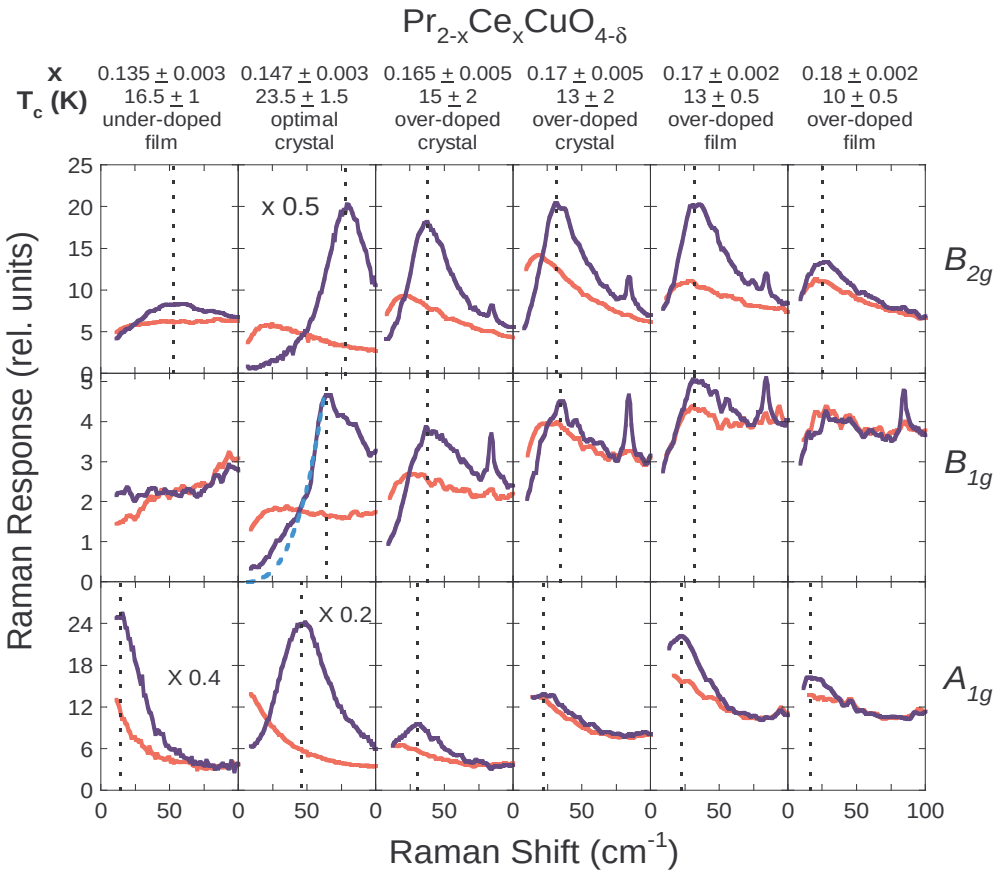

Figure 6.5: Doping and polarization dependence of the low energy electronic Raman spectra of single crystals and films of PCCO. The first, second and third rows show the Raman spectra obtained with 647 nm laser light in the B_{2g}, B_{1g} and A_{1g} channels respectively. The columns are arranged from left to right in order of increasing cerium doping. The solid red curves are the data obtained just above the respective T_c of the samples. The solid blue curves show the data taken in the SC state at 4 K. The dashed curve (light blue) is a cubic fit to the B_{1g} data for the optimally doped crystal. The dashed vertical lines show the peak positions of the 2Δ features.

gapped Fermi surface . This new data on optimally doped PCCO is consistent with the earlier data on optimally doped NCCO that was interpreted in terms of a non-monotonic d-wave order parameter [19]. Moreover, the low frequency data in the SC state in the B_{1g} channel for optimally doped PCCO and NCCO crystals can be fitted to a cubic power law of the form $\alpha\omega^3$, where α is a fitting parameter (see Fig. 6.5 and Fig. 6.7). This strengthens the case for nodes along the (0,0)$\rightarrow(\pi,\pi)$ direction. We note that the data fits well to the cubic power law at higher frequency shifts but deviates from it at very low frequency shifts due to quasiparticle scattering. Nodes in the (0,0)$\rightarrow(\pi,\pi)$ direction would lead to a linear low frequency behavior in the B_{2g} channel for non-resonant scattering [109]. However, the power law may change for resonant Raman scattering. It appears that resonance due to inter-band transitions at 647 nm (1.9 eV) excitation in the B_{2g} channel changes the power law behavior in this channel [19]. We do not observe a linear low-frequency power law in the B_{2g} channel for the 1.9 eV excitation. There are no definitive theoretical calculations for the low frequency power law behavior for resonant Raman scattering with which we can compare our B_{2g} data.

The gap becomes symmetry-independent in the two over-doped crystals and the over-doped film (x = 0.17), with the coherence peak positions at the same energies for both B_{2g} and B_{1g} symmetries. The peak positions and intensities also decrease in the over-doped regime compared to the optimally doped sample. The crystals and the film show similar behavior, further indicating the good quality of the films. The Raman response decreases smoothly towards zero below the 2Δ peaks and no well-defined threshold is observed down to the lowest frequency measured (7 cm^{-1}).

A symmetry-independent gap with continuously decreasing Raman scattering down to low frequencies has also been observed in the Raman spectra in over-doped samples of the hole-doped HTSC Bi-2212 [123, 124, 125](see Fig. 6.6). The gap energies are the same in B_{1g}, B_{2g} and A_{1g} symmetries. The 2Δ peak position in the A_{1g} channel is sensitive to the effects of Coulomb screening, details of the band

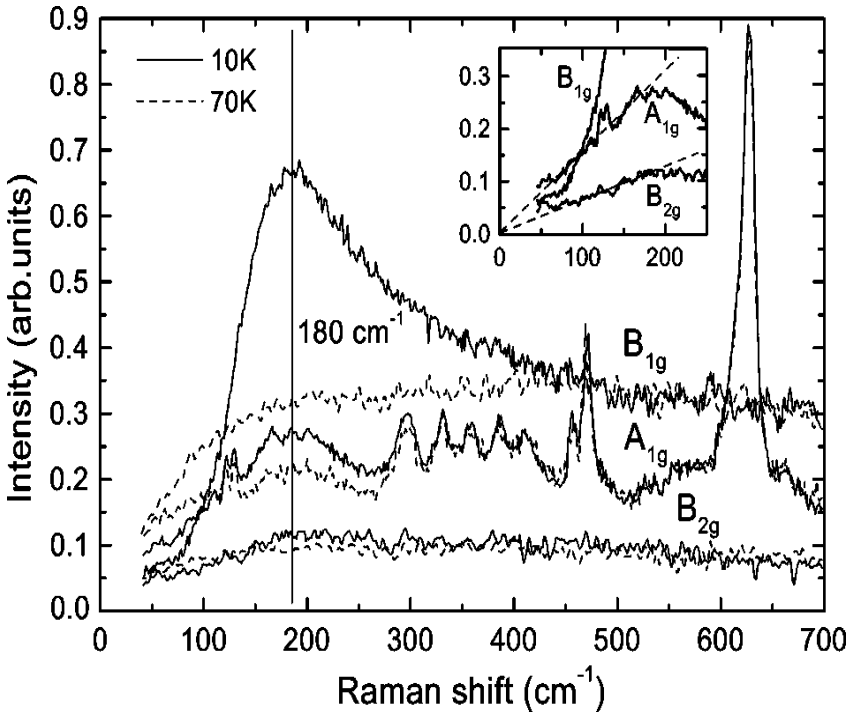

Figure 6.6: Electronic Raman spectra of heavily over-doped Bi-2212 ($T_c = 55$ K) in B_{1g}, B_{2g} and A_{1g} channels. Figure is taken from Ref [125].

structure, and higher order harmonics of the gap function and the Raman vertex, while this is not the case for the B_{1g} and B_{2g} symmetries [109]. Even if the data in the A_{1g} channel is ignored, the coincidence of gap energies in the B_{1g} and B_{2g} symmetries has yet to be explained within the framework of a monotonic d-wave order parameter. Nevertheless, the continuously decreasing Raman scattering below the gap energies with linear and cubic low-frequency power law behaviors in the B_{2g} and B_{1g} channels respectively led to a consensus on the presence of nodes in the gap along the Brillouin zone diagonals. Phase sensitive experiments on the over-doped p-type cuprates have indeed confirmed that the order parameter is predominantly $d_{x^2-y^2}$ [17].

At first sight, our Raman data on over-doped samples of the electron-doped HTSC for the two crossed polarizations is similar to the earlier Raman data on over-

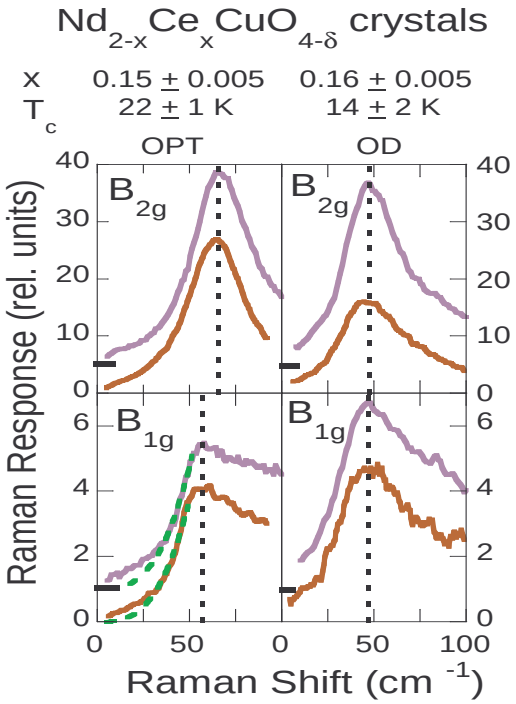

Figure 6.7: A comparison of the Raman spectra in the superconducting state for optimally doped (first column) and overdoped (second column) NCCO. The first and second rows show spectra for B_{2g} and B_{1g} channels respectively. The violet and brown curves are data taken with red laser excitation ($\lambda_L = 647$ nm) and infrared excitation ($\lambda_L = 799$ nm) respectively. The B_{2g} and B_{1g} data for $\lambda_L = 647$ nm has been shifted up by 5 units and 1 unit respectively. All spectra are taken at T $\approx$ 4K. The dashed vertical lines show the peak positions of the 2Δ features. The low frequency power law fits to the B_{1g} spectra for optimally doped crystal are of the form $\alpha\omega^3$ and are shown by dashed light green curves. α is a fitting parameter.

doped Bi-2212. However, there is an important difference: the absence of a clear-cut cubic low-frequency power law in the B_{1g} channel. In fact, the low-ω scattering is almost linear in frequency for the most over-doped PCCO crystal (x = 0.17) and the over-doped PCCO film (x = 0.17). The theory for Raman scattering in disordered or "dirty" d-wave superconductors predicts that the cubic low-frequency power law in the B_{1g} channel in the clean limit (quasiparticle scattering rate $\Gamma << 2\Delta$) will change to a linear power law in the presence of disorder ($\Gamma \sim 2\Delta$) [127]. The change from a cubic power law for optimally doped PCCO to a linear power law for the over-doped PCCO crystal and film (x≈0.17) implies the existence of a dirty d-wave gap in the over-doped samples. One must add here that the theory for dirty s-wave superconductors with finite quasiparticle lifetime broadening predicts smoothly decreasing sub-gap Raman intensities down to the lowest frequencies [128]. Therefore, we cannot rule out completely the possibility that the low frequency tails in the ERS spectra in over-doped samples are due to a dirty s-wave gap. We can, however, rule out the existence of a clean s-wave gap.

Fig. 6.7 compares the polarization and excitation wavelength dependence of the 2Δ peaks in the optimally doped and over-doped NCCO crystals. We observe that the gap changes from non-monotonic d-wave in the optimally doped sample (as discussed earlier) to a symmetry-independent one (for B_{2g} and B_{1g} symmetries) in the over-doped sample. For the over-doped NCCO sample, the low-ω scattering cannot be fitted to a cubic power law. These observations are in good agreement with the results on over-doped PCCO. As expected, the coherence peak positions are almost independent of the laser excitation energies. The data for the 799 nm laser wavelength is measured down to 4.5 cm^{-1}. There is no sharp scattering threshold down to these low frequency shifts. Therefore, we can rule out a clean s-wave gap in over-doped NCCO.

The ERS spectra in the A_{1g} channel for various Ce dopings in PCCO are shown in the third row of Fig. 6.5 .The 2Δ features in the A_{1g} channel occur at lower

energies compared to those in B_{2g} and B_{1g} channels. As mentioned earlier, the Raman scattering in the A_{1g} channel is influenced by Coulomb screening and details of the band structure, gap form and the Raman vertex and does not lend itself to a straightforward interpretation. Coulomb screening should lead to a much weaker intensity of pair breaking features in the A_{1g} channel. However, we find that the intensities of the 2Δ peaks in the A_{1g} channel are the same order of magnitude as those in crossed polarizations in all the over-doped samples and are significantly stronger in the under-doped and optimally-doped samples. This cannot be explained within the framework of existing theories and further theoretical work is needed to explain the doping dependence of the Raman spectra in the A_{1g} channel in PCCO.

The coherence peak energies in all measured Raman symmetries are plotted in Fig. 6.8a. The SC gaps measured by Raman spectroscopy in the B_{2g} and B_{1g} are in agreement with those measured with point contact tunneling spectroscopy for optimally doped and over-doped samples. For the under-doped film, the Raman data shows a smaller gap possibly due to stronger final state interactions. For under-doped samples, the two quasi-particles excited out of the SC condensate by Raman process continue to interact binding into a collective excitonic state that costs less energy than excitation of two independent quasiparticles. Similar observations were made previously for p-doped cuprates [129]. The coherence peaks in the A_{1g} channel occur at smaller energies than those in the B_{2g} and B_{1g} channels probably because of Coulomb screening.

The maximum gap value is observed in the B_{2g} channel for all dopings. The reduced gap value $2\Delta/k_BT_c$ (k_B is the Boltzmann constant) decreases monotonically in the B_{2g} channel with increasing doping, from 4.6 for the under-doped film to 3.5 for the over-doped samples (see Fig. 6.8b). This indicates weakening of pairing interactions with increasing doping. The reduced gap values in the B_{1g} channel lie between 4.2 and 3.5, with the the maximum value of 4.2 occurring near a doping of x $\approx$ 0.16. The gap or coherence effects or both vanish in the B_{1g} channel for the

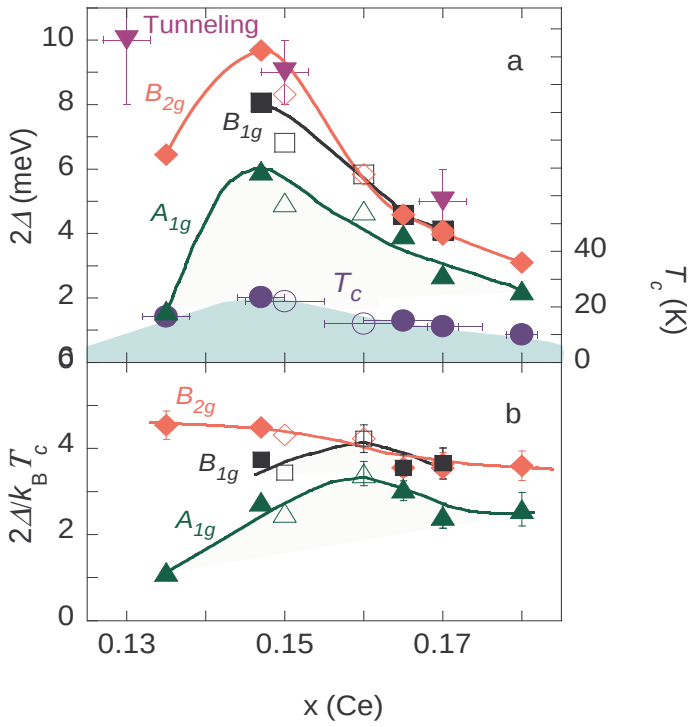

Figure 6.8: (a) The phase diagram of superconducting electron-doped cuprates explored by Raman spectroscopy. The peak positions of the 2Δ features for three symmetries are plotted. Filled symbols are for PCCO and the open symbols represent NCCO. T_c values are determined by magnetization measurements. Error bars on the cerium concentrations are shown only on the T_c data points to preserve clarity of the diagram. The size of the symbols for the Raman data represent the uncertainties in the quantities plotted on the vertical axis. Solid lines are guides to the eye. 2Δ obtained from point contact tunneling measurements is plotted for comparison and is denoted by inverted triangles.(b) Reduced gap $2\Delta/k_BT_c$ plotted for three Raman symmetries.

under-doped and most over-doped PCCO film. The reduced gap values in the A_{1g} channel also exhibit a maximum near x $\approx$ 0.16.

6.3 Doping dependence of the Drude response in the normal state and coherence effects in the SC state

The Drude (coherent) weight in the non-SC state and the coherence intensity in the SC state in the B_{2g} channel are discussed in this section.

The low energy electronic Raman scattering in the B_{2g} channel in the "normal" or non-SC state is dominated by a broad hump-like structure which we call the quasi-elastic scattering peak (QEP). This is seen clearly in the B_{2g} data just above T_c in Fig. 6.5. The QEP is due to the Drude response of the quasiparticles to the electromagnetic field [47, 130]. It can be shown that in the lowest order approximation, the Raman response function divided by the frequency shift i.e. $\chi"(\omega)/\omega$ (or Raman conductivity) is proportional to the real part of the optical conductivity $\sigma(\omega)$ [131] weighted by the Raman vertex. Since the real part of the optical conductivity can be described by a Drude model, so can $\chi"(\omega)$.

The Raman response in the normal state can be taken (at a phenomenological level) to consist of the Drude part that describes the coherent QEP, and the Marginal Fermi Liquid (MFL) part that describes the featureless, incoherent electronic continuum [115, 119].

$$\chi"_N(\omega) = \chi"_{Drude}(\omega) + \chi"_{MFL}(\omega) \tag{6.1}$$

This is related to Varma's description of the optical conductivity in the cuprates in terms of a Drude component at low frequencies plus a mid-IR contribution [115].

The Drude part of the Raman response function can be written as

$$\chi"_{Drude}(\omega) = a\frac{\Gamma\omega}{\omega^2+\Gamma^2} \tag{6.2}$$

and the MFL part as

$$\chi"_{MFL}(\omega) = b\tanh(\frac{\omega}{\omega_c}) \tag{6.3}$$

The flat and featureless electronic Raman continuum is a common feature in cuprates and extends up to several thousand wavenumbers. Its microscopic origin is still a matter of debate [119].

The two component fit to the normal state data of an over-doped PCCO crystal (x $\approx$ 0.165) obtained just above T_c is shown in Fig. 6.9. The fitting parameters a, b, Γ and ω_c have physical meaning. The integral (I_{Drude}) of $\chi"_{Drude}(\omega)/\omega$ (with respect to the frequency shift) from zero to infinity is equal to $a\pi/2$ and is proportional to the carrier density weighted by the Raman vertex. b is the value of the continuum at high frequency shifts. Γ is the quasiparticle scattering rate, assumed to be frequency independent. ω_c is the characteristic "cutoff" frequency of the continuum. The quantity I_{Drude} is plotted in Fig. 6.10a as a function of Ce doping.

The Raman response in the superconducting state at zero temperature $\chi"_{SC}(\omega)$ can also be described by a two component model.

$$\chi"_{SC}(\omega) = \chi"_{2\Delta}(\omega) + \chi"_{MFL}(\omega) \tag{6.4}$$

$\chi"_{2\Delta}(\omega)$ describes the SC coherence peak and $\chi"_{MFL}(\omega)$ is the incoherent continuum. It was shown in the previous chapter that the SC state Raman response in the non-symmetric channels (that are unaffected by Coulomb screening) at zero temperature is given by the momentum sum over the Tsuneto function weighted by the Raman coupling vertices ($\gamma_{\mathbf{k}}^{\alpha\beta}$) for corresponding polarization geometry ($\alpha\beta$).

$$\chi"_{2\Delta}(\omega) = \sum_{\mathbf{k}}(\gamma_{\mathbf{k}}^{\alpha\beta})^2\frac{\Delta_{\mathbf{k}}^2}{E_{\mathbf{k}}^2}\delta(2E_{\mathbf{k}}-\omega) \tag{6.5}$$

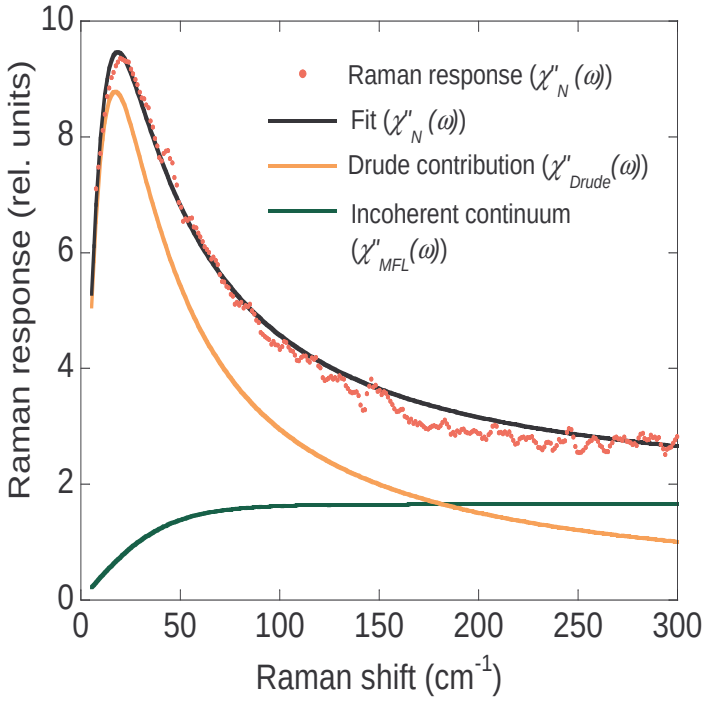

Figure 6.9: Red: The Raman response function for over-doped PCCO crystal (x $\approx$ 0.165) measured at 20 K in the non-superconducting state. The black line is a two component fit to the data. The orange line shows the coherent Drude contribution in the quasi-elastic scattering form and the green line represents incoherent continuum in the marginal Fermi liquid form.

We note that the integral ($I_{2\Delta}$) is given by

$$I_{2\Delta} = \int_0^\infty \frac{\chi"_{2\Delta}(\omega)}{\omega} d\omega = \sum_{\mathbf{k}} (\gamma_{\mathbf{k}}^{\alpha\beta})^2 \frac{\Delta_{\mathbf{k}}^2}{2E_{\mathbf{k}}^3}. \tag{6.6}$$

The integral ($I_{2\Delta}$) is proportional to the superfluid density

$$n_s \propto \sum_{\mathbf{k}} \frac{\Delta_{\mathbf{k}}^2}{2E_{\mathbf{k}}^3} \tag{6.7}$$

weighted by the Raman vertices. $I_{2\Delta}$ is plotted in Fig. 6.10b for several dopings of the electron-doped cuprates. The incoherent continuum is subtracted from the Raman response function in the SC state at the lowest temperature (≈ 4 K) to obtain only the coherent 2Δ contribution for integration. The contribution of the low-energy incoherent continuum in the superconducting state at energies comparable to 2Δ is not precisely known. We propose two estimates of the incoherent continuum at these low energies. The first estimate is based on the assumption that the continuum does not change in the superconducting state and is derived from the fit to data just above T_c (solid green line in Fig. 6.9). The second estimate is based on the assumption that the continuum vanishes below the energy 2Δ because the incoherent electronic scattering is completely suppressed by the opening of the superconducting gap. The difference between the measured low-temperature Raman response function and the continuum estimated by these two methods gives the lower and the upper bound for the coherent SC contribution. Thereafter, lower and upper bounds of $I_{2\Delta}$ are computed. Their average is plotted in Fig. 6.10b and one half their difference gives the error bars.

The superfluid density in the form ($1/\lambda^2$) is also plotted in Fig. 6.10b for several dopings of PCCO films for comparison. The data for the penetration depth (λ) is taken from Skinta *et al.* [24] and does not agree with data from Prozorov *et al.* [26]. It is not a subject of this thesis to discuss the disagreement between the penetration depth values from different groups. The Raman data gives relative values of the superfluid density and is in better qualitative agreement with the data of Skinta *et*

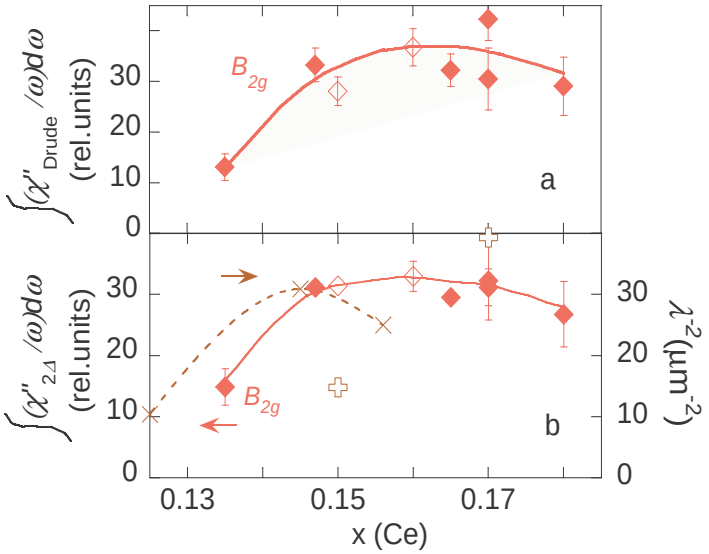

Figure 6.10: (a) Integrated Drude component and (b) integrated SC coherence intensity in the B_{2g} channel as a function of doping. The error bars for the Ce doping are the same as in Fig. 6.8. In (b) $1/\lambda^2$ data is also plotted for comparison: data from Ref. [24] is depicted by '$\times$' and linked by a dashed line while data from Ref. [26] is depicted by open crosses.

al. for under-doped and optimally doped PCCO. For over-doped PCCO, the data of Prozorov *et al.* appears to be in better agreement with the Raman data. The doping dependence of the $I_{2\Delta}$ (proportional to n_s) obtained from Raman data is in agreement with the doping dependence of the superfluid density for some of the hole-doped cuprates [132].

The significant results of the above analysis are that I_{Drude} and $I_{2\Delta}$ have the same doping dependence and same values (within error bars) for all dopings. This is in accordance with the optics 'partial' sum rule that states that the area under the real part of the optical conductivity have the same value in the normal and the superconducting states [133, 134]. By showing the equality of I_{Drude} and $I_{2\Delta}$, we have explicitly shown that the 'partial' sum rule is obeyed using the Raman data in the normal and SC states. This means that all the quasiparticles that contribute to the QEP in the normal state condense in the SC state to form the superfluid. The doping dependence of the normal state carrier density (I_{Drude}) and the superfluid density ($I_{2\Delta}$) increases with doping up to optimal doping and then remains almost constant with further increase in doping. This means that beyond optimal doping, the additional doped carriers do not contribute to the coherent Drude response nor to the superfluid but instead contribute to the incoherent continuum.

6.4 Magnetic field and temperature dependence of Raman spectra

In this section, we study the evolution of the spectra from the SC state into the normal resistive state as a function of temperature and of magnetic field applied normal to the *ab*-plane. The data was obtained with circularly polarized 647 nm light in the right-left (RL) scattering geometry. For the tetragonal D_{4h} symmetry, this geometry corresponds to $B_{1g}+B_{2g}$ representation. We have shown using linearly

polarized light that scattering in the B_{2g} channel exhibits the largest gap magnitude ($2\Delta_{max}$) and its intensity is about an order of magnitude greater than that in the B_{1g} channel . Therefore, the B_{2g} channel dominates the spectra in the RL scattering geometry.

Fig. 6.11 exhibits the SC coherence peak at the maximum gap value ($2\Delta_{max}$) for the optimally-doped (x $\approx$ 0.15) and over-doped (x $>$ 0.15) PCCO and NCCO crystals for two cases: (1) varying the magnetic field with constant temperature (5 K) and (2) varying temperature with zero magnetic field. By either increasing the temperature or magnetic field, the coherence peak loses intensity and moves to lower energies until it completely vanishes. We define an effective upper critical field, $H^*_{c2}(T, x)$, as the field that completely suppresses the coherence peak intensity: the Raman response remains field independent for $H > H^*_{c2}$. Above T_c or H^*_{c2} the coherence peak vanishes and the Raman response transforms into a broad overdamped low-frequency quasi-elastic scattering peak (QEP) $\chi"_{Drude}(\omega) = a\frac{\Gamma\omega}{\omega^2+\Gamma^2}$ that has been described in a Drude model as a coherent response of doped carriers [130, 47] above an incoherent featureless continuum response $\chi''_{MFL}(\omega) = b\tanh(\omega/\omega_c)$ [115]. This QEP is similar for both cases: $T > T_c$ and $H > H_{c2}$ at the lowest temperature, and therefore is independent of the means used to quench superconductivity. The a and b constants describe the coherent and incoherent contributions, ω_c is a cut-off frequency of order k_BT and the QEP position is governed by quasi-particle scattering rate (Γ) that characterizes the non-SC state. At low temperatures $\Gamma \approx 2$ meV for entire studied doping range. Notice that the characteristic energy scale for the SC gap ($2\Delta_{max}$) is several times the scattering rate for the optimally doped PCCO and NCCO samples. These two energy scales become quite similar for the over-doped samples.

Reduced gap values, $2\Delta_{max}/k_BT_c$, from Raman data on five single crystals of various doping levels are plotted in Fig. 6.12a as a function of the reduced temperature (T/T_c). For the lowest measured temperature, $2\Delta_{max}/k_BT_c$ values fall between

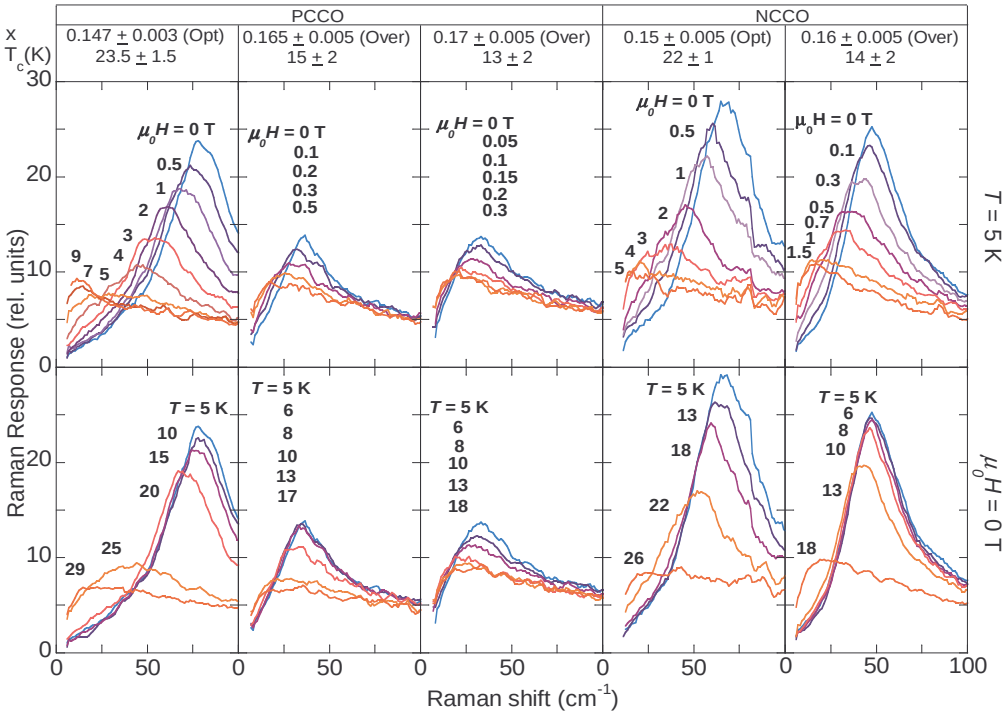

Figure 6.11: Representative Raman scattering spectra for three PCCO and two NCCO single crystals at optimal and over-doped carrier concentrations x. The first row shows the evolution of the spectra (in right-left polarization) with magnetic field applied normal to the ab-plane of the samples ($T \approx 5$ K). The second row shows the variation of the spectra with temperature between 5 K and Tc in zero magnetic field. The SC gap magnitude ($2\Delta_{max}$) is the energy at which the coherence peak intensity is highest.

4.5 for the optimally doped crystals and 3.5 for the most over-doped PCCO crystals. As the temperature is reduced below T_c for the optimally doped samples, the gap appears to open up faster than the mean-field prediction for a d-wave superconductor [135] suggesting strong phase fluctuations above T_c. The temperature dependence of the gap energy for the most over-doped samples is close to the prediction of BCS theory. However, a fit to the BCS theory does not necessarily mean that the gap in the over-doped samples has s-wave symmetry.

H_{c2} vs. T/T_c is plotted in Fig. 6.12b and shows a dramatic reduction of the upper critical fields in the entire temperature range and in the extent of the SC phase with increasing doping. The field that completely suppresses the coherence peak is determined to be the upper critical field, $H^*_{c2}(T)$. Also note that in contrast to $H^\rho_{c2}(T)$ obtained from magneto-resistivity [136, 137], $H^*_{c2}(T)$ displays negative curvature and a conventional temperature dependence.

We analyze Raman response in the mixed state assuming the presence of normal regions inside the vortex cores coexisting with SC regions surrounding the vortices. The Raman spectrum in a field is assumed to be a sum of contributions from the SC and normal regions. The normal state contribution to the measured Raman spectra is further assumed to be proportional to the number of vortices which itself is proportional to the applied field:

$$\chi''(\omega, H, T) = \chi''_{SC}(\omega, H, T) + \frac{H}{H^*_{c2}}\chi''_N(\omega, T). \tag{6.8}$$

Here $\chi''_N(\omega, T) = \chi''_{Drude}(\omega, T) + \chi''_{MFL}(\omega, T)$ is the normal state Raman response at or above critical field value $H^*_{c2}(T)$. $\chi''_{SC}(\omega, H, T)$ is the Raman response in SC state that we decompose in turn into low-frequency SC 2Δ coherence peak $\chi''_{2\Delta}(\omega, H, T)$ and a featureless continuum above the peak frequency.

In the Fig. 6.12c,d we plot for optimally- and over-doped crystals integrated coherence intensity $I(H) = \int(\chi''_{2\Delta}(\omega, H)/\omega)\, d\omega$ at the lowest measured temperature, 5 K, as a function of field. Here $\chi''_{2\Delta}(\omega, H)$ was obtained from Eq. 6.8. $I(H)$ is pro-

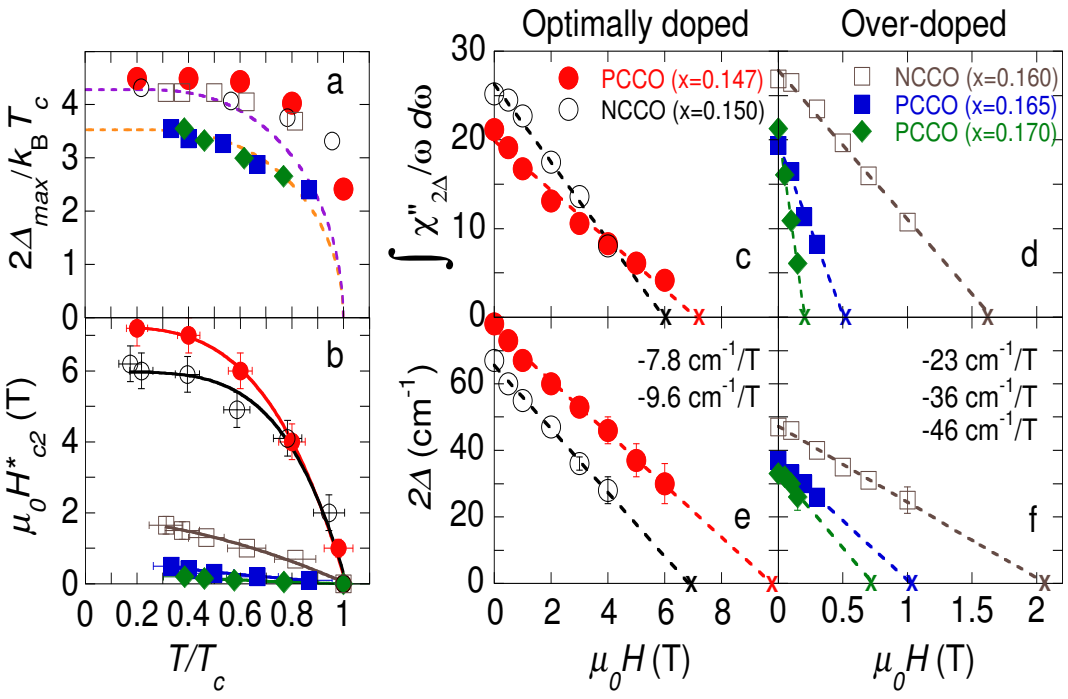

Figure 6.12: The temperature and field dependence of the SC order parameter amplitude and stiffness for two NCCO (open symbols) and three PCCO (filled symbols) single crystals with different Ce doping. The same symbols are used for all plots to indicate data on a particular crystal. The temperature dependence (a) of the reduced SC gap magnitude at zero field, and (b) of the effective upper critical field H^*_{c2} that completely suppresses the SC coherence peak intensity at the given temperature. Horizontal error bars for data in (a) are the same as shown in (b). In plot (a) the dotted lines are weak-coupling BCS predictions for temperature dependence of d-wave (violet) s-wave (yellow) SC gaps. The field dependence at 5 K of the integrated coherence intensity $\int(\chi''_{2\Delta}(\omega)/\omega)\,d\omega$ is shown in panels (c) and (d) and the SC coherence peak energy (2Δ) in panels (e) and (f) for optimally doped and over-doped crystals correspondingly. Approximated from the data, effective upper critical fields H^*_{c2} and the values of the SC gap collapse $H^{2\Delta}_{c2}$ are indicated with "x". Panels (e) and (f) include also the rate of the gap suppression $\frac{d\,2\Delta(H)}{d\,H}$.

portional to the superfluid density n_s weighted by the square of the Raman coupling vertex. In the panels Fig. 6.12e,f the coherence peak energy $2\Delta(H)$ is displayed as a function of field at 5 K. It appears that both the superfluid stiffness and the SC gap magnitude show monotonic almost linear decrease with the field. We use linear approximation to determine critical values of H^*_{c2} and $H^{2\Delta}_{c2}$ that completely suppress the superfluid density and the amplitude of the SC order parameter correspondingly. The data suggests that the SC gap remains finite at the effective critical fields H^*_{c2}. We find that the rate of the gap suppression, $d\,2\Delta(H)/d\,H$, is strongly doping dependent: -8 cmT^{-1} for optimally doped crystal rapidly increases with doping to surprisingly large, -46 cmT^{-1} for over-doped PCCO with $x = 0.17$.

The effect on superfluid stiffness, $d\,I(H)/d\,H$, is accordingly even steeper. This observation is in sharp contrast to hole-doped cuprates where the field induced suppression of the coherence peak intensity is not accompanied by any observable shift in the gap magnitude [111].

There appears to be a doping-dependent crossover in physical properties associated with superconductivity: relatively robust SC pairing at optimal doping becomes tenuous in the over-doped regime where field suppresses the pairing potential at an anomalously large rate while the T_c still remains relatively high. While the superfluid density vanishes at H^*_{c2}, the gap amplitude survives to higher fields and gets suppressed at $H^{2\Delta}_{c2}$.

The difference between H^*_{c2} and $H^{2\Delta}_{c2}$ increases for $x \leq 0.15$ samples probably due to strong phase fluctuations [140]. This is seen in Fig. 6.13, where the upper critical fields at $T = 5$ K, $H^*_{c2}(x)$ and $H^{2\Delta}_{c2}(x)$, and the related Ginzburg-Landau SC coherence length $\xi_{GL}(x) = \sqrt{\Phi_0/2\pi H^{2\Delta}_{c2}(x)}$ (Φ_0 is the fluxoid quantum) are plotted vs. Ce doping x.

The H^*_{c2} value of 7.2 ± 0.5 T for the optimally doped PCCO crystal is in agreement with the upper bound of $H_{c2} \approx 8$ T determined by thermal conductivity [63] and specific heat measurements [141]. This value also agrees with the upper

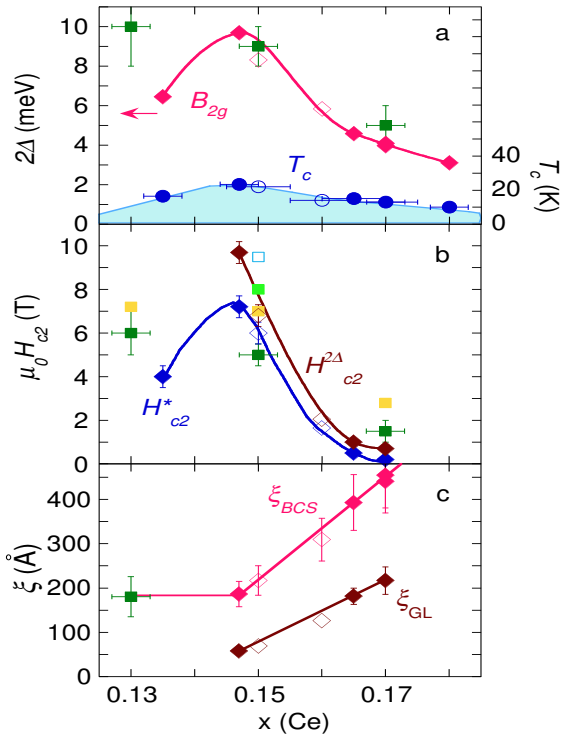

Figure 6.13: The phase diagram of PCCO (filled diamonds) and NCCO (open diamonds) superconductors explored by electronic Raman scattering in magnetic field. Panels show: (a) T_c (blue circles), the maximum energy of the SC 2Δ coherence peak and the distance between coherence peaks from point contact tunneling spectroscopy (dark green filled squares); (b) The doping dependence of the effective upper critical field $H^*_{c2}(x)$ (dark blue), the fields suppressing the gap amplitude $H^{2\Delta}_{c2}(x)$ (brown), and the comparison to upper critical fields obtained from other measurements (squares): point contact tunneling (dark green), Nernst effect on PCCO films [138] (yellow), Nernst effect on NCCO crystal [139] (light blue), and thermal conductivity [63] (light green); (c) the Ginzburg-Landau SC coherence length $\xi_{GL}(x)$ (brown) is compared to the BCS coherence length $\xi_{BCS}(x)$ (red) obtained from the Raman gap data. For under-doped sample, the gap value from point contact tunneling is used. The error bars on the Ce doping (x) are shown only on the T_c data points to preserve clarity of the figure. All solid lines are guides to the eye.

critical fields estimated by our tunneling spectroscopy data, tunneling spectroscopy with grain-boundary junctions [142, 88], and neutron scattering [31] measurements on optimally doped samples with similar T_c. Nernst effect measurements estimate $H_{c2} \approx 10$ T for optimally doped samples [139], consistent with $H_{c2}^{2\Delta} = 9.7 \pm 0.5$ T, the field at which the SC gap is expected to vanish from the Raman measurements. With increasing doping $H_{c2}^{2\Delta}$ drops by more than an order of magnitude reducing to 0.7 T for the $x = 0.17$ over-doped PCCO crystal. Correspondingly, $\xi_{GL}(x)$ rapidly increases with doping from ≈ 60 Å at optimal doping to 220 Å for $x = 0.17$ PCCO. For over-doped samples with similar Ce doping, specific heat [141] and point contact tunneling give somewhat higher H_{c2} values (≈ 3 T and 1.5 T respectively) compared to $H_{c2}^{2\Delta} = 0.7$ T from our Raman data.

In Fig. 6.13c we show that the values for $H_{c2}^{2\Delta}(x)$ are related to the SC gap. We compare here $\xi_{GL}(x)$ to BCS coherence length $\xi_{BCS}(x) = \hbar v_F / \pi \Delta_{max}(x)$, where the Fermi velocity $v_F = 4.3 \times 10^5$ m/s is estimated from ARPES measurements [143] and the lowest temperature SC gap values $\Delta_{max}(x)$ are used from Raman and tunneling data. The comparison plot reveals that $\xi_{BCS}(x)$ trend resembles doping dependence of $\xi_{GL}(x)$ and therefore confirms relation of $H_{c2}^{2\Delta}(x)$ to pairing potential $\Delta_{max}(x)$. It also indicates that the $\xi_{GL}(x)$ is still about two times lower and $H_{c2}^{2\Delta}(x)$ is about four times higher than expected for conventional BCS superconductor with an isotropic gap.

The ξ_{GL} for the electron-doped cuprates is significantly larger than for their hole-doped counterparts that leads to important differences. First, the size of the Cooper pair is larger than the average inter-particle spacing: $k_F \xi_{GL}$ parameter ranges between 40 and 150, still smaller than for conventional BCS superconductors but an order of magnitude larger than for hole-doped cuprates. For hole-doped cuprates, the upper critical fields are very high and the SC coherence length is short. The size of the Cooper pairs is comparable to the average inter-particle spacing: a rough estimate of parameter $k_F \xi_{SC}$ (k_F is the Fermi wave vector) leads to values in the range

of 3 to 20, two orders of magnitude smaller than for conventional BCS superconductors. In fact, the persistence of short-range anti-ferromagnetic (AF) correlations with doping, $\xi_{AF} \geq \xi_{SC}$, has been thought to be the cause for an effective pairing mechanism at least in the under-doped regime of the hole-doped cuprates.

Second, a larger Cooper pair size for electron-doped cuprates requires further pair interaction to be taken into account and leads to more complicated non-monotonic momentum dependence of the SC gap than the simplest $d_{x^2-y^2}$ form that well describes the gap function for hole-doped cuprates with very tight Cooper pairs.

6.5 Summary

We have investigated the electron-doped cuprates in the entire SC phase diagram with Raman spectroscopy. We find that the SC gap has a non-monotonic d-wave form in optimally doped PCCO, consistent with the earlier results on optimally doped NCCO. The symmetry of the gap in the under-doped film cannot be determined unambiguously because of the absence of the 2Δ peak in the B_{1g} channel. Nevertheless, the continuous, smooth decrease of the scattering intensity below 2Δ in the B_{2g} channel is consistent with a nodal order parameter (probably non-monotonic d-wave). The coherence peaks in the over-doped samples appear at the same energies in the two non-symmetric B_{1g} and B_{2g} channels. The continuous decrease of the low energy, sub-gap scattering and the absence of a clear threshold rules out a clean s-wave order parameter in the over-doped samples. There is a crossover of the low-frequency power law in the B_{1g} channel from cubic for optimally doped samples to linear for the most over-doped samples. This suggests that the order parameter may be dirty d-wave in the over-doped samples. However, a dirty s-wave gap cannot be dismissed completely. The $2\Delta/k_BT_c$ value of 3.5 for the over-doped samples is consistent with a weak-coupling (s-wave) BCS theory. The coherence lengths of a few hundred angstroms in the over-doped samples are approaching BCS values.

These are two indirect pieces of evidence that also suggest that the gap is becoming more "isotropic" with less directional dependence in **k**-space. Phase sensitive flux quantization experiments are necessary to elucidate the pairing symmetry in the over-doped samples.

We have shown that the "Raman conductivity sum rule" is satisfied in the normal and SC state ($I_{Drude} = I_{2\Delta}$). The coherent intensity of the Drude component in the normal state is the same as the coherent intensity of the 2Δ feature in the SC state for all dopings. This means that the coherent carriers in the normal state condense in the SC state. The integrated coherence intensity increases with the addition of carriers up to a doping of x $\approx$ 0.15. Beyond this doping, the additional carriers remain incoherent and do not contribute to the Drude conductivity or the superfluid density.

We have carried out a systematic study of doping, magnetic field and temperature dependence of the electron-doped cuprates in the SC state. We have plotted the field and temperature dependence of the magnitude and intensity of the 2Δ peaks for various dopings, and have also determined H_{c2} as a function of temperature and doping. We find a distinct change in these properties between the optimally-doped and over-doped samples, specially the reduction in H_{c2} by more than an order of magnitude.

Chapter 7

Conclusions

This chapter contains a summary of the important results we have obtained on the electron-doped HTSC with two spectroscopic techniques. We first discuss the salient results from point contact and high barrier tunneling spectroscopies followed by conclusions based on Electronic Raman Spectroscopy. We conclude with a coherent picture of the electron-doped cuprates that these two spectroscopies reveal and also comment upon future work that could lead to a better understanding of superconductivity in these unusual materials.

7.1 Point Contact and High Barrier Tunneling

We have performed Point Contact Spectroscopy (PCS) measurements into the *ab*-planes of under-doped (x = 0.13), optimally doped (x = 0.15) and over-doped (x = 0.17, 0.19) PCCO films. Our data on *low barrier strength (Z) junctions* indicates a transition in pairing symmetry near optimal doping. On under-doped PCCO, we observe a Zero Bias Conductance Peak (ZBCP) due to Andreev bound states and this is a signature of *d*-wave pairing symmetry. We do not observe a ZBCP in low Z PCS data on optimally-doped and over-doped PCCO and this points to absence of nodes in the gap. Our data, and fits to the data, indicate a fully gapped Fermi surface most consistent with $d + is$ pairing symmetry for optimally-doped and over-

doped PCCO. We find that our data for low barrier strength junctions for all doping levels can be best explained by a d- to $d + is$ pairing symmetry transition across optimum doping.

High barrier strength junctions on all dopings of PCCO show a gap-like feature with coherence peaks that are due to redistribution of quasiparticle states in the SC phase. The absence of a ZBCP in high Z junctions on under-doped PCCO is surprising and may be due to one or more of the following reasons. First, disorder at the junction interface may lead to suppression of the ZBCP. Secondly, an induced is order parameter at the surface may lead to gapped spectra. Thirdly, a gap with a non-monotonic d-wave form that has limited phase space around the nodes may make detection of Andreev Bound States more difficult. The direction of the narrow tunneling cone in high-Z junctions must be close to the nodal direction if Andreev bound states are to be detected. With the limitation imposed by surface roughness, the signature of Andreev bound states may be washed out by tunneling contributions from facets of various orientations, especially if the gap is non-monotonic d-wave. Moreover, the ZBCP observed in low-Z junctions in under-doped PCCO is probably due to the larger tunneling cone that makes it easier to detect Andreev bound states. The gap-like features in the spectra obtained on PCCO junctions with Ce doping greater than about 0.15 are due to a gap all around the Fermi surface.

High barrier Pb/PbO_x/RCCO (R = Pr, Nd) tunnel junctions on optimally doped single crystals reveal spectral features that are inconsistent with a clean s-wave gap and a clean monotonic d-wave gap. The data can be reconciled with a non-monotonic d-wave gap. The non-monotonic d-wave gap may lead to a low density of nodal quasiparticles that results in a small shoulder at the Pb gap edge in the $G-V$ spectra in the SC state of Pb and PCCO/NCCO. Because of the limited phase space around the nodal regions, the nodal quasiparticles play a less significant role compared to the fully gapped regions in **k**-space: the spectra show enhanced spectral weight at the sum of the Pb gap and a **k**-space average of the PCCO/NCCO gap.

When Pb is in the normal state, either due to $H > H_{c2}$ or due to $T > T_c$, the SC gap-like feature with coherence peaks of PCCO/NCCO is observed. No ZBCP due to Andreev bound states is observed in tunnel junctions, most probably due to the peculiar nature of the non-monotonic d-wave gap as discussed in the preceding paragraph.

For $H \geq H_{c2}$, we observe a gap-like feature in the normal state at the Fermi energy for all the doping levels that we have investigated in these experiments. The normal state gap is of the same order of magnitude as the superconducting gap. However, the NSG is much weaker and does not have coherence peaks like the SC gap. The depth of the gap depends on the barrier strength of the junction such that it is weaker in more transparent (low Z) junctions.

The NSG coexists with the SC gap at the lowest measured temperature (1.8 K). The NSG has a temperature dependence of its own and it vanishes at or below the superconducting T_c of the sample. The origin of the NSG remains to be discovered.

7.2 Electronic Raman Spectroscopy

We have performed a systematic Raman scattering study on various dopings of the electron-doped cuprates covering the SC phase. We observe 2Δ coherence peaks in the B_{2g} and A_{1g} channels for all dopings. The coherence peaks in the B_{1g} channel occur for all dopings except the under-doped and the most over-doped PCCO films. The coherence peaks in the A_{1g} channel occur at lower energies compared to those in the B_{2g} and B_{1g} channels for the same doping level. The coherence peak in optimally doped PCCO occurs at a higher energy in the B_{2g} channel than in the B_{1g} channel. The scattering decreases smoothly and continuously below the coherence peak and there is no sub-gap threshold. This is consistent with earlier data on optimally doped NCCO by Blumberg *et al.* [19] and is due to the non-monotonic d-wave order parameter in which the maximum gap occurs near the nodal direction

in **k**-space. We also observe a cubic low frequency power law in the B_{1g} channel and this provides confirmation of nodes along the (0,0)$\rightarrow(\pi,\pi)$ direction. For over-doped PCCO and NCCO samples, the coherence peaks occur at the same energies in both the B_{2g} and B_{1g} channels. There are low frequency tails in the spectra in both channels. The low frequency tails have linear frequency dependence in the B_{1g} channel in the over-doped samples (x $\approx$ 0.17). This is consistent with a dirty d-wave order parameter. However, a dirty s-wave gap cannot be ruled out. The maximum gap value occurs in the B_{2g} channel and is maximum for optimally doped samples. The reduced maximum gap value ($2\Delta/k_BT_c$) decreases slowly and monotonically in the B_{2g} channel with increasing doping. This implies the weakening of pairing interactions with increasing doping. The $2\Delta/k_BT_c$ values in B_{2g} channel lie between 4.6 and 3.5 and are consistent with weak-coupling d-wave theory.

The data just above T_c in the non-symmetric channels shows a broad peak called the quasi-elastic scattering peak (QEP). The QEP is much more pronounced in the B_{2g} channel. This QEP is due to the Drude response of the coherent charge carriers. The Raman spectra in the normal state can be resolved into the coherent Drude component and the incoherent continuum. The Drude component can be expressed in terms of the Raman conductivity ($\chi"/\omega$). The integrated area under the coherent Raman conductivity (I_{Drude}) is proportional to the carrier density. This increases with increasing doping up to optimal doping and then remains almost constant implying that additional carriers do not contribute to the coherent response. Nor do these additional carriers in the over-doped samples contribute to the superfluid density in the SC state. In fact the integrated area under the coherent Raman conductivity ($I_{2\Delta}$) in the SC state is proportional to superfluid density. We find that $I_{2\Delta}$= I_{Drude} and follows the same trend with doping. This shows that the Raman conductivity sum rule for coherent scattering is obeyed and that all the coherent quasiparticles condense below T_c into the Cooper pair condensate.

We have also studied the dependence of the coherence peaks on temperature and

magnetic field applied perpendicular to the *ab*-planes of the samples. We find that, for samples near optimum doping (x $\approx$ 0.15), the temperature dependence of the SC gap is consistent with the prediction of *d*-wave mean-field theory except near T_c. The temperature dependence of the gap in the over-doped samples appears to follow the weak-coupling BCS mean-field prediction. The upper critical fields that suppress long range phase coherence (H^*_{c2}) at the lowest achievable temperature ($\approx$ 5 K) are maximum for optimally doped samples ($\approx$ 7 T) and about 0.2 T for the most over-doped PCCO crystal (x $\approx$ 0.17). The upper critical field that suppresses the gap amplitude $H^{2\Delta}_{c2}$ also decreases by an order of magnitude with increasing doping. The steep drop in H^*_{c2} and $H^{2\Delta}_{c2}$ with increasing doping is partly due to the weakening of pairing interactions. However, this is probably not the only reason. It is possible that the increasing number of incoherent carriers in the over-doped regime assist the magnetic field in destroying SC phase coherence. The long coherence lengths of the electron-doped cuprates compared to the hole-doped cuprates suggest the importance of longer range SC interactions so that the influence of atoms beyond nearest neighbors becomes important. Thus, it is not surprising that higher harmonics shape the precise form of the SC gap at optimal doping and are likely to dominate at higher dopings.

7.3 A comparison of results from tunneling, Raman and other experiments

The data from Point Contact Tunneling is consistent with a transition in pairing symmetry from *d*-wave in the under-doped samples to a nodeless gap in the over-doped samples. This transition in pairing symmetry takes place just above optimal doping, such that PCCO films with x = 0.15 and T_c = 21 K are already in the regime where the Fermi surface is fully gapped. Barrier tunneling experiments in

PCCO and NCCO crystals with higher T_c values between 21 K and 23 K, and doping between x=0.14 and x=0.15, reveal spectra that can best be explained by a non-monotonic d-wave gap. Raman experiments on similarly doped crystals of PCCO and NCCO are consistent with a non-monotonic $d_{x^2-y^2}$ gap. For over-doped crystals and films, the Raman spectra in the SC state can be interpreted in terms of a dirty d-wave gap although a dirty s-wave gap scenario cannot be dismissed. One should add here that tunneling is a surface sensitive probe and the transition in pairing symmetry revealed by PCS may well be a surface effect. One must add that the most recent penetration depth studies on PCCO by two different groups disagree with each other, both in their conclusions about the nature of the pairing symmetry and in their values of the magnetic penetration depth [25, 26]. The most recent specific heat measurements in a magnetic field on over-doped samples are most consistent with an s-wave gap [50]. The phase sensitive flux quantization experiments are necessary on over-doped samples to clarify the symmetry of the gap.

We find that the gap magnitudes obtained from Raman spectra on optimal and over-doped samples are consistent with those obtained from tunneling measurements. The gap obtained from Raman on under-doped PCCO film is less than that obtained from tunneling because of final state interactions between the paired electrons in the Raman measurements.

The upper critical magnetic field values obtained from tunneling and Raman spectroscopies are roughly in agreement for optimally doped samples (see Fig. 6.13). H_{c2}^{*} obtained from Raman scattering for the under-doped film is near the lower bound of the upper critical fields estimated from PCS. This may well be due to the low superfluid density and strong phase fluctuations in the under-doped film. For over-doped samples, H_{c2}^{*} and $H_{c2}^{2\Delta}$ drop rapidly with increased doping in both Raman and PCS measurements. In the Raman measurements, $H_{c2}^{*} \approx 0.2$ T and $H_{c2}^{2\Delta} \approx 0.7$ T are lower compared to PCS ($H_{c2} \approx 1.5$ T). However, H_{c2} values for similar over-

doped samples estimated from spectroscopic methods are generally lower compared to those obtained from resistivity ($\approx$ 4 T) [136] and Nernst measurements ($\approx$ 3.5 T) [138] at similar temperatures. The order parameter in a magnetic field becomes a spatially dependent quantity. The spectroscopic methods, in particular Raman scattering, are sensitive to long range phase coherence. In contrast, resistivity and Nernst measurements do not directly probe SC phase coherence and can be influenced by fluctuation effects and vortex dynamics. Therefore, H_{c2} values obtained from spectroscopic techniques are the "true" upper critical magnetic fields.

7.4 Future work

Since the symmetry of the order parameter in over-doped samples is yet to be decisively resolved, high barrier tunneling into *ab*-planes of over-doped single crystals of the electron-doped HTSC may yield some answers. As reported in earlier chapters, excellent tunnel junctions with Pb have been obtained on optimally doped crystals and further effort is required to obtain the same quality junctions on over-doped crystals. Moreover, single crystals of another electron-doped cuprate $(Pr,La)_{2-x}Ce_xCuO_{4-\delta}$ have been prepared by the floating zone method [144]. Experiments with point contact and barrier tunnel junctions can be performed on these crystals. Tunneling experiments with break junctions in single crystals of the electron-doped cuprates can also be done and may shed some light on the symmetry of the gap.

One of the most interesting problems in electron-doped HTSC at the present time is to understand the origin of the normal state gap. We have shown from point contact tunneling that this gap exists at dopings between x = 0.13 and x = 0.19. There is on-going work on tunnel junctions with Pb on various dopings of c-axis oriented PCCO films such that tunneling is nominally along the c-axis [89]. Because of surface roughness of the films, contributions to the current arise both

from *ab*-plane and c-axis tunneling. The SC gap of PCCO is observed as well as the normal state gap. The NSG is more pronounced in this geometry probably because of contribution of the tunneling current along the c-axis. If the NSG has a magnetic origin, then a high magnetic field parallel to the *ab*-plane should influence the gap in some way. This experiment has to be performed at very high fields applied at an angle to the *ab*-planes, such that the normal component suppresses superconductivity and the parallel component may affect the gap. This experiment needs to be carried out at the High Magnetic Field Lab at Tallahassee, Florida.

It will also be interesting to perform tunneling on samples in the anti-ferromagnetic region of the phase diagram (x = 0 to x $\approx$ 0.12) in an effort to observe the evolution of the anti-ferromagnetic gap with doping. The NSG may well be related to the anti-ferromagnetic gap.

Raman data on PCCO crystals and films has been obtained in the normal state as a function of temperature and shows the evolution of the QEP. This data needs to be analyzed to obtain various normal state parameters including the quasiparticle scattering rate and relative carrier densities as a function of doping, temperature and scattering geometry.

One of the challenges is to understand the A_{1g} Raman response in the normal and SC states. We have extensive Raman data in the A_{1g} channel and we have to find ways of analyzing it.

We have also obtained preliminary "c-axis" Raman data in the (x,x), (x,z) and (z,z) scattering geometries on a slightly over-doped PCCO crystal. This data needs to be compiled and published.

BIBLIOGRAPHY

[1] M. Tinkham, *Introduction to Superconductivity*, 2nd ed. (McGraw-Hill, New York, 1996).

[2] J. R. Schrieffer, *Theory of Superconductivity* (W. A. Benjamin Inc., New York, 1964).

[3] J. G. Bednorz and K. A. Müller, Z. Phys. B **64**, 189 (1986).

[4] M. K. Wu, J. R. Ashburn, C. J. Torng, P. Hor, R. L. Meng, L. Gao, Z. J. Huang, Y. Q. Wang, and C. W. Chu, Phys. Rev. Lett. **58**, 908 (1987).

[5] P. Dai, B. C. Chakoumakos, G. F. Sun, K. W. Wong, Y. Xin, and D. F. Lu, Physica C **243**, 201 (1995).

[6] J. Bok, G. Deutscher, D. Pavuna, and S. A. Wolf, editors, *The gap symmetry and fluctuations in high T_c superconductors* (Plenum Press, New York, 1998).

[7] Z. X. Shen, W. E. Spicer, D. M. King, D. S. Dessau, and B. O. Wells, Science **267**, 343 (1995).

[8] Y. Tokura, H. Takagi, and S. Uchida, Nature **337**, 345 (1989).

[9] A. Damascelli, Z. Hussain, and Z.-X. Shen, Rev. Mod. Phys. **75**, 473 (2003).

[10] P. K. Mang, private communication.

[11] S. Mao, *Fabrication, characterization and properties of $Nd_{2-x}Ce_xCuO_{4-y}$ superconducting thin films and heterostructures.*, PhD thesis, University of Maryland at College Park, 1995.

[12] E. Maiser, P. Fournier, J. L. Peng, F. M. Araujo-Moriera, T. Venkatesan, R. L. Greene, and G. Czjzek, Physica C **297**, 15 (1998).

[13] J. Bok, G. Deutscher, D. Pavuna, and S. A. Wolf, editors, *The gap symmetry and fluctuations in high T_c superconductors* (Plenum Press, New York, 1998), chap. Current Research Issues for the Electron-doped Cuprates by P. Fournier, E. Maiser and R. L. Greene.

[14] N. P. Armitage, D. H. Lu, D. L. Feng, C. Kim, A. Damascelli, K. M. Shen, F. Ronning, Z.-X. Shen, Y. Onose, Y. Taguchi, and Y. Tokura, Phys. Rev. Lett. **86**, 1126 (2001).

[15] J. Bok, G. Deutscher, D. Pavuna, and S. A. Wolf, editors, *The gap symmetry and fluctuations in high T_c superconductors* (Plenum Press, New York, 1998), chap. The Spin Fluctuation Model for High Temperature Superconductivity: Progress and Prospects by David Pines.

[16] C. C. Tsuei and J. R. Kirtley, Rev. Mod. Phys. **72**, 969 (2000).

[17] C. C. Tsuei, J. R. Kirtley, G. Hammerl, J. Mannhart, H. Raffy, and Z. Z. Li, Cond-mat/0402655.

[18] C. C. Tsuei and J. R. Kirtley, Phys. Rev. Lett. **85**, 182 (2000).

[19] G. Blumberg, A. Koitzsch, A. Gozar, B. S. Dennis, C. A. Kendziora, P. Fournier, and R. L. Greene, Phys. Rev. Lett. **88**, 107002 (2002).

[20] B. Stadlober, G. Krug, R. Nemetschek, and R. Hackl, Phys. Rev. Lett. **74**, 4911 (1995).

[21] J. D. Kokales, P. Fournier, L. V. Mercaldo, V. V. Talanov, R. L. Greene, and S. M. Anlage, Phys. Rev. Lett. **85**, 3696 (2000).

[22] R. Prozorov, R. W. Giannetta, P. Fournier, and R. L. Greene, Phys. Rev. Lett. **85**, 3700 (2000).

[23] L. Alff, S. Meyer, S. Kleefisch, U. Schoop, A. Marx, H. Sato, M. Naito, and R. Gross, Phys. Rev. Lett. **83**, 2644 (1999).

[24] J. A. Skinta, M. Kim, T. R. Lemberger, T. Greibe, and M. Naito, Phys. Rev. Lett **88**, 207005 (2002).

[25] M.-S. Kim, J. A. Skinta, T. R. Lemberger, A. Tsukada, and M. Naito, Phys. Rev. Lett. **91**, 087001 (2003).

[26] A. Snezhko, R. Prozorov, D. D. Lawrie, R. Giannetta, J. R. J. Gauthier, and P. Fournier, Phys. Rev. Lett. **92**, 157005 (2004).

[27] L. Alff, S. Kleefisch, U. Schoop, M. Zittartz, T. Kemen, T. A. Marx, and R. Gross, Eur. Phys. J. B **5**, 423 (1998).

[28] S. Kashiwaya, T. Ito, K. Oka, S. Ueno, H. Takashima, M. Koyanagi, Y. Tanaka, and K. Kajimura, Phys. Rev. B **57**, 8680 (1998).

[29] B. Chesca, M. Seifried, T. Dahm, N. Schopohl, D. Koelle, R. Kleiner, and A. Tsukada, Cond-mat/0402131.

[30] Y. Dagan, M. M. Qazilbash, C. P. Hill, V. N. Kulkarni, and R. L. Greene, Phys. Rev. Lett. **92**, 167001 (2004).

[31] H. J. Kang, P. Dai, J. W. Lynn, M. Matsuura, J. R. Thompson, S.-C. Zhang, D. N. Argyriou, Y. Onose, and Y. Tokura, Nature **423**, 522 (2003).

[32] M. Fujita, M. Matsuda, S. Katano, and K. Yamada, Cond-mat/0311269.

[33] S. Sachdev, Science **288**, 475 (2000).

[34] W. A. Harrison, Phys. Rev. **123**, 85 (1961).

[35] L. Y. L. Shen, J. App. Phys. **40**, 5171 (1969).

[36] C. Wang, B. Giambattista, C. G. Slough, R. V. Coleman, and M. A. Subramanian, Phys. Rev. B **42**, 8890 (1990).

[37] I. Giaever, H. R. Hart, and K. Megerle, Phys. Rev. **126**, 941 (1962).

[38] G. E. Blonder, M. Tinkham, and T. M. Klapwijk, Phys. Rev. B **25**, 4515 (1982).

[39] M. Covington, M. Aprili, E. Paraoanu, L. H. Greene, F. Xu, J. Zhu, and C. A. Mirkin, Phys. Rev. Lett. **79**, 277 (1997).

[40] Y. Dagan and G. Deutscher, Phys. Rev. Lett. **87**, 177004 (2001).

[41] M. Cardona, editor, *Light Scattering in Solids I*, 2nd ed. (Springer-Verlag, Berlin, 1983).

[42] W. Hayes and R. Loudon, *Scattering of Light by Crystals* (John Wiley and Sons, New York, 1978).

[43] M. V. Klein and S. B. Dierker, Phys. Rev. B **29**, 4976 (1984).

[44] R. Sooryakumar and M. V. Klein, Phys. Rev. Lett. **45**, 660 (1980).

[45] S. B. Dierker, M. V. Klein, G. W. Webb, and Z. Fisk, Phys. Rev. Lett. **50**, 853 (1983).

[46] R. Hackl, R. Kaiser, and S. Schicktanz, J. Phys. C **16**, 1729 (1983).

[47] A. Koitzsch, G. Blumberg, A. Gozar, B. S. Dennis, P. Fournier, and R. L. Greene, Phys. Rev. B **67**, 184522 (2003).

[48] J. L. Peng, E. Maiser, T. Venkatesan, R. L. Greene, and G. Czjzek, Phys. Rev. B **55**, R6145 (1997).

[49] J. L. Peng, Z. Y. Li, and R. L. Greene, Physica C **177**, 79 (1991).

[50] H. Balci, *Specific Heat and Nernst Effect of Electron-doped High-Temperature Superconductors*, PhD thesis, University of Maryland at College Park, 2004.

[51] J. S. Kim and D. R. Gaskell, Physica C **209**, 381 (1993).

[52] J. Bok, G. Deutscher, D. Pavuna, and S. A. Wolf, editors, *The gap symmetry and fluctuations in high T_c superconductors* (Plenum Press, New York, 1998), chap. From Andreev Reflection to the Sharvin Contact Conductance by Guy Deutscher and Roger Maynard.

[53] S. Kashiwaya and Y. Tanaka, Rep. Prog. Phys. **63**, 1641 (2000).

[54] Q. Huang, J. F. Zasadzinski, N. Tralshawala, K. E. Gray, D. G. Hinks, J. L. Peng, and R. L. Greene, Nature **347**, 369 (1990).

[55] F. Hayashi, E. Ueda, M. Sato, K. Kurahashi, and K. Yamada, J. Phys. Soc. Jpn **67**, 3234 (1998).

[56] A. Mourachkine, Europhys. Lett. **50**, 663 (2000).

[57] A. Biswas, P. Fournier, M. M. Qazilbash, V. N. Smolyaninova, H. Balci, and R. L. Greene, Phys. Rev. Lett **88**, 207004 (2002).

[58] D. H. Wu, J. Mao, S. N. Mao, J. L. Peng, X. X. Xi, T. Venkatesan, R. L. Greene, and S. M. Anlage, Phys. Rev. Lett. **70**, 85 (1993).

[59] A. Andreone, A. Cassinese, A. D. Chiara, R. Vaglio, A. Gupta, and E. Sarnelli, Phys. Rev. B **6392**, 1994 (49).

[60] C. W. Schneider, Z. H. Barber, J. E. Evetts, S. N. Mao, X. X. Xi, and T. Venkatesan, Physica C **233**, 77 (1994).

[61] J. R. Cooper, Phys. Rev. B **54**, R3753 (1996).

[62] T. Sato, T. Kamiyama, T. Takahashi, K. Kurahashi, and K. Yamada, Science **291**, 1517 (2001).

[63] R. W. Hill, C. Proust, L. Taillefer, P. Fournier, and R. L. Greene, Nature **414**, 711 (2001).

[64] H. Balci, V. N. Smolyaninova, P. Fournier, A. Biswas, and R. L. Greene, Phys. Rev. B **66**, 174510 (2002).

[65] Y. Tanaka and S. Kashiwaya, Phys. Rev. B **74**, 3451 (1995).

[66] G. E. Blonder and M. Tinkham, Phys. Rev. B **27**, 112 (1983).

[67] C.-R. Hu, Phys. Rev. Lett. **72**, 1526 (1994).

[68] M. Fogelstrom, D. Rainer, and J. A. Sauls, Phys. Rev. Lett. **79**, 281 (1997).

[69] R. Krupke and G. Deutscher, Phys. Rev. Lett. **83**, 4634 (1999).

[70] S. Kashiwaya, Y. Tanaka, M. Koyanagi, and K. Kajimura, Phys. Rev. B **53**, 2667 (1996).

[71] R. J. Behm, N. Garcia, and H. Rohrer, editors, *Scanning Tunneling Microscopy and Related Methods* (Kluwer Academic Publishers, 1990), chap. Spectroscopy using Conduction Electrons by H. Van Kempen.

[72] I. K. Yanson, Sov. J. Low Temp. Phys. **17**, 143 (1991).

[73] R. C. Reinertson, C. W. Smith, and J. P. J. Dolan, Physica C **200**, 377 (1992).

[74] E. L. Wolf, *Principles of Electron Tunneling Spectroscopy* (Oxford University Press, New York, 1985).

[75] J. Y. T. Wei, N.-C. Yeh, D. F. Garrigus, and M. Strasik, Phys. Rev. Lett. **81**, 2542 (1998).

[76] A. Sharoni, O. Millo, A. Kohen, Y. Dagan, R. Beck, G. Deutscher, and G. Koren, Phys. Rev. B **65**, 134526 (2002).

[77] J. W. Ekin, Y. Xu, S. Mao, T. Venkatesan, D. W. Face, M. Eddy, and S. A. Wolf, Phys. Rev. B **56**, 13746 (1997).

[78] D. Rainer, H. Burkhardt, M. Fogelstrm, and J. A. Sauls, J. Phys. Chem. Solids **59**, 2040 (1998).

[79] Y. Tanaka, H. Itoh, Y. Tanuma, H. Tsuchiura, J. Inoue, and S. Kashiwaya, J. Phys. Soc. Jpn. **71**, 2005 (2002).

[80] Y. Tanuma, Y. Tanaka, and S. Kashiwaya, Phys. Rev. B **64**, 214519 (2001).

[81] M. Aprili, M. Covington, E. Paraoanu, B. Niedermeier, and L. H. Greene, Phys. Rev. B **57**, R8139 (1998).

[82] G. Deutscher, N. Achsaf, D. Goldschmidt, A. Revcolevschi, and A. Vietkine, Physica C **282-287**, 140 (1997).

[83] M. Vojta, Y. Zhang, and S. Sachdev, Phys. Rev. Lett. **85**, 4940 (2000).

[84] V. A. Khodel, V. M. Yakovenko, M. V. Zverev, and H. Kang, Phys. Rev. B **69**, 144501 (2004).

[85] Y. Ohashi, J. Phys. Soc. Jpn. **65**, 823 (1996).

[86] A. Kohen, G. Leibovitch, and G. Deutscher, Phys. Rev. Lett. **90**, 207005 (2003).

[87] A. Biswas, P. Fournier, V. N. Smolyaninova, R. C. Budhani, J. S. Higgins, and R. L. Greene, Phys. Rev. B **64**, 104519 (2001).

[88] L. Alff, Y. Krockenberger, B. Welter, M. Schonecke, R. Gross, D. Manske, and M. Naito, Nature **422**, 698 (2003).

[89] Y. Dagan, private communication.

[90] A. M. Duif, A. G. M. Jansen, and P. Wyder, J. Phys. Condens. Matter **1**, 3157 (1989).

[91] Y. V. Sharvin, Sov. Phys. JETP **21**, 655 (1965).

[92] G. Wexler, Proc. Phys. Soc. London **89**, 927 (1966).

[93] K. Gloos, Phys. Rev. Lett. **85**, 5257 (2000).

[94] C. Walti, H. R. Ott, Z. Fisk, and J. L. Smith, Phys. Rev. Lett. **85**, 5258 (2000).

[95] R. S. Gonnelli, A. Calzolari, D. Daghero, L. Natale, G. A. Ummarino, V. A. Stepanov, and M. Ferretti, Eur. Phys. J. B **22**, 411 (2001).

[96] A. I. D'yachenko, V. Y. Tarenkov, R. Szymczak, A. V. Abal'oshev, I. S. Abal'osheva, S. J. Lewandowski, and L. Leonyuk, Phys. Rev. B **61**, 1500 (2000).

[97] K. Hasselbach, J. R. Kirtley, and P. Lejay, Phys. Rev. B **46**, 5826 (1992).

[98] N. P. Armitage *et al.*, Phys. Rev. Lett. **87**, 147003 (2001).

[99] Y. Onose, Y. Taguchi, K. Ishizaka, and Y. Tokura, Phys. Rev. Lett. **87**, 217001 (2001).

[100] H. Yamamoto, M. Naito, and H. Sato, Phys. Rev. B **56**, 2852 (1997).

[101] I. Giaever, J. H. R. Hart, and K. Megerle, Phys. Rev. **126**, 941 (1962).

[102] S. Kashiwaya, Y. Tanaka, M. Koyanagi, S. Ueno, and K. Kajimura, Physica C **282-287**, 2405 (1997).

[103] Y. Dagan, R. Krupke, and G. Deutscher, Europhys. Lett. **51**, 116 (2000).

[104] P. N. Trofimenkoff, H. J. Kreuzer, H. J. Wattamaniuk, and J. G. Adler, Phys. Rev. Lett. **29**, 597 (1972).

[105] J. G. Adler, H. J. Kreuzer, and J. Straus, Phys. Rev. B **11**, 2812 (1975).

[106] A. A. Abrikosov and L. A. Fal'kovskii, Sov. Phys.-JETP **13**, 179 (1961).

[107] A. A. Abrikosov and V. M. Genkin, Sov. Phys.-JETP **38**, 417 (1974).

[108] M. Cardona, editor, *Light scattering in solids I, 2nd edition* (Springer-Verlag, Berlin, 1983), chap. Electronic Raman scattering by M. V. Klein.

[109] T. P. Devereaux and D. Einzel, Phys. Rev. B **51**, 16336 (1995).

[110] D. Einzel and R. Hackl, J. Raman Spec. **27**, 307 (1996).

[111] G. Blumberg, M. Kang, and M. V. Klein, Phys. Rev. Lett. **78**, 2461 (1997).

[112] L. V. Gasparov, P. Lemmens, N. N. Kolesnikov, and G. G*ü*ntherodt, Phys. Rev. B **58**, 11753 (1998).

[113] J. Bok, G. Deutscher, D. Pavuna, and S. A. Wolf, editors, *The gap symmetry and fluctuations in high-T_c superconductors* (Plenum Press, New York, 1998), chap. Light scattering from charge and spin excitations in cuprate systems by R. Hackl.

[114] J. Bok, G. Deutscher, D. Pavuna, and S. A. Wolf, editors, *The gap symmetry and fluctuations in high-T_c superconductors* (Plenum Press, New York, 1998),

chap. Analysis of the superconducting gap by electronic Raman scattering in $HgBa_2Ca_2Cu_3O_{8+\delta}$ single crystals by A. Sacuto and R. Combescot.

[115] C. M. Varma, P. B. Littlewood, S. Schmitt-Rink, E. Abrahams, and A. E. Ruckenstein, Phys. Rev. Lett. **63**, 1996 (1989).

[116] M. Tinkham, *Group Theory and Quantum Mechanics* (McGraw-Hill, New York, 1964).

[117] E. Y. Sherman, C. Ambrosch-Draxl, and O. V. Misochko, Phys. Rev. B **65**, 140510(R) (2002).

[118] A. Koitzsch, *Spectroscopic Investigation of Many-body Effects in Hole and Electron-doped Cuprates*, PhD thesis, Institute of Solid State and Materials Research Dresden, Dresden, Germany, 2004.

[119] S. L. Cooper and M. V. Klein, Comments Con. Mat. Phys. **15**, 99 (1990).

[120] T. P. Devereaux, D. Einzel, B. Stadlober, R. Hackl, D. H. Leach, and J. J. Neumeier, Phs. Rev. Lett. **72**, 396 (1994).

[121] X. K. Chen, J. C. Irwin, H. J. Trodahl, T. Kimura, and K. Kishio, Phys. Rev. Lett. **73**, 3290 (1994).

[122] M. Kang, G. Blumberg, M. V. Klein, and N. N. Kolesnikov, Phys. Rev. Lett. **77**, 4434 (1996).

[123] C. Kendziora, R. J. Kelley, and M. Onellion, Phys. Rev. Lett. **77**, 727 (1996).

[124] I. Bozovic and D. van der Marel, editors, *Spectroscopic Studies of Superconductors* (The International Society for Optical Engineering), chap. Electronic Raman Scattering in Copper-oxide Superconductors and related Compounds by R. Hackl, G. Krug, R. Nemetschek, M. Opel and B. Stadlober.

[125] T. Masui, M. Limonov, H. Uchiyama, S. Lee, and S. Tajima, Phys. Rev. B **68**, 060506(R) (2003).

[126] G. Blumberg, A. Koitzsch, A. Gozar, B. S. Dennis, C. A. Kendziora, P. Fournier, and R. L. Greene, Phys. Rev. Lett. **90**, 149702 (2003).

[127] T. P. Devereaux, Phys. Rev. Lett. **74**, 4313 (1995).

[128] T. P. Devereaux, Phys. Rev. B **47**, 5230 (1993).

[129] H. L. Liu, G. Blumberg, M. V. Klein, P. Guptasarma, and D. G. Hinks, Phys. Rev. Lett. **82**, 3524 (1999).

[130] G. Blumberg and M. V. Klein, J. Low Temp. Phys. **117**, 1001 (1999).

[131] B. S. Shastry and B. I. Shraiman, Phys. Rev. Lett. **65**, 1068 (1990).

[132] J. L. Tallon, J. W. Loram, J. R. Cooper, C. Panagopoulous, and C. Bernhard, Phys. Rev. B **68**, 180501(R) (2003).

[133] D. N. Basov, S. I. Woods, A. S. Katz, E. J. Singley, R. C. Dynes, M. Xu, D. G. Hinks, C. C. Homes, and M. Strongin, Science **283**, 49 (1999).

[134] M. V. Klein and G. Blumberg, Science **283**, 42 (1999).

[135] H. Won and K. Maki, Phys. Rev. B **49**, 1397 (1994).

[136] P. Fournier and R. L. Greene, Phys. Rev. B **68**, 094507 (2003).

[137] F. Gollnik and M. Naito, Phys. Rev. B **58**, 11734 (1998).

[138] H. Balci, C. P. Hill, M. M. Qazilbash, and R. L. Greene, Phys. Rev. B **68**, 054520 (2003).

[139] Y. Wang, S. Ono, Y. Onose, G. Gu, Y. Ando, Y. Tokura, S. Uchida, and N. P. Ong, Science **299**, 86 (2003).

[140] V. J. Emery and S. A. Kivelson, Nature **374**, 434 (1995).

[141] H. Balci and R. L. Greene, Cond-mat/0402263.

[142] S. Kleefisch, B. Welter, A. Marx, L. Alff, R. Gross, and M. Naito, Phys. Rev. B **63**, 100507(R) (2001).

[143] N. P. Armitage *et al.*, Phys. Rev. B **68**, 064517 (2003).

[144] B. Liang, private communication.